Dissecting the High Energy Plasma Environment of Sagittarius A*

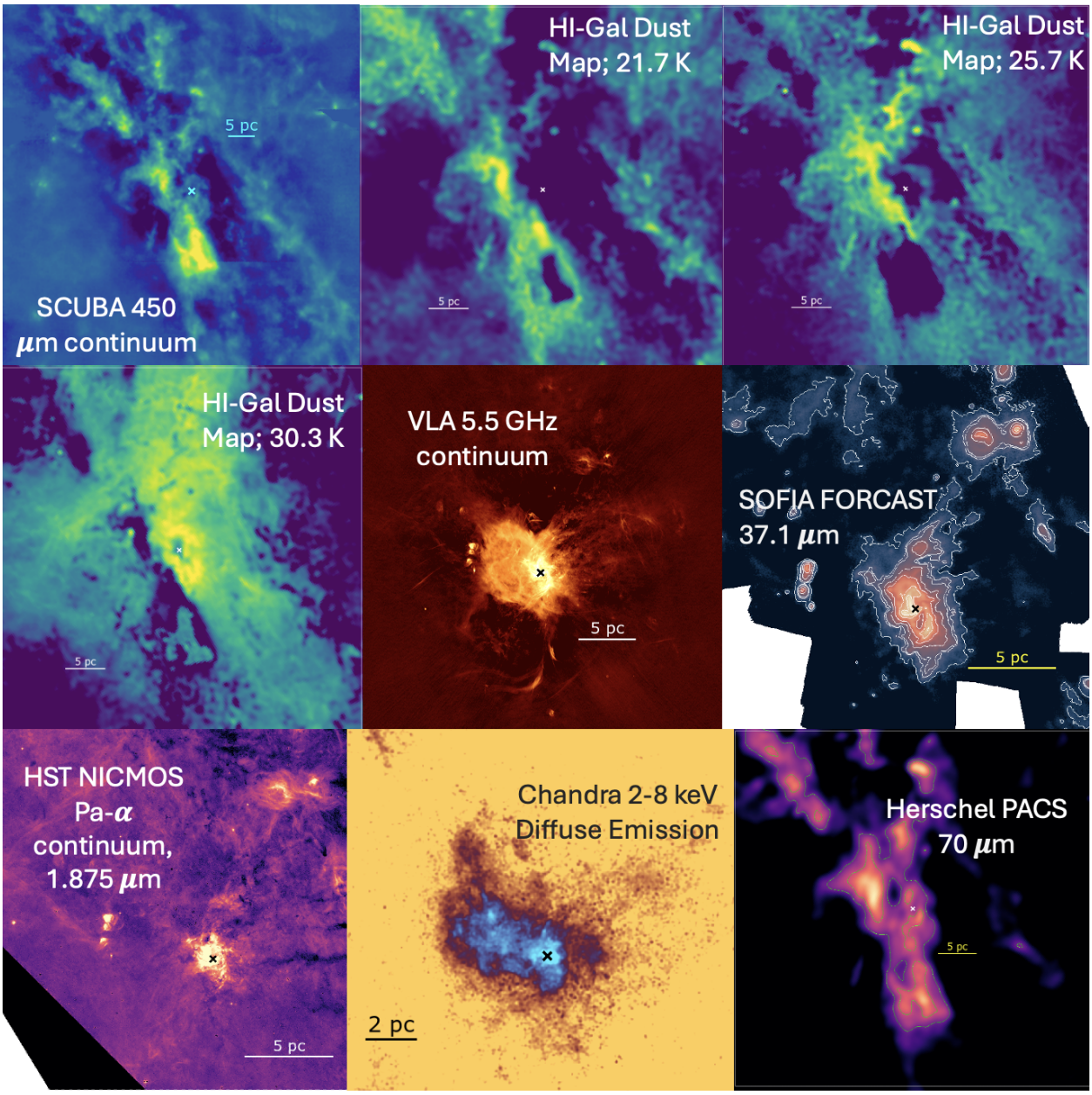
by

Mayura Balakrishnan

A dissertation submitted in partial fulfillment
of the requirements for the degree of
Doctor of Philosophy
(Astronomy and Astrophysics)
in the University of Michigan
2025

Doctoral Committee:

Professor Lia Corrales, Chair
Professor Nuria Calvet
Professor Kayhan Gültekin
Professor Dragan Huterer
Professor Sera Markoff, University of Amsterdam


5 pc
SCUBA 450
μm continuum
HI-Gal Dust
Map; 21.7 K
5 pc
HI-Gal Dust
Map; 25.7 K
5 pc
HI-Gal Dust
Map; 30.3 K
5 pc
VLA 5.5 GHz
continuum
5 pc
SOFIA FORCAST
37.1 μm
5 pc
HST NICMOS
Pa-α
continuum,
1.875 μm
5 pc
Chandra 2-8 keV
Diffuse Emission
2 pc
Herschel PACS
70 μm
5 pc

Mayura Balakrishnan
bmayura@umich.edu
ORCID iD: 0000-0001-9641-6550

© Mayura Balakrishnan 2025

DEDICATION

This dissertation is dedicated to my mother, Dr. Shyamala Nagaraj.

ACKNOWLEDGEMENTS

There are of course too many people to thank. From all stages of my life, from Malaysia to Ann Arbor to Emma Willard to my ten years at the University of Michigan, I was helped along the way by numerous mentors and peers. It all started with Uncle Sam, whose science/aerospace workshop allowed me to discover my love for space.

Thank you to Lia Corrales, for being a wonderful advisor and mentor. I will always be in awe of your organizational and coding skills. I'm so grateful that you helped me get onto the XRISM team. Thank you to my thesis committee, especially to Nuria for declaring me as an Astro major sophomore year, and Dragan for working on me with my honors thesis and hiring me to help with MMSS. Thank you to Eric Bell and Sean Johnson as well for being my Astro faculty friends.

Thank you to my mother, whose years of toil and trouble in academia and life paved the avenues in which I have been able to flourish, both personally and professionally. Thank you to my parents for feeding me this past month while I lost motivation I didn't know I still had. Thank you to my father (tennis kaki), my sister Kamini for *always* making an effort despite the giant age difference, my brother Ram, Daryl, Tiffany, and my lovely niblings, who have kept me humble all these years and given me a great reason to keep going. Thank you to my incredibly large, incredibly extended family in Malaysia that are too numerous to list. It has been wonderful having your support all these years, especially Anandhi and Vasantha Mami. Thank you to Uncle Vijayan, who has been there for me academically for a long, long time.

Thank you to Dana for being there for me for over a decade, and being the best friend anyone could ever ask for. Thank you so much to Nita, who's gotta be one of the best humans on Earth, for honoring me with her friendship since undergrad. Hope to watch more silly vampire shows with you soon. I don't have words to describe how important you two have been in my life.

Thank you so much to Paul, for being the best academic sibling one could ask for. You really helped me get through postdoc season. Thank you to my other X-ray elders for all their sage advice and help over the years, Mason, Renee, Erica, and Adi.

Thank you to the friends who have kept me sane over many, many years. Thanks to my Malaysian friends, Shria, Nritta, Aditi, Khave, Kahrthik, Amanda, and Hima. Thanks to

Alex Maynard, without whom my transition to the US would have been even worse. Thanks to all my Emma Willard friends, Ying, Kylie, Sonya, Soph, Dani, Sully, for years of crazy fun memories. Thank you to my college friends, Adrian, Melissa, Alex, Quinn. Thank you to Ethan for the cat pics and Elke for the holiday cookies. And thank you to all the other friends not mentioned, with whom I've shared numerous laughs and good times.

I owe heartfelt thanks to my UMich Astro crew, who were particularly important in getting me over the finish line. Thanks to my dyed hair crew, Thomas and Cayenne. Thank you Cayenne, for reading so much of my material. Thomas, he fell in love with a beautiful lady. Thank you to Vai and Nishant for watching bad Hindi movies with me. An enormous thank you as well to all the other UMich Astronomy grad students, specifically Annie, Marbely, Brandon, who have all helped keep me sane.

And lastly, thank you to Robert, who brought me an absolutely unprecedented and unexpected amount of joy during a very stressful year, and truly saw me for who I am. And without whom this document literally would have never compiled.

TABLE OF CONTENTS

DEDICATION ii

ACKNOWLEDGEMENTS iii

LIST OF FIGURES vii

LIST OF TABLES xiii

LIST OF ACRONYMS xiv

ABSTRACT xvi

CHAPTER

1 Introduction 1

1.1 Sagittarius A* (Sgr A*) 4
1.1.1 Basics of X-ray Spectroscopy 4
1.1.2 Chandra X-ray Observatory and Instrumentation 6
1.1.3 Accretion in the Low-Luminosity Regime 7
1.1.4 Past Studies of the *Chandra* Spectrum 8
1.2 The NSC Plasma Around Sgr A* 9
1.3 Sgr A East 12
1.3.1 Brief Overview of Supernova Remnants 13
1.3.2 Past studies of Sgr A East 13
1.3.3 Poissonian Generalized Morphological Component Analysis (pGMCA) 15
1.4 Summary 17

2 Modeling the High-Resolution Spectrum of Sgr A's accretion flow with a Radiatively Inefficient Accretion Flow 19

2.1 Abstract 19
2.2 Introduction 20
2.3 Dataset & Chandra Instrumentation 23
2.4 Methods 24
2.4.1 RIAF plasma model for the accretion flow 24
2.4.2 Modeling the High Energy Grating (HEG) Spectrum 29
2.4.3 Fitting 31
2.5 Results 32

2.5.1 HETG Spectral Fitting . . . 32
2.6 Summary & Conclusions . . . 34

3 Modeling the High-Resolution Spectrum of Sgr A's accretion flow with Hydrodynamical Simulations of Stellar Winds . . . 36

3.1 Abstract . . . 36
3.2 Introduction . . . 37
3.3 Methods . . . 40
3.3.1 Simulation Setup . . . 40
3.3.2 Modeling the HEG spectrum . . . 45
3.4 Results . . . 46
3.4.1 Searching For Signatures of a Cold Disk . . . 46
3.4.2 Stellar Winds vs. RIAF . . . 47
3.4.3 Sgr A* at micro-calorimeter resolution . . . 51
3.5 Summary & Conclusions . . . 53

4 Through a Fog of Plasma: Separating Supernova Remnant (SNR) Sgr A East from the Sgr A* Plasma Environment . . . 55

4.1 Abstract . . . 55
4.2 Introduction . . . 56
4.3 Datasets . . . 59
4.3.1 Multiwavelength Datasets . . . 59
4.3.2 Chandra Data . . . 60
4.4 Data Exploration . . . 62
4.4.1 Diffuse Emission . . . 62
4.4.2 Energy Hue Maps . . . 65
4.5 pGMCA Results . . . 67
4.5.1 Methods . . . 67
4.5.2 Outputs . . . 67
4.6 Interpretation . . . 70
4.6.1 The Sgr A East SNR . . . 72
4.6.2 Plasma associated with the NSC and/or Warm Dust . . . 74
4.6.3 Diffuse Galactic Center (GC) Plasma . . . 77
4.7 Summary . . . 79

5 Conclusions . . . 82

5.1 Examining the X-ray Spectrum of Sgr A* with a RIAF Model . . . 83
5.2 Examining the X-ray Spectrum of Sgr A* with SPH Simulations . . . 84
5.3 Examining the Emissions of Sgr A East using GMCA . . . 85
5.4 Future Directions: From the Central Parsecs to Galactic Scales . . . 86

APPENDIX A . . . 88

BIBLIOGRAPHY . . . 91

LIST OF FIGURES

FIGURE

1.1 TOP: Two schematics of the region of interest. On the left, Figure 1.1 from Baganoff et al. 2003. A schematic view of the galactic center on arcminute scales. On the right, Figure 2 from Murchikova et al. 2019, which is zoomed in on the circumnuclear ring and central star cluster. BOTTOM: Two X-ray images of the regions of interest. On the left, stacked *Chandra* X-ray observations of the region, with Sgr A*, supernova remnant Sgr A East, and the circumnuclear disk labelled. The extent of Sgr A East is not clear, and the presence of diffuse emission makes it hard to distinguish different components. On the right, Figure 1.1 from Wang et al. (2013) shows the plasma morphology closer to the outer edge of accretion flow of Sgr A* (Bondi radius denoting the Supermassive Black Hole (SMBH)s sphere of gravitational influence, cyan dashed circle). IRS 13 and Pulsar Wind Nebula (PWN) G359.95-0.04 lie very close to this. 2

1.2 Figure 2 from Calderón et al. (2020), where the dots are the Wolf-Rayet (WR) stars of interest, and the plasma clearly has a complex filamentary structure. In the center, because of extended timescales, a cool (T = 10^4 K) disk forms in the $T \sim 10^{6-7} K$ plasma. 11

1.3 Image of Sgr A complex in low, medium, and high energy bands. One can see the Sgr A East SNR in the radio and X-ray, while intermediate wavelengths generally capture components likely associated with the Nuclear Stellar Cluster (NSC) plasma and minispiral as opposed to the remnant. VLA image from (Zhao et al., 2016); SOFIA Forcast data from (Lau et al., 2015). 14

2.1 LEFT: Adaptation of Figure 1 from Corrales et al. (2020) showing the cleaned, quiescent 2 - 8 keV data for one roll angle. The 0th order (non-dispersed) image is displayed in HEG coordinates with the dispersion direction on the x-axis and the cross-dispersion direction on the y-axis. Solid black lines bracket the source extraction region out to 1.5″, while the dashed lines denote the background extraction region, 5″ away from Sgr A* in the cross-dispersion direction. The yellow and blue boxes refer to the effective regions of the image that contribute to the source and background spectra, respectively. RIGHT: Adapted from Figure 6 of Corrales et al. (2020), showing the the combined, unbinned, stacked and background subtracted HEG ±1 counts histogram in black. The best-fit Radiatively Inefficient Accretion Flow (RIAF) model from W13 is plotted in red, showing that the background subtracted spectrum has additional structure. The Fe XXV doublet wavelengths are plotted with blue dashed lines, and Fe XX, Fe XXII, Fe XXII, and Fe XXVI are plotted in brown, teal, blue, and orange lines respectively. 23

2.2 Diagram illustrating the geometry taken into account when calculating the RIAF model flux for the background region. We include the projected HEG extraction area; this reflects how the spectral extraction pipeline for HEG captures photon events between 1.5″ and 5″ in the cross-dispersion direction and up to 3″ along the dispersion axis. In other words, the source spectrum probes the central $3 \times 10^5 R_g$ while the background annulus spans $3 - 10 \times 10^5 R_g$. Only a portion of shells outside of $10^6 R_g$ lie within our line-of-sight projection in the background extraction region (green box). We use θ_{min} and θ_{max} to denote the angular boundaries between which a given shell is captured. These quantities are used to calculate the differential volume in each shell, as seen in Equations 2.3 and 2.4. 26

2.3 Demonstration of the procedure used to predict the HEG +1 source region counts histogram for a given RIAF model. The green curve shows the RIAF emission (in ph s^{-1}) calculated with `pyatomdb`, integrated over the differential volume corresponding to the physical region probed. We incorporate extinction (orange dashed) and a powerlaw for contaminating photons (blue dot-dashed). Convolving with the HEG ancillary response file (ARF) and response matrix file (RMF) leads to the final counts histogram (pink), washing out the fine structure from the original line profiles. 30

2.4 Final fits to the HEG +1 and -1 source and background regions, with error contours corresponding to RIAFs with parameters from chains within the top 5% likelihood range. The data and best-fit RIAF are plotted in black and blue, respectively, and are binned to have 4 cts/bin for visual clarity. The residual counts ($x_i - m_i$) are plotted in dashed blue lines (note the limits on the y-axis are different for the HEG +1 and HEG -1 residuals). The model captures some of the 6.7 keV emission but does not capture any structure in the background. 33

2.5 LEFT: Corner plot from the final fits of our RIAF model with `pyatomdb`, showing the distributions for RIAF s (material density slope), q (temperature profile slope), and Z_{Fe} (relative to solar; all other elemental abundances were set to 2 $Z_\odot$). Overall, the data prefer sub-solar Iron abundances, s values close to 1, and $q \approx 0.22$. 34

3.1 The high-resolution quiescent spectrum of Sgr A*, extracted in Corrales et al. (2020), plotted in counts. The top and bottom panels show the data from the HEG +1 and -1 orders, respectively. In this work, we focus on the Fe Kα complex, between 6.4 and 7.2 keV. The spectra extracted from the source (out to 1.5 $''$) and background (between 1.5$''$and 5$''$) regions are plotted in black and blue, respectively, and are rebinned to a factor of 3. 41
3.2 The top and bottom rows show the results of the disk (runtime of 3500 yr) and no-disk (runtime of 1100 yr) scenarios, respectively, for gas emitting at 6.7 keV. The plots span the central $12'' \times 12''$ surrounding Sgr A*, with North upwards and East to the left. LEFT: Column density map of the region, with the cool disk of gas seen clearly in the top left panel. MIDDLE: 6.7 keV X-ray intensity with the dark blue highlighting high levels of Fe Kα emission. RIGHT: Illustration of the velocity structure in this complex plasma, with color denoting the line-of-sight velocity corresponding to the line profile's maximum X-ray brightness for each pixel. The grayscale overlay reflects X-ray emission intensity, i.e. dimmer regions indicate X-ray dim gas. 44
3.3 LEFT: Line profiles generated by plasma simulated in the 0$''$- 1.5$''$source region (top) and 1.5$''$- 5$''$background region (bottom). MIDDLE & RIGHT: Predicted counts histograms calculated for HEG +1 (middle) and HEG -1 (right) for the disk (solid curves) and no-disk (dashed curves) plasma scenarios in the stellar winds simulation. We plot the source and background regions in purples and reds, respectively. The small differences between the final spectra with and without a cold gas disk are slight and not resolvable with *Chandra*-HETG, differing only by $\sim 2.6\%$ at the peaks. We are thereby unable to detect evidence of the $\sim 10^4$ K disk from X-ray spectroscopy alone. 47
3.4 Final fits to the HEG +1 and -1 source and background regions. The observation is plotted in black, with the best-fit RIAF model in blue and the stellar wind simulations plotted in pink. The residual counts spectrum (observation $-$ model) are plotted below each subplot. The data is binned to a factor of 4 for visual clarity, however, the fitting was performed on the unbinnned HEG data. While the models capture the 6.7 keV peak in the source spectrum, most of the observed line structure is not predicted in the simulations. 50
3.5 Histograms showing the Cash statistic from the posterior distributions of both the RIAF (blue) and stellar wind simulation fits (pink). 51
3.6 The anticipated *NewAthena* photon counts spectra for the stellar wind plasma models (red) under both disk (solid) and quasi-steady (dot-dashed) accretion scenarios in the Fe Kα region. The best-fit RIAF and contours from Chapter 2 are overlaid in blue. The stellar wind model will be differentiable from the RIAF model, and it is possible, with a high signal-to-noise, to detect signatures of the cold disk in the X-ray plasma. 52

4.1 View of the region of interest in several different wavelength bands. In all panels, North is up and East is to the left, and an "X" denotes the location of Sgr A*. *a)* SCUBA 450μm continuum image, showing the distribution and density of the molecular gas; *b) - d)* Herschel HI-Gal dust temperature maps, reflecting the column density of material at a given dust temperature (labelled) along that line of sight (Marsh et al., 2017) ; *e)* VLA 5.5 GHz continuum image of the region, showing the extent of the supernova remnant shell (Zhao et al., 2016); *f)* SOFIA FORCAST 37.1μm emission, characterizing the warm dust in the region (Lau et al., 2015); *g)* HST NICMOS 1.875 μm Pa-α continuum (Wang et al., 2010); *g)* Chandra 2-8 keV diffuse emission, with point sources removed, showing the major plasma components: the Sgr A* plasma environment and the supernova remnant (this work). 61
4.2 The results of stacking 1.3 Ms *Chandra* ACIS-I observations, listed in Table 4.1. Each image has a 30" bar in the bottom left. We have separated the data into the four energy bands of main interest: 2−8 keV (full band; top left), 1−2.6 keV (Si and S; top right), 2.6−5 keV (Ar; bottom left), and 5−8 keV (Fe; bottom right). Note that the smoothing scales differ between images. 64
4.3 Both panels show energy hue maps spanning 2−8 keV, but differ in labeling. The color of each pixel is dictated by its median energy, while the lightness and saturation are determined by the X-ray intensity in that pixel. The median energy colorbar is shown on the right. LEFT: We identify spectrally differentiated features of interest. RIGHT: Overlaid are radio contours of the supernova remnant shell from (Zhao et al., 2016). Note that unlike the diffuse emission images, these are not exposure corrected; see text for details. 66
4.4 Energy hue maps generated only with photons between 5−8 keV. Here, the distinction between the SNR Iron core and the plasma surrounding Sgr A* is highlighted. The plasma associated with Sgr A* seems to correspond to median energies ∼6-6.2 keV while the SNR Iron core has median pixel energies closer to 6.7 keV. 66
4.5 GMCA outputs and corresponding spectra. The output images have been divided by exposure maps created with `flux_obs`. All images are on the same log-spaced colorbar, with a scale bar denoting 2 pc and an "X" at the position of Sgr A*. The top row shows the two main components seen between 5−8 keV, while the bottom two rows display the four components identified by the algorithm in the 2−5 keV energy range. Each component is labeled with notation we refer to throughout this work. 68
4.6 GMCA outputs we believe capture emission from the supernova remnant. Each image has the radio shell (Zhao et al., 2016) overlaid in white, an X at the location of Sgr A*, and a scale bar showing the extent of 2 parsecs in the bottom left. Below each image, we plot the associated spectrum. The panel on the left is from the 5−8 keV component, while the other two are emission components from the 2−5 keV data. The line centroids and widths can be found in Table 4.2. 70

4.7 Median energy map of 2−8 keV photons (identical to Figure 4.3). The brightness and saturation in each pixel correspond to the X-ray intensity, while the color corresponds to the median energy (colorbar in units of eV). Overlaid in white and yellow are the left and middle panels, respectively, from Figure 4.6. The 2−5 keV ejecta component is co-sptial with the two X-ray bright and red features seen in Figure 4.3. The Iron line component appears to be ceneterd on high median energy pixels, the iron core denoted in Figure 4.3. 73
4.8 TOP: Schematic from Murchikova et al. 2019 showing the extents of various structures within and associated with the Circumnuclear Disk (CND). The schematic has rotation markers, showing that the molecular filament is expected to be redshifted along the line of sight due to Galactic rotation. BOTTOM LEFT: N_{H_2} column densities of gas associated with dust at 25.7 K (derived from HI-Gal plane survey dust maps Marsh et al., 2017), with VLA 5.5 GHz contours and 2−5 pGMCA Component 3 contours in white and cyan, respectively. RIGHT: pGMCA 2−5 keV component 3, from Figure 4.6, with 44 GHz methanol masers (McEwen et al., 2016) plotted (maser legend is to the left) and contours from the 25.7 K emission. The pink arrows in the bottom right image highlight regions where it appears the X-ray plasma is pushing up against material associated with 25.7 K dust. 75
4.9 LEFT: SCUBA 450 μm emission (colormap) with overlaid contours. RIGHT: 2–8 keV energy hue map, with the same contours from the left panel shown in cyan. Arrows mark gaps in the molecular material, and the red regions in the energy map correspond precisely to these holes. This alignment indicates that the SNR lies behind the molecular gas where the median pixel energy is higher, since the softer X-ray emission has been absorbed by the foreground material. 76
4.10 GMCA outputs that appear co-spatial with warm and hot gas emission. Each image has cnotours from 37.1μm $\sim$ SOFIA FORCAST dust emission ($T_{dust} \sim 100K$) and 1.875 μm Pa-α HST NICMOS $\sim$ ($T_{gas} \sim 100K$) emission in pink and white, respectively. They also have an X at the location of Sgr A* and a scale bar showing the extent of 2 parsecs in the bottom left. The panel on the left is emission between 2−5 keV while the panel on the right is emission between 5−8 keV. The pink and white arrows denote regions where the contours align particularly well with the pGMCA extracted component. The corresponding spectra are plotted below each image, with continuum and line fits that were used in the calculation of line centroids listed in Table 4.2. The component on the left traces hot plasma pockets that coincide with both the NSC and dust within the Sgr A East shell (Lau et al., 2015). This implies that the dust (denoted by the right arrow) has endured the passage of the reflected shock and has been shock heated. 78
4.11 GMCA 2−5 keV Component 2. On the left, the image is overlaid with contours from the SCUBA 450 μm continuum (Pierce-Price et al., 2000). The colorbar is consistent with the other pGMCA outputs, an "X" marks the location of Sgr A*, and a 2 pc scale bar is shown on the bottom right. On the right, the spectrum is dominated by a strong feature at 2.4 keV. This component displays the broadest lines of all pGMCA outputs, indicative of a diffuse and turbulent plasma. . . . 79

A.1 Merged *Chandra* event image created using `reproject_obs`, with point sources identified by `wavdetect` shown as green ellipses. These regions were manually refined to exclude diffuse structures misidentified as compact sources. The black diamond near the center marks the location of the supermassive black hole, Sgr A*. The image is centered on Sgr A* and spans 8.4' x 8.4'. 90

LIST OF TABLES

TABLE

2.1 Summary of priors and fit results from our MCMC sampling. The Iron abundance, Z_{Fe} is given in units of $Z_{\odot}$. Z_{Fe} and the normalization on the powerlaw, N_{PL}, are given gaussian priors in additional to hard limits. For each parameter, we list the best-fit value and the 90% credible intervals. 32

4.1 List of the *Chandra* observations used in this chapter and their respective exposure times and start dates. 63

4.2 Line features identified in the 2–5 keV band across pGMCA components. Candidate lines are matched by centroid energy and temperature peak to known transitions. Errors on the values are 3σ uncertainties. Below, we list the possible ions corresponding to the spectral features in the pGMCA outputs, with the recombination (R), intercombination (I), and forbidden (F) line centroids, along with peak plasma temperatures associated with the resonance lines. 71

LIST OF ACRONYMS

AGN Active Galactic Nuclei

ADAF Advection-Dominated Accretion Flow

ACIS Advanced CCD Imaging Spectrometer

AMR Adaptive Mesh Refinement

CGM Circumgalactic Medium

CCD Charge-Coupled Device

CND Circumnuclear Disk

CIE Collisional Ionization Equilibrium

CNR Circumnuclear Ring

CMZ Central Molecular Zone

CV Cataclysmic Variable

LETG Low Energy Transmission Grating

HETG High Energy Transmission Grating

HETG-S High Energy Transmission Gratings Spectrometer

HRC High Resolution Camera

MEG Medium Energy Grating

HEG High Energy Grating

GC Galactic Center

GMCA Generalized Morphological Component Analysis

GRMHD General Relativistic Magnetohydrodynamic

GCXVP Chandra X-ray Visionary Project

ISM Interstellar Medium

IR Infrared

LLAGN low-luminosity AGN

MW Milky Way

MCMC Markov Chain Monte Carlo

MHD Magnetohydrodynamic

MMSNR Mixed-morphology Supernova Remnant

NEI Non-Equilibrium Ionization

NSC Nuclear Stellar Cluster

PWN Pulsar Wind Nebula

RIAF Radiatively Inefficient Accretion Flow

SPH Smoothed Particle Hydrodynamics

SED Spectral Energy Distribution

Sgr A* Sagittarius A*

SMBH Supermassive Black Hole

SNR Supernova Remnant

WR Wolf-Rayet

XRSM X-ray Imaging & Spectroscopy Mission

XVP X-ray Visionary Program

ABSTRACT

The crowded central parsecs of our Galaxy offer a unique environment to study accretion physics, plasma dynamics, star formation, and more. Within arcseconds of central supermassive black hole (SMBH) Sagittarius A* (Sgr A*), colliding stellar winds from Wolf-Rayet (WR) stars in the nuclear star cluster generate a hot plasma reservoir from which Sgr A* accretes. Given this abundance of plasma, the SMBH radiates at a lower luminosity than expected. Through *Chandra* X-ray spectroscopy and imaging, I examine the extended plasma environment at multiple scales. To investigate the spectrum of the accretion flow, I perform forward-modeling of High Energy Transmission Grating-Spectrometer (HETG-S) data, accounting for the accretion geometry and instrumental effects. I find that a Radiatively Inefficient Accretion Flow (RIAF) model fit to the quiescent HETG-S spectrum indicates an outflow balancing inflowing material and a sub-solar iron abundance. Next, I generate synthetic spectra from smoothed particle hydrodynamic simulations of the stellar-wind plasma and find that these fit the HETG-S spectrum as well. Distinguishing the RIAF and the stellar wind plasma scenarios may be possible with future microcalorimeters that have high spatial resolution. At larger angular scales, the extended Sgr A* plasma environment overlaps in our line of sight with the supernova remnant (SNR) Sgr A East. An improved understanding of Sgr A East provides crucial insights into recent star formation, dust physics, and feedback processes occurring within the GC. I apply data-driven signal separation methods to analyze *Chandra* imaging observations encompassing the extended region around Sgr A*. Through this analysis, I successfully isolate the emission signature of this unique SNR from the surrounding cooler plasma associated with Sgr A*. By integrating a comprehensive set of multiwavelength datasets, I characterize both the spatial distribution and spectral properties of distinct X-ray components, enabling the identification of relationships among these structures and facilitating a robust discussion of their broader physical implications.

CHAPTER 1

Introduction

Astronomical observations consistently reveal that supermassive black holes (SMBHs), ranging from millions to billions of solar masses, anchor the dynamical centers of most galaxies. Empirical scaling relations have established strong correlations between fundamental properties of SMBHs and key characteristics of their host galaxies, suggesting intrinsic co-evolution between SMBHs and their galactic environments (Kormendy & Ho, 2013). Notably, SMBH mass correlates strongly with global host galaxy properties, including bulge mass, luminosity, and stellar dynamics—particularly the stellar velocity dispersion, measured far beyond the galactic nucleus (McConnell & Ma, 2013). The Galactic Center (GC) of our own Milky Way provides an unparalleled opportunity to probe this fundamental connection, offering sub-parsec resolution that allows detailed study of astrophysical processes governing the SMBH-galaxy interplay.

Lying at the center of our Milky Way, 8.1 kiloparsecs (26,400 light-years) from Earth, our central SMBH Sagittarius A* (Sgr A*) is embedded within a dense nuclear star cluster (NSC) and surrounded by a turbulent ecosystem of hot plasma, dust, strong magnetic fields, and multiphase gas structures. Figure 1.1 introduces the primary components within the central arcminutes of our Galaxy. In the top row, schematics from Baganoff et al. (2003) and Murchikova et al. (2019) illustrate the arrangement of the stellar and gaseous components, highlighting the circumnuclear disk (CND) and ionized minispiral Sgr A West. The CND, comprised of dense, cold molecular gas, orbits the SMBH at radii of 1.5–3 pc (Genzel et al., 2010), and the minispiral channels material inward, funneling gas toward Sgr A*, where it is ionized by shocks and intense ultraviolet radiation (Tsuboi et al., 2017). Within the innermost parsec, outflows from young massive stars in the NSC collide and thermalize, generating hot, diffuse, X-ray-emitting plasma clearly visible in the *Chandra* images (Figure 1.1, bottom panels). Zooming in, there is also X-ray emission close to the SMBH from the pulsar wind nebula (PWN) G359.95-0.04 and the massive star cluster IRS 13, both situated within 5″ of Sgr A* (Wang et al., 2013).

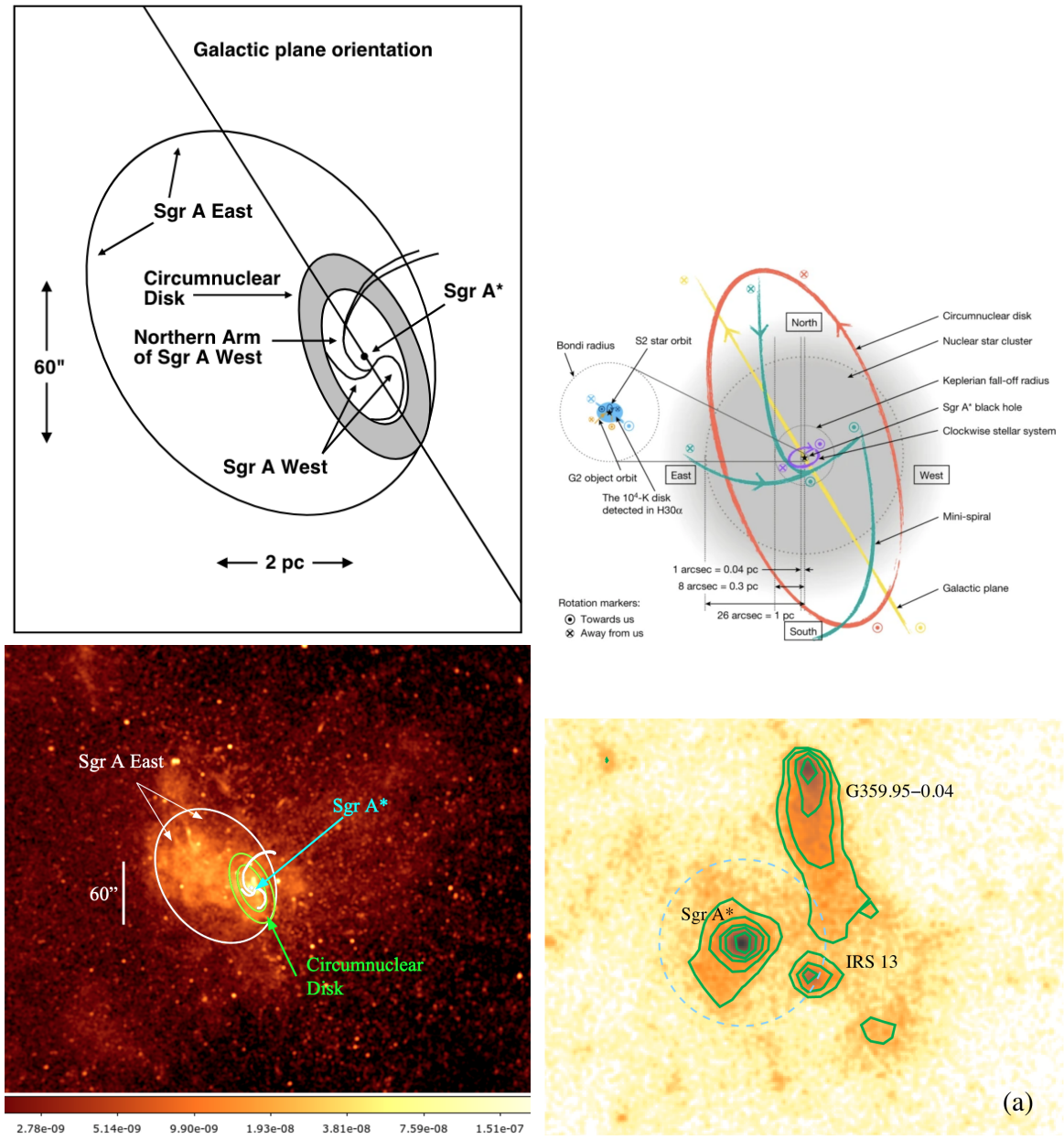


Figure 1.1: TOP: Two schematics of the region of interest. On the left, Figure 1.1 from Baganoff et al. 2003. A schematic view of the galactic center on arcminute scales. On the right, Figure 2 from Murchikova et al. 2019, which is zoomed in on the circumnuclear ring and central star cluster. BOTTOM: Two X-ray images of the regions of interest. On the left, stacked *Chandra* X-ray observations of the region, with Sgr A*, supernova remnant Sgr A East, and the circumnuclear disk labelled. The extent of Sgr A East is not clear, and the presence of diffuse emission makes it hard to distinguish different components. On the right, Figure 1.1 from Wang et al. (2013) shows the plasma morphology closer to the outer edge of accretion flow of Sgr A* (Bondi radius denoting the SMBHs sphere of gravitational influence, cyan dashed circle). IRS 13 and PWN G359.95-0.04 lie very close to this.

Enveloping these features is the supernova remnant (SNR) Sgr A East (ellipse seen in left column of Figure 1.1), an extended, nonthermal X-ray emitting structure spanning approximately $3' \times 2'$ (Maeda et al., 2002). The complexity of this region is further compounded by hundreds (if not thousands) of X-ray point and extended sources, contributing significantly to the diffuse X-ray background.

Despite abundant plasma available for accretion, measurements of the mass accretion rate near Sgr A*'s event horizon are orders of magnitude lower than expected from simple estimates of stellar wind plasma accretion (Marrone et al., 2007). This discrepancy indicates the existence of mechanisms that either eject material or prevent it from reaching the innermost accretion regions. Consequently, the SMBH exhibits luminosities significantly below predictions from standard thin-disk accretion models. However, historical evidence from X-ray light echoes reflected by nearby molecular clouds indicates that Sgr A* experienced higher accretion rates, and thus greater luminosities, only a few hundred years ago (Ponti et al., 2010; Marin et al., 2023). Thus, studying Sgr A* provides a unique window into radiatively inefficient accretion flows (RIAFs), feedback processes, and their episodic behavior, crucial for understanding galaxy evolution.

At the heart of this dissertation lie two interconnected themes. First, why is Sgr A* faint despite the abundant hot plasma in its vicinity? Is a significant fraction of inflowing gas lost via winds or jets before reaching the event horizon? Second, how does the complex surrounding environment, including the SNR Sgr A East, interact with and shape the SMBH's accretion and feedback processes? Addressing these questions requires both detailed spectroscopy of the accretion flow and innovative techniques for disentangling overlapping emission structures.

In Chapter 2, I test RIAF models against the highest-resolution Chandra/HETG spectrum of Sgr A*, deriving density and temperature profiles that refine earlier multiwavelength constraints (Yuan et al., 2003). Chapter 3 further compares this spectrum against smoothed particle hydrodynamic simulations, assessing whether colliding stellar winds alone can produce observed X-ray signatures (Cuadra et al., 2005, 2015).

Observations are complicated by line-of-sight overlap between the accretion flow and SNR Sgr A East, whose nonthermal emission is embedded within and interacting with the ambient plasma (Maeda et al., 2002). In Chapter 4, I apply Generalized Morphological Component Analysis (GMCA; Bobin et al. 2007; Ponti et al. 2019), an advanced data-driven technique, to 1.3 Ms of *Chandra* imaging data to isolate distinct emission components. This allows me to robustly disentangle Sgr A East's emission from the surrounding plasma, clarifying interactions between these overlapping astrophysical phenomena.

Ultimately, this work addresses the broader question: "How has Sgr A shaped, and been

shaped by, its complex surroundings across multiple scales?" To answer this, we leverage the *Chandra* science archive, which offers a treasure trove of high-resolution imaging and spectroscopy of Sgr A* that will not be replaced for decades. While proposed missions like AXIS may approach *Chandra*'s spatial resolution, no currently planned observatory replicates *Chandra*'s sub-arcsecond view of the Galactic Center combined with high-resolution gratings spectroscopy.

1.1 Sgr A*

Sgr A*, the SMBH at the center of the Milky Way, represents the nearest and best-resolved galactic nucleus available for detailed study. Approximately 8.1 kiloparsecs away, it is an exceptional laboratory to investigate the physical processes that govern black hole accretion, feedback mechanisms, and the intricate relationship between SMBHs and their surrounding environments. Despite residing within a gas-rich environment abundant with hot plasma supplied by massive WR stars, Sgr A* is extraordinarily dim, with a luminosity roughly 10^{-9} times its theoretical maximum luminosity. This stark contrast between expected and observed luminosities positions Sgr A* as a prototypical example of a low-luminosity AGN (LLAGN).

This section presents the tools and methods used throughout this dissertation by first reviewing the fundamentals of X-ray spectroscopy, then outlining the relevant *Chandra* instrumentation, next covering the basics of low-luminosity accretion, and finally examining past studies of the Sgr A* *Chandra* spectrum.

1.1.1 Basics of X-ray Spectroscopy

To characterize the conditions within the accretion environment around Sgr A*, X-ray spectroscopy[1] is employed as a powerful diagnostic tool. In the high-temperature, highly ionized plasma that permeates the central parsec, X-ray emission predominantly arises from bremsstrahlung radiation (free-free emission), along with strong emission lines from collisionally excited atomic transitions. The iron K-shell emission lines, spanning energies from approximately 6.4 keV (near-neutral fluorescence) to 6.97 keV (hydrogen-like Fe XXVI), provide particularly robust diagnostics for plasma temperature, density, ionization state, and dynamics. Hydrogen-like iron refers to Fe ions that have been stripped of all but one electron, analogous to the hydrogen atom, while helium-like iron retains two electrons, resembling the

[1]Please see the ASTRO-H cookbook for an excellent detailed overview:
https://heasarc.gsfc.nasa.gov/docs/xrism/documents/AHCookBook_v1.02.pdf

electronic structure of a helium atom. These simplified atomic configurations give rise to well-understood inner-shell transitions that produce strong, isolated X-ray lines ideal for plasma diagnostics. The strongest line at 6.7 keV arises from the Kα transition of He-like iron, where an electron transitions from the $n = 2$ shell to the $n = 1$ shell. This transition consists of three components: the resonance line, the intercombination line, and the forbidden line. The relative strengths of these lines are sensitive to both electron and temperature density.

In this dissertation, we exclusively use data from the *Chandra X-ray Observatory*, whose Advanced CCD Imaging Spectrometer (ACIS) provides moderate spectral resolution of $\Delta E \sim 100$–150eV across the Fe K band. At this resolution, individual components of the He-like Fe XXV triplet at 6.7 keV are typically blended into a single broad feature. Nevertheless, the presence and centroid of this complex still yield meaningful constraints on plasma temperature and ionization, especially when these features can be spatially isolated from Sgr A* using *Chandra*'s sub-arcsecond angular resolution, ensuring they are not contaminated by nearby emission.

At even higher temperatures, typically $T \gtrsim 10^8$ K, iron is further ionized to its hydrogen-like state, and a line at 6.97 keV from the Lyα transition of Fe XXVI becomes apparent. This feature indicates extremely hot plasma conditions, often associated with accretion shocks or strong outflows. Conversely, at lower temperatures or in neutral material, a line near 6.4 keV can be seen. This is the Fe Kα fluorescence line from near-neutral iron, generated when a K-shell electron is ejected, typically by X-ray photoioinization and an L-shell electron fills the vacancy. This line is often observed in reflection off cold molecular clouds illuminated by past X-ray flares from Sgr A*.

The interpretation of these lines relies on spectral modeling using atomic models such as APEC (Astrophysical Plasma Emission Code; Smith et al., 2001), which assumes a plasma in Collisional Ionization Equilibrium (CIE). In this framework, the observed photon flux at energy E is given by

$$F(E) = \int n_e n_H \Lambda(E, T, Z)\, dV,$$

where n_e and n_H are the electron and hydrogen densities, $\Lambda(E, T, Z)$ is the emissivity function dependent on energy E, temperature T, and metallicity Z, and the integral is over the emitting volume. The emissivity function $\Lambda(E, T, Z)$ encapsulates both continuum and line processes: thermal bremsstrahlung, radiative recombination continua, two-photon emission, and the discrete line emission from collisional excitation and de-excitation of ions. Its value at each energy depends on the ionization balance (set by T in CIE), the population levels of each ion, and the atomic rate coefficients. This information is generally drawn from large

databases such as AtomDB (Sánchez Díaz et al., 2024). Fitting the observed spectrum with an APEC model returns parameters such as temperature and abundance.

1.1.2 Chandra X-ray Observatory and Instrumentation

All data analyzed in this dissertation were obtained using the *Chandra X-ray Observatory*, NASA's flagship mission for high-resolution X-ray imaging and spectroscopy. Launched in 1999, *Chandra* carries two primary scientific instruments: the Advanced CCD Imaging Spectrometer (ACIS) and the High Resolution Camera (HRC), the former of which can be used in conjunction with either of two transmission grating assemblies, the Low Energy Transmission Grating (LETG) or the High Energy Transmission Grating (HETG). ACIS comprises two CCD arrays: ACIS-I for wide-field imaging and ACIS-S for spectroscopic readout, especially when paired with HETG.

ACIS offers moderate spectral resolution across the 0.5–10 keV band, with $\Delta E \sim 100$–150 eV near 6 keV. In cases where higher spectral resolution is required, the HETG can be deployed in front of ACIS-S to disperse incoming photons and obtain high-resolution spectra with $E/\Delta E \sim 100$–1000 over the 0.4–10 keV range. The HETG has significant sensitivity in its operational range, with a resolution of $E/dE \sim 170$ at 6.7 keV for point sources. However, the resolution is impacted by the extended and diffuse nature of Sgr A*. The HETG functions as a slitless spectrograph; dispersed light from the gratings forms a characteristic 'X' pattern, with photons landing directly onto the ACIS-S detector. Each photon is scattered in the dispersion direction corresponding to the energy of the photon. An order-sorting algorithm decides whether or not a photon at a particular dispersion angle came from the central source based on its CCD estimated energy ($\Delta E \sim 100$ eV), and assigns photons to different diffraction orders by the use of "banana plots" (Section 8.2 of *Chandra* Proposal Observatory Guide; CPOG [2]).

ACIS-I provides a 17' × 17' field of view. Although ACIS-I offers moderate spectral resolution ($E/\Delta E \sim 50$–100 across 0.5-8 keV) compared to the grating instrument configuration, its field of view fully encompasses the supernova remnant Sgr A East and its surroundings. Additionally, ACIS-I exhibits a lower instrumental background than ACIS-S. This combination of broader field of view and lower background makes ACIS-I more appropriate for subsequent analyses of Sgr A East in this dissertation, whereas ACIS-S's narrower field of view would miss key regions of the remnant.

[2] https://cxc.harvard.edu/proposer/POG/html/chap8.html

1.1.3 Accretion in the Low-Luminosity Regime

Despite residing in a gas-rich environment with abundant WR stellar winds injecting material at $\dot{M}_{\rm WR} \sim 10^{-5}\,M_\odot\,{\rm yr}^{-1}$ into the central parsec (Cuadra et al., 2008, 2015), SMBH Sgr A* exhibits luminosities orders of magnitude below theoretical expectations. This discrepancy originates in catastrophic inefficiencies in mass transport, where multiwavelength observations reveal that $\gtrsim$99% of gravitationally captured material never reaches the event horizon (Yuan & Narayan, 2014).

The accretion process begins at the Bondi radius, defined as the point where the black hole's gravitational potential dominates the gases thermal energy, resulting in gravitational capture and inflow:

$$R_{\rm B} = \frac{2GM_{\rm BH}}{c_s^2} \approx 10^5\,R_{\rm G} \approx 0.04\ {\rm pc} \tag{1.1}$$

for $M_{\rm BH} = 4.28\times10^6\,M_\odot$ (Gillessen et al., 2017), sound speed $c_s \sim 550\,{\rm km\,s^{-1}}$ (corresponding to a $kT \sim 1.3$ keV plasma; Baganoff et al., 2003), and with $R_{\rm G}$ denoting the gravitational radius, or $R_{\rm G} = \frac{GM}{c^2} = 2\times10^{-7}$ pc for Sgr A*. As shown in Baganoff et al. (2003), standard Bondi-Hoyle theory (Bondi, 1952) predicts an accretion rate at the Bondi radius of:

$$\dot{M}_{\rm Bondi} = \pi R_{\rm B}^2 \rho c_s \sim 10^{-5}\,M_\odot\,{\rm yr}^{-1} \tag{1.2}$$

This theoretical prediction is consistent with the estimated accretion rate from hydrodynamical simulations that trace the winds of WR stars in the central parsec (Cuadra et al., 2008, 2015). These simulations find that the WR stars collectively inject gas at $\dot{M}_{\rm WR} \sim 10^{-5}\,M_\odot\,{\rm yr}^{-1}$, implying a substantial supply of material available for accretion.

In standard thin disk accretion (Shakura & Sunyaev, 1973), 10% of the rest mass energy of the plasma is typically converted into radiation. With $10^{-5}\ M_\odot\ yr^{-1}$ of stellar winds being ejected close to the Bondi radius and therefore available to accrete, converting this to a luminosity, and assuming only 10% of the total luminosity is converted into X-rays gives $L_X = 0.1\times\eta\dot{M}c^2 = 5\times10^{38}$ erg s^{-1} for a typical $\eta = 0.1$. Meanwhile, the measured X-ray luminosity of Sgr A* in quiescence is $L_X \sim 10^{33}$ erg s^{-1} (Wang et al., 2013), five orders of magnitude lower. It is prudent to mention that the Bondi accretion rate serves as a lower limit, as it is based solely on the X-ray plasma that is accreted. However, while cooler atomic and molecular gas (e.g., through the CND and Sgr A West) also contributes to the total accretion flow, accounting for it cannot explain the orders-of-magnitude discrepancy between the predicted and observed luminosity (Yuan & Narayan, 2014).

This discrepancy has motivated the development of the RIAF model to describe the accretion environment of low-luminosity AGNs such as Sgr A*. First formalized by Narayan

& Yi (1994), the RIAF paradigm describes a hot, optically thin, geometrically thick (scale height $\sim$ radius) accretion flow in which most of the energy released by viscous or turbulent dissipation is retained in the ions and is advected, rather than radiated away. This paradigm predicts that outflows are inevitable; the high thermal energy results in powerful winds, so that the mass accretion rate $\dot{M}(r)$ decreases inwards as $\dot{M}(r) \propto r^s$, where $s \approx 0.5$–1 depending on the strength of the outflows (Yuan & Narayan, 2014).

Observational constraints on the accretion rate near Sgr A*'s event horizon come from Faraday rotation measurements of polarized submillimeter emission, which limit the accretion rate to $\lesssim 10^{-7} - 10^{-9} M_\odot \mathrm{yr}^{-1}$, depending on the assumed magnetic field geometry (Marrone et al., 2007). This implies that most of the material captured at the Bondi radius must be expelled or otherwise prevented from reaching the black hole. Numerical simulations have confirmed this two-zone structure, where a quasi-spherical inflow at large radii transitions to an outflow-dominated regime at $\sim 10^3 - 10^4\ R_g$ (Narayan et al., 2012; Yuan et al., 2015). Note that *Chandra* cannot resolve this radius, it's imaging resolution corresponds to approximately $10^5 R_g$.

Radiation from RIAFs arise via a combination of synchrotron, bremsstrahlung, and inverse Compton processes. Modeling the broadband Spectral Energy Distribution (SED) of Sgr A* in its quiescent state over multiple wavelengths offers valuable diagnostics of the underlying plasma conditions and electron distributions. A seminal RIAF-based model by Yuan et al. (2003) successfully reproduced the observed SED using a two-component plasma: a dominant thermal electron population responsible for bremsstrahlung and Comptonized synchrotron X-rays, and a minor non-thermal tail accounting for low-frequency radio emission and the variability seen in the infrared. The thermal X-ray emission is produced by electrons with $T \sim 10^8 - 10^{11}$K within $\sim 10^3 R_g$ of the black hole, while synchrotron radiation from nonthermal electrons explains both the flat radio spectrum and flaring behavior. Allowing for a RIAF s value that can vary with radius, Ma et al. (2019) found that $s \sim 0.05$ at small radii ($\lesssim 100\ R_g$), steepening to $s \sim 0.6$ at larger radii, consistent with increasingly powerful mass outflows. These results support a layered structure: a dense, nearly steady inflow at small scales surrounded by a turbulent, convective envelope that drives strong winds.

1.1.4 Past Studies of the *Chandra* Spectrum

The deepest X-ray spectroscopic observations of Sgr A* come from the 3 Ms *Chandra* Galactic Center X-ray Visionary Project (GCXVP), which used the HETG and ACIS to capture both spatially and spectrally resolved emission from the inner parsec. Wang et al. (2013) analyzed the zeroth-order spectrum within $1.5''$ of Sgr A*, excluding known transients, and

modeled it as optically thin thermal plasma with significant line emission. They found that the spectrum can be characterized by a two-temperature model, with $kT \sim 1$–2 keV and a higher temperature component of $kT \sim 4$ keV. The measured X-ray luminosity is $L_X \sim 2 \times 10^{33}$ erg s^{-1} (2–10 keV), consistent with earlier findings (Baganoff et al., 2003). The presence of a strong Fe Kα line at 6.7keV, consistent with highly ionized Fe XXV, indicates the plasma is collisionally ionized.

The high-resolution gratings spectrum from the GCXVP has further revealed detailed plasma diagnostics. Corrales et al. (2020) extracted the dispersed HETG spectrum of Sgr A*, carefully correcting for contamination from neighboring sources (e.g., the PWN G359.95−0.04 and IRS13E). They identified emission lines from highly ionized Fe (FeXX–XXIV), with some lines showing slight energy shifts, suggesting bulk motion or velocity broadening within the inner accretion flow.

In Chapter 2, we model this high-resolution spectrum with a RIAF framework that self-consistently incorporates the geometry and response of *Chandra* gratings.

1.2 The NSC Plasma Around Sgr A*

The stellar population of the GC is dominated by the NSC, which is one of the most massive and densely packed star clusters in our Galaxy. Within the central 4 pc, the NSC has an estimated mass of 10^7 $M_\odot$ (Schödel et al., 2011), which is *greater than the mass of the supermassive black hole itself.* Spectroscopic studies have identified about 180 young (2.5−6 Myr Lu et al., 2013), massive (up to 100 $M_\odot$; Paumard et al., 2006), WR and O/B stars. Early-type stars make up only 4% of the population of the NSC as a whole; most of the stars within 1 pc of Sgr A* are late-type giants, horizontal branch, or red clump stars (ages > 1 Gyr; masses between 0.5−4 $M_\odot$). However, if you look at the stars in the clockwise disk (Do et al., 2013), concentrated into the central 0.13 pc (Yelda et al., 2014), the young stars make up 20%−50% of the population. The burst of recent star formation that creates these massive stars is estimated to have produced 10^4 $M_\odot$ of stars (Lu et al. 2013).

The early-type stars, despite making up small fractions of the NSC, have had large impacts on the GC. The mini-spiral of ionized gas and hot dust, made up of three main streamers funneling material in from the CND (1.5−3 pc away from Sgr A*; Genzel et al., 2010; Tsuboi et al., 2017), is likely heated via shocks or photoiozation by the NSC. The S-cluster, made up of mainly B-type stars orbiting within the innermost arcsecond have been monitored since 1992, and were used to measure the mass of Sgr A* (see, e.g. Ghez et al., 1998; Genzel & Stutzki, 1989), with definitive evidence coming from the orbit of the star S2. And finally, as previously mentioned, the main bath of plasma from which Sgr A* accretes arises from the

massive outflows suppplied by WR star winds within the NSC core.

The inner edge of the CND, at a radius of 1.5 pc, is impacted by winds and supernovae from the NSC, potentially causing instabilities and streams of gas to peel off and fall inwards towards Sgr A* (Morris & Serabyn, 1996; Hsieh et al., 2019). Recent observations have provided evidence of high-velocity gas clouds being drawn towards Sgr A*, suggesting that material from the CND is indeed being accreted, albeit at an inefficient rate (Gillessen et al., 2019).

Two major groups have conducted hydrodynamic simulations of the ~ 30 WR stars orbiting within the central parsec, using the precise stellar positions and velocities determined from infrared observations (Paumard et al., 2006). The first group (Cuadra et al., 2008, 2015; Calderón et al., 2020; Russell et al., 2017) employs both smoothed particle hydrodynamics (SPH) and adaptive mesh refinement (AMR) methods to model the stellar wind interactions. Their simulations typically resolve scales from the Bondi radius ($10^5\ R_g$) down to 1000 R_g, focusing on how wind-wind collisions generate the observed hot plasma ($kT = 1-2$ keV) while tracking the resulting accretion flow toward Sgr A*. These works have demonstrated the formation of transient, filamentary structures that can form from clumps and the importance of cooling physics in shaping the accretion flow (Calderón et al., 2020). In contrast, the second group (Ressler et al., 2018, 2020a,b, 2023) employs magnetohydrodynamic (MHD) and general relativistic MHD (GRMHD) simulations that probe much smaller scales ($\leq 100 R_g$). Their models incorporate magnetic fields and relativistic effects, revealing how magnetized outflows can suppress accretion (Ressler et al., 2020a) and produce flaring events consistent with Sgr A*'s observed variability.

Both approaches reproduce observed accretion rates at multiple scales: $\dot{M} \sim 10^{-5}\ M_\odot\ \mathrm{yr}^{-1}$ near the Bondi radius (Cuadra et al., 2005) and $\dot{M} \sim 10^{-8}\ M_\odot\,\mathrm{yr}^{-1}$ closer to the event horizon (Ressler et al., 2018). The simulations both start from the same wind-fed supply of 30 Wolf–Rayet stars, but differ in how they handle angular momentum, resolution, and cadence. In the Smoothed Particle Hydrodynamics (SPH)/Adaptive Mesh Refinement (AMR) runs (e.g., Cuadra et al., 2015; Calderón et al., 2020), all angular momentum redistribution occurs via collisions and partial cancellation of the injected wind streams (no explicit viscosity or magnetic torques). On the other hand, the grid/MHD simulations (e.g., Ressler et al., 2018) add magnetic effects that remove angular momentum. Spatially, the SPH models resolve gas down to a sink radius of order $10^4 R_g$ ($0.1''$), whereas the nested-grid Athena++ calculations reach $\leq 300 R_g$ before imposing an inner boundary. Temporally, SPH uses adaptive timesteps from days up to $\sim$ 1yr, while the grid and MHD simulations employ $\Delta t \sim$ hours–days with outputs every few years (Ressler et al., 2020a), and the horizon–scale GRMHD (Ressler et al., 2020b) runs use sub-second timesteps and minute-scale outputs

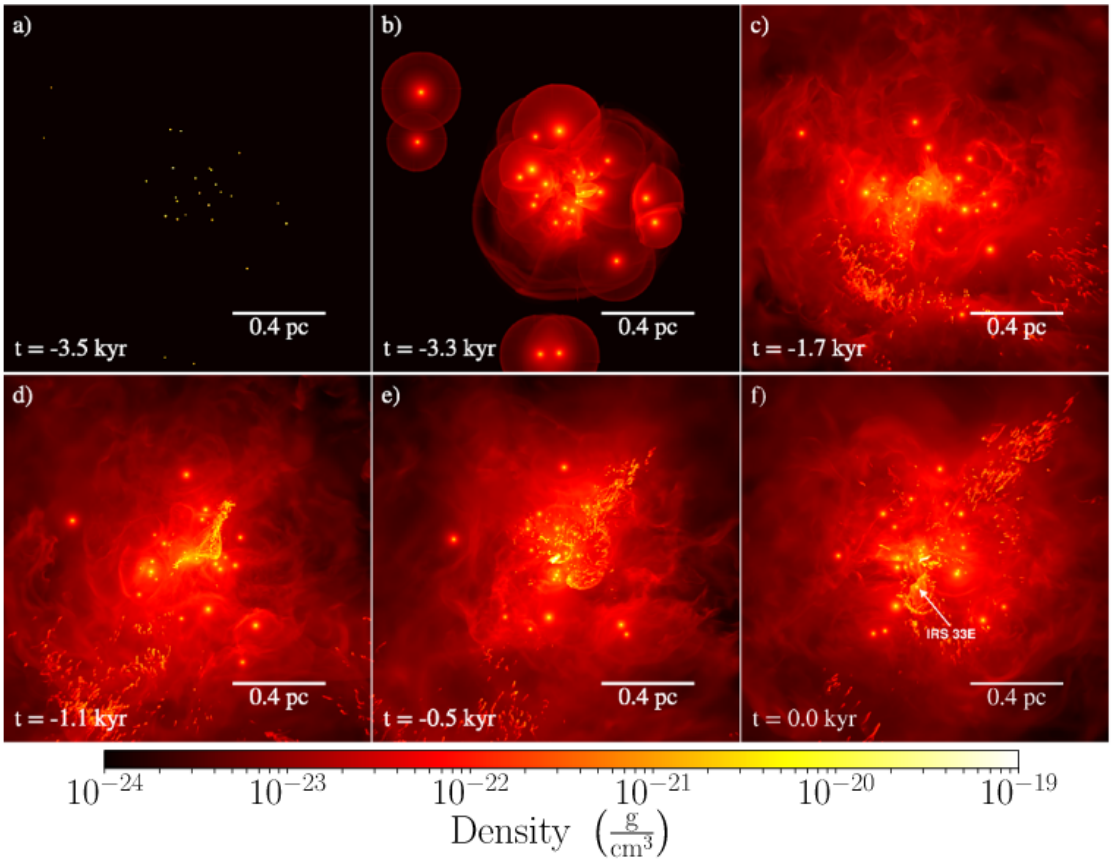


Figure 1.2: Figure 2 from Calderón et al. (2020), where the dots are the WR stars of interest, and the plasma clearly has a complex filamentary structure. In the center, because of extended timescales, a cool (T = 10^4 K) disk forms in the $T \sim 10^{6-7} K$ plasma.

over $\sim$ 0.24yr to resolve rapid relativistic variability. However, neither approach yet reproduces the shape imaged by the EHT (Event Horizon Telescope; Event Horizon Telescope Collaboration et al., 2022a).

One particularly interesting puzzle is the disputed presence of a cold gas disk ($T \sim 10^4$ K). The existence of the disk seems plausible; collisions between the stellar winds may have provided a mechanism for cooling and condensing gas into colder phases. The Atticama Large Millimeter Array (ALMA), a radio telescope array, detected H30α emission that initially suggested a compact (0.004 pc) disk structure (Murchikova et al., 2019), since confirmed by line shifts in other Hydrogen lines that imply the presence of a small rotating disk (Yusef-Zadeh et al., 2020). However, subsequent Brγ observations imposed flux limits 80 times below the predicted values, challenging this interpretation (Ciurlo et al., 2021).

Theoretical work reveals this dichotomy may stem from timescale dependencies in accretion flow evolution. AMR simulations (with foundations from Cuadra et al. (2015))

demonstrate that sustained inflows (>3000 yr) can produce cold disks through radiative cooling instabilities (Calderón et al., 2020), whereas comparable SPH simulations at shorter timescales show no such structure (Russell et al., 2017). The extended AMR simulations and the formation of the disk (clearest in panel e) are shown in Figure 1.2. This discrepancy raises fundamental questions about numerical methodologies (e.g., SPH smoothing lengths versus AMR grid resolution) and physical conditions (e.g., metallicity-dependent cooling, thermal conduction) required for disk formation.

In Chapter 3, we address these questions by (1) extending SPH simulations to 3000 yr timescales to test for delayed disk emergence, and (2) searching for corresponding X-ray signatures in *Chandra* grating spectra, particularly the velocity-shifted Fe lines reported by (Corrales et al., 2020). While we show that a cool disk can form in the SPH simulations, we note that the Ressler group is unable to form a disk even after extending the timescales. We find that the difference is in the cooling prescription, and this is explored in depth in recent simulations (Calderón et al., 2025).

1.3 Sgr A East

Overlapping (along our line-of-sight) the previously mentioned astrophysical structures - Sgr A*, Sgr A West, the CND – is Sgr A East, a prominent, non-thermal X-ray emitting structure (see, e.g. Yusef-Zadeh, 1986; Wang, 2022; Maeda et al., 2002) extending several arcminutes around Sgr A* (Maeda et al., 2002). Sgr A East is widely believed to be a supernova remnant (SNR). Its irregular morphology and non-thermal spectrum are consistent with synchrotron emission from accelerated particles in the shock waves produced by a supernova explosion (Wang, 2022). Notably, Sgr A East appears to be interacting with the surrounding molecular clouds (Yusef-Zadeh et al., 1999a; Tsuboi et al., 2019), potentially influencing the density and temperature of the Interstellar Medium (ISM) in its vicinity (Morris & Serabyn, 1996). The spatial proximity of Sgr A East to Sgr A* raises questions about potential past interactions or interactions with the accretion flow.

This section introduces Sgr A East by first outlining the general evolutionary phases of SNRs, then reviewing past observational and theoretical studies of Sgr A East, and finally describing the signal separation technique used to disentangle this remnant from the Sgr A* accretion flow.

1.3.1 Brief Overview of Supernova Remnants

The evolution of a SNR is characterized by four distinct phases. Initially, the free expansion phase is dominated by the unimpeded outward motion of ejecta, with density profiles scaling as $\rho \propto v^{-n}$ ($n \sim 7$ for Type 1a, $n \sim 9-12$ for core collapse). A reverse shock forms, heating the ejecta while transferring energy to the surrounding medium. As the swept-up mass exceeds the ejecta mass, the SNR transitions to the Sedov-Taylor phase, where adiabatic expansion governs the dynamics. Here, energy is conserved (aside from cosmic-ray losses), producing a hot interior and a cooler shell. As the SNR sweeps up material, it starts to lose energy to radiation, and energy conservation no longer holds. Once radiative cooling becomes significant ($T \leq 10^5$ K, $v_{\rm shock} \sim 200$ km s^{-1}), the SNR enters the snowplow phase, where where momentum is conserved. This phase generates dense, optically bright shells surrounding an isothermal, pressure-equilibrated interior of metal-rich ejecta. Finally, in the merging phase, the shock properties converge with those of the turbulent ISM.

SNRs typically have "shell" like or "center-filled" structures. However, the small but growing class of mixed-morphology supernova remnants (MMSNRs) often exhibit concentrated thermal X-ray emission from their interiors, with far more extended radio shells (Vink, 2012). Their central thermal emission may arise from evaporating cloudlets via thermal conduction (White & Long, 1991a), while metal enrichment (Lazendic & Slane, 2006) and near-equilibrium plasma state (Kawasaki et al., 2005) differentiate them from both younger (non-equilibrium) and older (fully mixed) SNRs. Alternative mechanisms like adiabatic expansion into a dense circumstellar medium or anisotropic thermal conduction (inhibited by magnetic fields) may explain observed overionization, where rapid cooling outpaces recombination (Vink, 2012). MMSNRs often exhibit associations with molecular clouds and 1720 MHz OH masers, supporting the idea that a dense circumstellar medium profoundly influences their evolution.

1.3.2 Past studies of Sgr A East

Sgr A East was first imaged[3] with $6'' \times 18''$ resolution (Ekers et al., 1975) and was suggested to be a supernova remnant based on its nonthermal spectrum. Yusef-Zadeh further characterized this source between 1980 and 2000 (see, e.g., Yusef-Zadeh, 1986; Yusef-Zadeh et al., 1999a, 1996, 2001, 1997), finding that the SNR is likely in the plane of the Galactic Center, within 10−30 pc of Sgr A*. Assuming the SNR is ∼8 kpc away, the expansion velocity was estimated to be $100 - 200$ km s^{-1} and the age to be 10,000 years, consistent with a SNR in

[3]The image was called the WORST (Westerbork Owens Valley Radio Synthesis Telescope) image, named as such as the beam shape apparently looked like a sausage, or wurst.

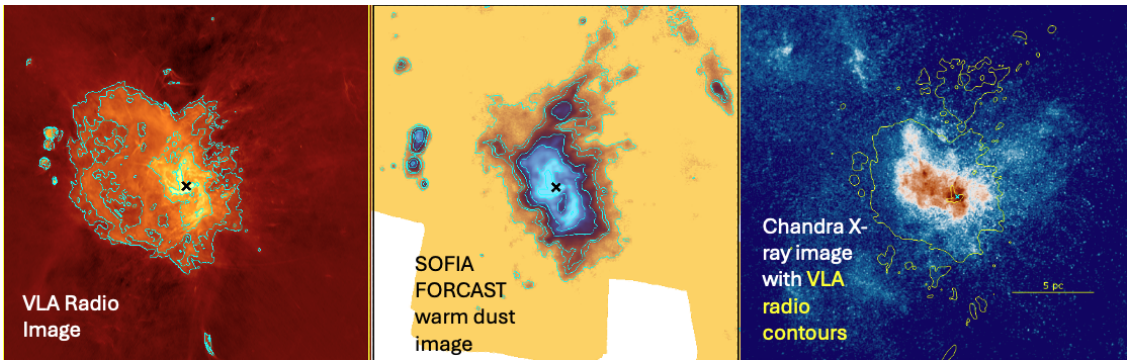


Figure 1.3: Image of Sgr A complex in low, medium, and high energy bands. One can see the Sgr A East SNR in the radio and X-ray, while intermediate wavelengths generally capture components likely associated with the NSC plasma and minispiral as opposed to the remnant. VLA image from (Zhao et al., 2016); SOFIA Forcast data from (Lau et al., 2015).

the Sedov-Taylor phase.

X-ray observations with *Chandra* provide more insight. The remnant has very concentrated 6.7 keV Fe Kα emission compared to the radio shell, with an X-ray centroid offset by $\sim$5 pc from Sgr A* (Maeda et al., 2002; Park et al., 2004). The radio and X-ray images can be seen in Figure 1.3, where the X-ray image has the radio contours overlaid in yellow. The X-ray core appears to extend only 2 arcmin (Maeda et al., 2002), in comparison to the radio shell which is 10 arcmin across (Yusef-Zadeh, 1986). Deriving a velocity from the Fe Kα line broadening yields a velocity dispersion of 1000 km s^{-1}. These two papers postulate that the morphology of the remnant implies it exploded asymmetrically into a dense central environment or has been influenced by the GC's gravitational potential. Energetics derived from the remnant in X-rays signify overionization, which could be due to recent re-energization by a past burst of Sgr A* (Ono et al., 2019; XRISM Collaboration, 2024).

The discovery of the Cannonball pulsar (PSR J1746-2856) may provide constraints on Sgr A East's age and formation history. Zhao et al. (2013) identified this young, high-velocity pulsar (moving at $\sim$500 km s^{-1}) along Sgr A East's northwestern edge, with its trajectory suggesting it was launched from near the remnant's geometric center during the supernova explosion. Zhao et al. (2013) traced its trajectory back to the remnant's geometric center, implying an age of approximately 9,000 years. Nynka et al. (2013) detected non-thermal X-ray emission up to 30 keV from the Cannonball using *NuSTAR*, with spectral and spatial characteristics consistent with a PWN, although no pulsed signal was detected. These findings support the scenario where Sgr A East resulted from a supernova explosion that also produced the Cannonball.

Maeda et al. (2002) analyzed *Chandra* observations of Sgr A East, interpreting the data

with a simplified dynamical evolution model. They proposed that Sgr A East is a supernova remnant approximately 10,000 years old, expanding into a dense interstellar medium. The X-ray emission was found to be rich in heavy elements, supporting the hypothesis of a core-collapse supernova origin. However, this study did not include hydrodynamic simulations. Building on this, Zhou et al. (2021) carried out deep, spatially resolved spectroscopy and found elemental abundances (low Si/Fe and S/Fe but high Mn/Fe and Ni/Fe) that are inconsistent with either a standard core-collapse or "normal" Type Ia supernova. Instead, these ratios uniquely match a pure turbulent-deflagration (Type Iax) explosion of a Chandrasekhar-mass white dwarf. Finally, Ehlerová et al. (2022) ran three-dimensional hydrodynamic simulations in a realistic Galactic-Center environment (including the nearby 50 $\mathrm{km\,s^{-1}}$ molecular cloud and the nuclear stellar wind) and showed that only an explosion 10 kyr ago can reproduce both the observed shell size and the bright northeastern X-ray ridge; models younger than 5 kyr fail to match the remnant's extent.

1.3.3 Poissonian Generalized Morphological Component Analysis (pGMCA)

Generalized Morphological Component Analysis (GMCA) is a blind source separation technique that decomposes multi-dimensional astronomical datasets into distinct spatial and spectral components. Originally designed to isolate the Cosmic Microwave Background from foreground components (Bobin et al., 2015), GMCA has been adapted to separate overlapping sources in X-ray astronomy, such as synchrotron emission and thermal plasma emission in supernova remnants (Picquenot et al., 2019).

GMCA formulates the problem of component separation as a linear decomposition of an observed data cube into distinct spatial and spectral components. Given a data cube $X \in \mathbb{R}^{m\times n}$, where m is the number of spectral bins, or energy channels, and each of the n columns corresponds to a spatial pixel (flattened from the 2D image), the model assumes the data can be approximated as

$$X = AS + N,$$

where $A \in \mathbb{R}^{m\times r}$ is the spectral mixing matrix, with each column r representing the spectrum of one astrophysical component, and $S \in \mathbb{R}^{r\times n}$ is the source matrix, with each row r giving the corresponding spatial maps (in the wavelet domain). The term N accounts for observational noise. GMCA iteratively solves for A and S by alternating between estimating the spatial maps S given current spectral estimates A, and updating the spectra A based on the current spatial maps S, while promoting sparsity in the spatial domain to isolate

physically meaningful structures.

The primary insight behind GMCA is the assumption of sparsity: astrophysical structures typically have a concise representation when viewed in an appropriate wavelet transform, such as the Starlet transform (Starck et al., 2007). Sparse representation means most of the information about an astrophysical source is captured by a few significant wavelet coefficients, making the sources easier to distinguish and separate even if they overlap spatially.

To find the best-fitting model, GMCA solves an optimization problem similar in spirit to chi-squared minimization familiar in astronomical data analysis. Specifically, GMCA minimizes a "loss function" that quantifies the difference between the model AS and the observed data X, while also including a regularization term to promote sparsity:

$$\min_{A,S} \|X - A\,S\|_F^2 \; + \; \sum_{i=1}^{r} \lambda_i \, \|S_i\|_1$$

where the first term ensures the reconstructed sources match the observed data (akin to the traditional chi-squared fitting), and the second term enforces sparsity. In a Bayesian interpretation, this sparsity constraint can be viewed as imposing a prior that the astrophysical sources in question are independent in the spatial-spectral domain.

For our work decomposing overlapping sources in the GC, we utilize pGMCA, or Poissonian GMCA. Unlike standard GMCA, which assumes Gaussian noise and minimizes the squared error (i.e., the Frobenius norm) between the model and the data, pGMCA modifies the loss function to account for Poisson statistics. This is useful in the X-ray regime, where photon counts follow a Poisson distribution and Gaussian assumptions would misrepresent the noise properties, particularly in low-count regimes.

While it aims to decompose complex data into simpler building blocks akin to Principal Component Analysis (PCA) and Independent Component Analysis (ICA), GMCA relies on different assumptions. PCA finds orthogonal directions that capture the greatest variance in the data, making it fast and robust for dimensionality reduction and denoising, but its components often blend multiple physical sources. ICA goes a step further by enforcing statistical independence among recovered signals, which can separate non-Gaussian, independent sources (for example, isolating the cosmic microwave background from instrument noise), but it breaks down when astrophysical components are not truly independent and is sensitive to noise and initialization. GMCA replaces the independence requirement with a sparsity assumption in a wavelet domain: because many astronomical structures (e.g., filaments, clumps, shock fronts) concentrate their information into a few significant wavelet coefficients, GMCA's optimization can disentangle spatially overlapping emission components that PCA and ICA struggle to separate.

In Chapter 4, I apply pGMCA to ACIS-I observations of the GC. This analysis is to improve our understanding of the X-ray plasma environment by disentangling overlapping emission components and isolating distinct physical mechanisms, enabling the extraction of spectrally distinct images across the central 7 arcminutes and revealing the spatial structure of multiple plasma populations. By comparing these results with multiwavelength datasets, I characterize the X-ray morphology of the supernova remnant and investigate its interaction with the surrounding medium, offering new insights into its formation and evolution within this complex environment. Furthermore, by characterizing the spatial-spectral distribution of different plasma components, I will derive more precise estimates of shock velocities and ambient densities, thereby providing constraints for future hydrodynamic simulations.

1.4 Summary

The unusually low luminosity of Sgr A* (Baganoff et al., 2003), despite the abundant plasma supplied by stellar winds from the NSC, remains a central puzzle in Galactic Center astrophysics. RIAF models suggest that much of this material is expelled before reaching the black hole, but the mechanisms responsible for such outflows are not fully understood (Wang et al., 2013). At the same time, the NSC itself presents dynamical challenges, including a mix of young and old stellar populations and complex rotation patterns that influence the surrounding plasma (Genzel et al., 2010). Hydrodynamic simulations have begun to capture these effects, modeling the interaction between stellar winds and the SMBH's gravitational potential while probing the debated existence of a cool, rotating disk near Sgr A* (Calderón et al., 2020; Murchikova et al., 2019; Ciurlo et al., 2021). Adding to the complexity, the MMSNR Sgr A East exhibits unusual X-ray and radio properties that may reflect interactions with both the ambient medium and the dense stellar population of the NSC. Along our line of sight, the emission from Sgr A*, Sgr A East, and the NSC significantly overlap, creating observational challenges but offering a unique opportunity, given the availability of high-resolution *Chandra* data, to probe accretion physics, stellar feedback, and supernova remnant evolution in a uniquely dense and energetic environment.

In this thesis, I address these phenomena through two complementary approaches. First, in Chapter 2, I analyze high-resolution X-ray spectra of Sgr A* using *Chandra* HETG data from the Chandra X-ray Visionary Project (GCXVP) to constrain the properties of its accretion flow. Although grating spectroscopy offers exceptional diagnostic power for point sources, the extreme source crowding in the Galactic Center introduces significant observational complexities. Accurate analysis requires meticulous separation of Sgr A*'s emission from contaminating sources, including the PWN G359.95-0.04 and the IRS 13E stellar clus-

ter. I also carefully account for the unique geometry of *Chandra*'s HETG instrument and incorporate advanced forward modeling techniques. In Chapter 3, I compare both analytical RIAF models and modern hydrodynamic simulations with the observational data to constrain the detailed structure of the accretion flow.

In Chapter 4, I apply new data-driven component separation methods to disentangle the overlapping emission components from Sgr A East and the ambient plasma surrounding Sgr A*. Incorporating multiwavelength constraints, I disentangle Sgr A East from the Sgr A* accretion flow for the first time. I also separate overlapping plasmas at different temperatures along the line of sight, offering key insights into how these distinct components coexist within the complex central region.

Finally, in Chapter 5 I discuss the implications of these findings in the context of the field and relate them to complementary works, while outlining promising directions for future research with new and upcoming X-ray observatories.

CHAPTER 2

Modeling the High-Resolution Spectrum of Sgr A's accretion flow with a Radiatively Inefficient Accretion Flow

The contents of this chapter were published in The Astrophysical Journal, Volume 947, Issue 1, in collaboration with Lia Corrales, Sera Markoff, Michael Nowak, Daryl Haggard, Daniel Q. Wang, Joey Neilsen, Christopher M. P. Russell, Diego Calderón, Jorge Cuadra, and Fred Baganoff in the *Astrophysical Journal* volume 974, issue 1, and can be found in full at this link.

2.1 Abstract

The extreme low-luminosity supermassive black hole Sgr A* provides a unique laboratory in which to test radiatively inefficient accretion flow (RIAF) models. Previous fits to the quiescent *Chandra* ACIS-S spectrum found a RIAF model with an equal inflow-outflow balance works well. In this work, we apply the RIAF model to the *Chandra* HETG-S spectrum obtained through the *Chandra* X-ray Visionary Program, which displays features suggestive of temperature and velocity structures within the plasma. A comprehensive forward model analysis accounting for the accretion flow geometry and HETG-S instrumental effects is required for a full interpretation of the quiescent *Chandra* HETG-S spectrum. We present a RIAF model that takes these effects into account. Our fits to the high-resolution gratings spectrum indicate an inflow balanced by an outflow ($s \sim 1$) alongside a temperature profile that appears shallower than what would be expected from a gravitational potential following $1/r$. The data require that the abundance of Iron relative to solar is $Z_{Fe} < 0.32 Z_{\odot}$ (90% credible interval), much lower than the 2 $Z_{\odot}$ metallicity measured in nearby late-type giants. While future missions like *NewAthena* will provide higher spectral resolution, source separation will continue to be a problem. Leveraging *Chandra*'s unparalleled spatial res-

olution, which is not expected to be surpassed for decades, remains essential for detailed investigations of the densely populated Galactic Center in X-rays.

2.2 Introduction

Active Galactic Nuclei (AGN) feedback is an important mechanism by which star formation can be quenched (see, e.g. Weinberger et al., 2018; Vogelsberger et al., 2014; Fabian, 2012), significantly shaping galaxy properties over cosmic time. However, even in low-luminosity states, mechanical feedback from radiatively inefficient SMBHs can still have a significant effect on galactic evolution (Yuan et al., 2018). Low-luminosity AGNs (LLAGNs; $L \leq 10^{39} - 10^{40}$erg/s) constitute the majority of observed AGN in the nearby universe (Ho, 2008). The closest supermassive black holes, detectable by modern instruments such as Keck, Hubble, EHT, and *Chandra*, are M31* ($L \sim 10^{38}$ erg/s; $M_* \sim 10^8 M_\odot$; Bender et al., 2005) and our own Milky Way's Sagittarius A* (Sgr A*; $L_X \sim 10^{33}$ erg/s; $M_* = 4.1 \times 10^6 M_\odot$; Baganoff et al., 2003). Both are categorized as low-luminosity active galactic nuclei (LLAGN). The proximity of Sgr A* allows for in-depth investigations into the dynamics between supermassive black holes and their surroundings, deepening our understanding of LLAGNs.

Sgr A* displays many behaviours that make it a dynamic astrophysical laboratory. The SMBH has significant time variability, with flares that reach 100 - 1000 times the quiescent luminosity in both the X-ray (on average 1 per day; Nowak et al., 2012; Neilsen et al., 2013; Haggard et al., 2019) and NIR (4 per day; Schödel et al., 2011). During non-flaring periods, the SMBH maintains a low luminosity of approximately $L_X \sim 10^{33}$ erg s^{-1} $= 10^{-10} L_{\rm edd}$ (Baganoff et al., 2003; Wang et al., 2013; Corrales et al., 2020), despite the material available at the Bondi radius ($\sim 4-5''$; see Section 2.4.1.2). Around 30 massive Wolf-Rayet (WR) stars orbit within 0.4 pc ($\sim 10''$) with mass loss rates of $\sim 10^{-5}-10^{-6} M_\odot$ yr^{-1} (Martins et al., 2007; Cuadra et al., 2015), providing plasma for Sgr A* to accrete. Meanwhile, Faraday rotation measurements and Event Horizon Telescope (EHT) models closer to the horizon ($\sim 4 \times 10^{-6}$ pc) show a mass accretion rate closer to $10^{-9} - 10^{-8} M_\odot$ yr^{-1} (Marrone et al., 2007; Event Horizon Telescope Collaboration et al., 2022b, 2024). Advection-dominated accretion flows (ADAFs; Narayan & Yi, 1994; Narayan & McClintock, 2008), in which a significant portion of the accretion energy is retained in ions and electromagnetic radiation losses are minimal, were developed to explain the observed low-luminosity of Sgr A*. However, measurements of the low accretion rate (in addition to issues with self-similarity in the ADAF solution) suggest that advection-dominated inflow-outflow solutions (ADIOS; Blandford & Begelman, 1999, 2004), where some of the accreted material is expelled in an outflow, may better

describe the physical processes in the Sgr A* accretion flow. Magnetic fields have also been theorized to prevent matter from flowing into the inner regions (Pang, 2011), but their importance is unclear; modelling of EHT data finds that magnetic fields are required, but some general relativistic magnetohydrodynamic (GRMHD) simulations do not support this scenario (Ressler et al., 2020b).

Regardless of underlying physics, optically thin, quasi-spherical accretion flows with a variety of internal conditions can be parameterized with the Radiatively Inefficient Accretion Flow (RIAF) prescription (Quataert, 2002; Yuan et al., 2003; Yuan & Narayan, 2014). RIAFs typically adopt a simple power-law to describe the mass accretion rate, $\dot{m} \propto r^s$, and material density, $n \propto r^{-3/2+s}$, where $s = 0$ corresponds to classical Bondi accretion and $s \sim 1$ indicates an inflow balanced by an outflow (Begelman, 2012). Observations of the SMBH at different wavelengths probe different scales: the event horizon can be seen through long baseline radio interferometry, radio polarization probes within $\sim 10\ R_g$ (where $R_g = GM_*/c^2$), and the quiescent X-ray emission originates from $10^4 - 10^6 R_g$, around the Bondi radius. Consequently, the multiwavelength spectral energy distribution (SED) offers comprehensive insight into the underlying physics, potentially exhibiting different s values at different radii. One model that successfully explains the multiwavelength SED of Sgr A* and can account for the observed flaring behavior is Yuan et al. (2003), where thermal electrons with $s \sim 0.3$ in collisional ionization equilibrium (CIE) transfer $\sim 1.5\%$ of their energy to a population of non-thermal electrons. Newer fits incorporating different boundary conditions have found $s \sim 0.05$ within $30R_g$ and $s \sim 0.6$ closer to R_{Bondi} (Ma et al., 2019), indicating that the outflow increasingly dominates as distance from the SMBH increases. Simulations confirm this, with many requiring some sort of outflow that dominates outside $R > 100R_g$ (Yuan & Narayan, 2014; Ressler et al., 2018; Dexter et al., 2020; Chatterjee et al., 2021).

To investigate the X-ray properties of Sgr A*, the *Chandra* X-ray Visionary Program (PIs: Markoff, Nowak, & Baganoff)[1] obtained 3 Ms of *Chandra* exposures in 2012, utilizing the *Chandra* High Energy Transmissions Grating Spectrograph (HETG-S; Canizares et al., 2005). Other works focus on deciphering the time variability of Sgr A*, but here we summarize results from previous analysis of the quiescent emission. Wang et al. (2013) (hereafter W13) analyzed the zeroth order (non-dispersed) quiescent spectrum and found emission lines corresponding to a plasma with $T \sim 3.5$ keV and a RIAF $s \sim 1$. The plasma being accreted onto the SMBH primarily originates from shocked, colliding stellar winds from the 30 WR stars in the central parsec. Roberts et al. (2017) performed hierarchical Bayesian fits, with initial conditions matching the WR orbits, to the 2D image of Sgr A* with hydrodynamic models. They found that 99% of the accreted mass is ejected in a polar outflow before reach-

[1] https://www.sgra-star.com/

ing the horizon. Smoothed particle hydrodynamics (SPH) simulations of these stellar winds are also able to recreate the observed X-ray spectrum (Russell et al., 2017). We address whether these simulations are better able to reproduce the observed HETG-S spectrum in the following chapter.

Studying the central $\sim 5-10$ arcseconds ($1-2\times10^6 R_g$) around Sgr A* in X-rays poses a challenge due to high extinction and the presence of nearby contaminating objects. Extracting the high-resolution gratings spectrum requires meticulous management of flares, point sources, and nearby contaminants. Although use of *Chandra*'s gratings allows for increased spectral resolution compared to the CCD, the dispersed light from the slit-less gratings intertwines with emissions across the entire field-of-view, which is not a problem for bright point sources. Meanwhile, Sgr A* exhibits X-ray brightness comparable to that of the extended and diffuse pulsar wind nebula (PWN) G359.95-0.04 and the massive star cluster IRS 13E, both of which lie an angular projected distance of $4''$ (only 8 *Chandra* pixels) from the SMBH and appear to extend into the Bondi radius of the accretion flow. Using custom background regions and non-standard extraction techniques to obtain the high-resolution spectrum, Corrales et al. (2020) identified various line features within the Fe Kα complex potentially associated with Fe XXVI, Fe XXV, Fe XX, Fe XXII, and Fe XXIII. The detection of multiple ionization states of Iron suggests the possibility of probing multiple temperature layers within the accretion flow. Moreover, apparent line shifts suggest the potential for investigating the velocity structure and orientation of the accretion flow using the high-resolution spectrum. However, this line structure could be a stochastic artifact, as each spectral bin only contains a handful of counts. Therefore, a comprehensive forward model analysis encompassing the geometry, instrumental effects, and anticipated velocity structure within the Sgr A* accretion flow is imperative for a complete interpretation of the *Chandra* HETG-S spectrum.

The goal of this work is to fit the *Chandra* HEG spectrum with a RIAF model to investigate whether the apparent lower energy line features can be explained by temperature and density structure in the Sgr A* accretion flow. We build on the previous work of Corrales et al. (2020), fitting the high-resolution quiescent X-ray spectrum with careful consideration of the system geometry, *Chandra* optics, and the HETG order-sorting algorithm. Focusing on the Fe Kα complex, the strongest line features found in the HEG spectrum (Corrales et al., 2020), we fit the 6.4 - 7.2 keV spectrum with a RIAF model to constrain the temperature and density profiles of gas about $10^4 R_g - 10^6 R_g$ from the SMBH. In Section 2, we introduce the unique challenges presented by the *Chandra* HETG instrument and the high-resolution spectrum used in this work. Section 3 outlines the procedure used to calculate the plasma emission and describes how we incorporated the unique geometry and spectral

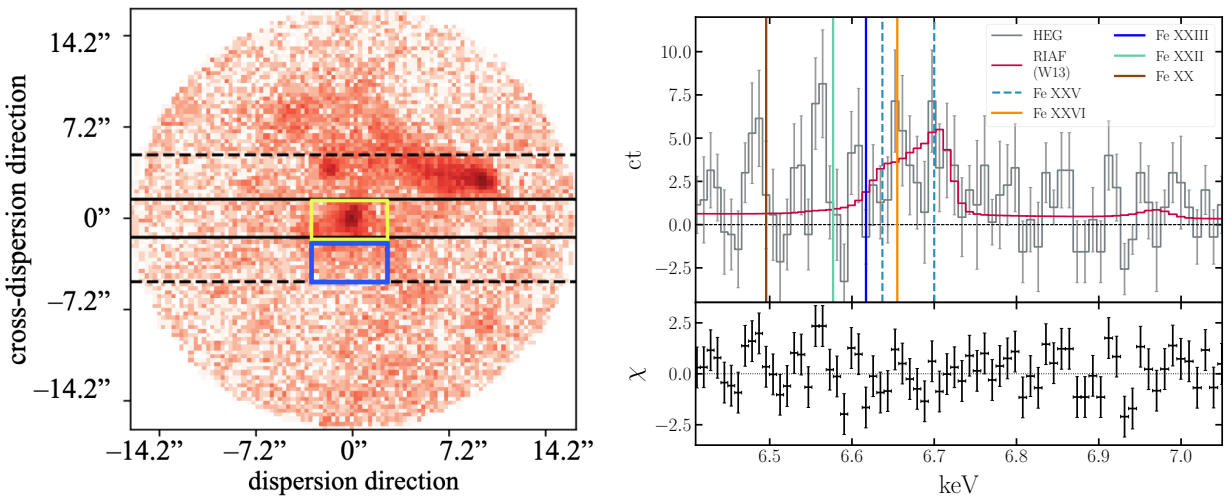


Figure 2.1: LEFT: Adaptation of Figure 1 from Corrales et al. (2020) showing the cleaned, quiescent 2 - 8 keV data for one roll angle. The 0th order (non-dispersed) image is displayed in HEG coordinates with the dispersion direction on the x-axis and the cross-dispersion direction on the y-axis. Solid black lines bracket the source extraction region out to 1.5″, while the dashed lines denote the background extraction region, 5″ away from Sgr A* in the cross-dispersion direction. The yellow and blue boxes refer to the effective regions of the image that contribute to the source and background spectra, respectively. RIGHT: Adapted from Figure 6 of Corrales et al. (2020), showing the the combined, unbinned, stacked and background subtracted HEG ±1 counts histogram in black. The best-fit RIAF model from W13 is plotted in red, showing that the background subtracted spectrum has additional structure. The Fe XXV doublet wavelengths are plotted with blue dashed lines, and Fe XX, Fe XXII, Fe XXII, and Fe XXVI are plotted in brown, teal, blue, and orange lines respectively.

extraction techniques into our forward model. In Section 4, we fit the data and discuss our interpretations, and end with conclusions. In the following chapter, we extend our analysis by fitting the data to synthetic spectra built on hydrodynamic simulations based on Cuadra et al. (2015) and Russell et al. (2017) of the nearby WR stellar winds, and compare the two models.

2.3 Dataset & Chandra Instrumentation

In this work, we utilize *Chandra*'s HETG. As mentioned in Chapter 1, the extended nature of the Sgr A* image poses challenges for effectively and precisely isolating photons originating from the accretion flow amidst nearby contaminating objects or background sources. The extraction pipeline may therefore inadvertently capture contaminating photons that do not

stem from the accretion flow.

The HEG +1 and HEG -1 orders (opposite sides of the 'X') exhibit several distinctions. Photons with energies $\sim$ Fe Kα dispersed in the $m = -1$ direction primarily land on ACIS chip S1 (back-illuminated), while those in the $m = +1$ direction land on chips S4/S5 (front-illuminated). This results in differences in effective area and line response functions for both orders. While these effects are minimal for bright sources, they become more pronounced in low-count scenarios, necessitating separate analysis and fitting of the HEG +1 and HEG -1 order data in our work.

The dataset used in this work was carefully extracted (Corrales et al., 2020) from the 3 Ms *Chandra* X-ray Visionary Program (PIs: Markoff, Nowak & Baganoff); in this paper we fit this high-resolution spectrum of Sgr A* in quiescence with a RIAF model. Corrales et al. (2020) removed background and Sgr A* flares, resulting in 2.55 Ms total exposure. Observations were stacked by roll angle, and background spectra were generated by selecting regions "up" or "down" opposite to contaminating sources PWN G359.95-0.04 and IRS 13E along the cross-dispersion direction. The extracted source and background spectra encompass regions from $0''$ - $1.5''$, and $1.5''$ - $5''$, respectively. In the left panel of Figure 2.1, we highlight the effective image regions probed by the HEG. Source and background regions are shown in yellow and blue, respectively. The width of the boxes are determined by the finite energy extraction width used in order sorting (via the `ciao` tool `tg_resolve_events`, more details in Section 2.4.1.1). The raw combined background-subtracted spectrum, depicted in the right panel of Fig 2.1, exhibits strong emission Fe Kα emission from FeXX$-$XXVI features from the inner region of the accretion flow. The HEG spectrum is overplotted with the $s \sim 1$ RIAF from W13 in red, which best fits the zeroth order, low-resolution spectrum. In this analysis, we focus specifically on the Fe Kα complex, the most prominent X-ray emission feature from Sgr A*, and limit the analysis to 6.4 keV $-$ 7.2 keV.

2.4 Methods

2.4.1 RIAF plasma model for the accretion flow

To construct our model, we use the parametric RIAF interpretation (Quataert, 2002; Yuan et al., 2003; Yuan & Narayan, 2014), where the electron temperature and density profiles

are given as follows:

$$T(r) = T_0 \left(\frac{r}{r_0}\right)^{-q}$$
$$n_e(r) = n_{e,0} \left(\frac{r}{r_0}\right)^{-3/2+s} \tag{2.1}$$

We fix T_0 and $n_{e,0}$ to the temperature and density conditions reported in Baganoff et al. (2003), and fix $M_{\rm SMBH} = 4.15 \times 10^6 M_\odot$ (GRAVITY Collaboration et al., 2019). The RIAF parameter s describes the balance between outflow and inflow, with $s = 0$ corresponding to classical Bondi accretion and $s = 1$ indicating an inflow equally balanced by an outflow (Begelman, 2012), while q represents the steepness of the temperature profile. To calculate the expected emission arising from a RIAF, we approximate the accretion flow with shells of plasma assumed to be optically thin and in collisional ionization equilibrium (CIE). We use the publicly available `pyAtomDB`[2] version 0.10.13 code with AtomDB version 3.0.9 to model the photon emissivity in each spherical shell. The plasma is assumed to be optically thin and spherically symmetric, such that the total spectrum is obtained by numerically integrating the luminosity function over a series of nested shells with differential volume element dV. We calculate the luminosity at each radius using `pyatomdb` for a given RIAF s, q, and Z.

The python module `pyAtomDB` can be used to calculate emission for plasmas up to $kT \approx 86$ keV, or $T \approx 10^9$ K. Above this temperature ceiling, astrophysical plasmas are expected to be fully ionized, producing a smooth continuum with no atomic features. For plasma shells where the temperature exceeds $kT > 86$ keV, we calculate the relativistic bremsstrahlung continuum using the pyAtomDB functions `do_brems` and `calc_ee_brems`, which calculate the ion-electron and electron-electron bremsstrahlung emissivity, respectively. Around 86 keV, the inclusion of electron-electron bremsstrahlung adds about 20% to the continuum emission. The point at which the accretion flow plasma reaches these temperatures depends on the slope of the RIAF temperature profile. For $q \sim 2$ and $q \sim 1$, the plasma becomes fully ionized for radii $R < 10^5 R_g$ and $R < 10^4 R_g$, respectively.

In reality, the accretion flow is not spherically symmetric. In a companion paper, Balakrishnan et al. 2024b, we compare our RIAF model to simulations of the WR stellar winds surrounding Sgr A*. The two models offer different physical insights; the simulations take into account velocity broadening of the colliding winds and asymmetries in the plasma, while the spherically symmetric RIAF model incorporates an inflow/outflow balance but does not include velocity structure. We do not include thermal broadening in our RIAF model since its impact is negligible; thermal broadening in a $10^7 K$ plasma is $\sim 4 - 10$ eV and HEG

[2]https://github.com/atomdb/pyatomdb

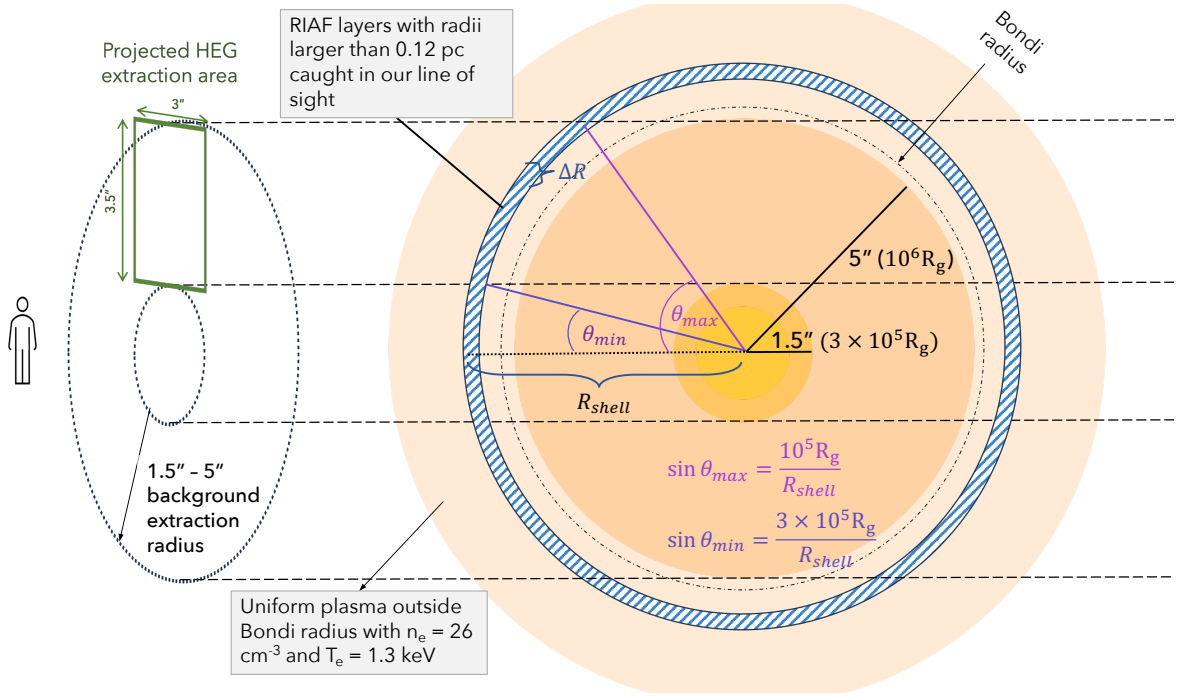


Figure 2.2: Diagram illustrating the geometry taken into account when calculating the RIAF model flux for the background region. We include the projected HEG extraction area; this reflects how the spectral extraction pipeline for HEG captures photon events between 1.5″ and 5″ in the cross-dispersion direction and up to 3″ along the dispersion axis. In other words, the source spectrum probes the central $3 \times 10^5 R_g$ while the background annulus spans $3 - 10 \times 10^5 R_g$. Only a portion of shells outside of $10^6 R_g$ lie within our line-of-sight projection in the background extraction region (green box). We use θ_{min} and θ_{max} to denote the angular boundaries between which a given shell is captured. These quantities are used to calculate the differential volume in each shell, as seen in Equations 2.3 and 2.4.

resolution is $\sim 70 - 140$ eV. Adding thermal broadening has no discernable effect on the predicted counts histogram.

2.4.1.1 Accounting for the HETG geometry

The source and background spectra used in this work probe regions of the accretion flow corresponding to $0 - 1.5''$ ($< 3 \times 10^5 R_g$, or < 0.06 pc) and $1.5 - 5''$ ($3 - 10 \times 10^5 R_g$, or $0.06 - 0.19$ pc) in radius away from Sgr A* respectively. To account for layers outside the physical boundaries of the accretion flow that are not completely encompassed by the extraction region but contribute to the plasma emission along the line-of-sight, we integrate the luminosity function along a cylinder, as demonstrated in Figure 2.2. We calculate the

radial-dependence of the luminosity function, for every shell, as follows:

$$\begin{aligned}\frac{dL}{dR} &= n^2\Lambda(n_e, T_e, Z)\ \frac{dV}{dR} \\ &= n^2\Lambda(n_e, T_e, Z)\ 2R^2\ sin\theta\ d\phi d\theta \\ &= n^2\Lambda(n_e, T_e, Z)\ 2R^2 \times 2\pi\ \ [cos(\theta_{min}) - cos(\theta_{max})] \\ &= n^2\Lambda(n_e, T_e, Z)\ 4\pi R^2\,(\cos\theta_{min} - \cos\theta_{max})\end{aligned} \tag{2.2}$$

where $\Lambda(n_e, T_e, Z)$ comes from `pyatomdb`, and the differential volume in each shell (dV) takes into account our geometric setup, shown schematically in Figure 2.2. Each shell outside the radius of interest ($1.5''$ for the source regions and $5''$ for the background regions) is multiplied by a geometric factor which takes into consideration the portions of the shell falling within the angular boundaries defined by θ_{min} and θ_{max}. The absolute limits of θ are $[0, \pi/2]$, and a factor of 2 is introduced into the calculation to account for the emission from both the front and back side of the optically thin accretion flow.

Another factor to consider is that the HETG order-sorting pipeline only retains events within $3''$ along the dispersion axis (CPOG Section 8.2), marked by the green box in Figure 2.2. For the background model, we include a factor of $f_B = 0.15$, which expresses the ratio of the area captured by the HETG to the area of the $1.5''-5''$ background extraction annulus. Plugging in the appropriate values for θ_{min} and θ_{max} for the various cases, we obtain:

$$\left(\frac{dV_{shell}}{dR}\right)_{src} = 4\pi R^2 \times \begin{cases} 1 & R < 3\times 10^5 R_g \\ (1-\cos\theta_{max}) & 3\times 10^5 R_g < R < 10^6 R_g \end{cases} \tag{2.3}$$

for the plasma inside the source extraction region, and

$$\left(\frac{dV_{shell}}{dR}\right)_{bkg} = 4\pi R^2 f_B \times \begin{cases} 1 & 3\times 10^5 R_g < R < 10^6 R_g \\ (\cos\theta_{min} - \cos\theta_{max}) & 10^6 R_g < R < 2.4\times 10^6 R_g \end{cases} \tag{2.4}$$

for plasma inside the background extraction region. All notation is consistent with that defined in Figure 2.2. For both the background and source regions, we integrate out to a maximum radius of $2.4\times 10^6 R_g$, to ensure appropriate comparison to the simulations in the next chapter. We then integrate dL/dR over all shells to get the expected flux arising for a

given RIAF with three free parameters: s, q, Z_{Fe}. We treat any material outside the Bondi radius ($1.1 \times 10^6 R_g \approx 5.5''$) as a uniform plasma with temperature and density 1.3 keV and 26 cm^{-3} (Baganoff et al., 2003).

2.4.1.2 Choosing RIAF Model Hyperparameters

Several model parameters demanded careful consideration: the metallicity of the plasma, Z, the Bondi radius, R_{Bondi}, the number of radial bins used in the integration, N_R, the innermost radius of integration, R_{in}, and the outer bound on the radius, R_{out}.

Utilizing `pyatomdb` grants us significant control over the plasma element abundances. To develop initial estimates of the abundance, we extracted a CCD spectrum from the zeroth-order HETG-S image, following spatial regions used in W13. We used the XSPEC `tbvarabs` interstellar absorption model (Wilms et al., 2000) and incorporated the extinction effect of dust scattering removing light from the source extraction aperture assuming the Rayleigh-Gans approximation, i.e., $\tau_{sca} = 0.5(\mathrm{N_H}/10^{22}\ \mathrm{cm}^{-2})(E/\mathrm{keV})^{-2}$, which is valid for $E > 2$ keV (Predehl & Schmitt, 1995; Nowak et al., 2012; Corrales et al., 2016). The prevalent Iron line at 6.7 keV provides the strongest constraint on the plasma models, and it is poorly fit with standard solar abundances. We obtain a reasonable fit (a reduced Cash statistic of 1.06) with a `vapec` model where all metal abundances are set to 2 $Z_\odot$ (consistent with metallicity measurements from stars in the GC; Do et al., 2018) and we allow the Iron abundance to vary. While Do et al. (2018) measured metallicity in late-type giants, the abundance, and particularly the Iron abundance, in the Wolf-Rayet winds feeding the black hole could be different. The `vapec` model best fit gives $\mathrm{N_H} = 9.2^{+0.5}_{-1.1} \times 10^{22}$ cm^{-2}, $kT = 3.4^{+0.7}_{-0.3}$ keV, and $Z(\mathrm{Fe}) = 1.1 \pm 0.2\ Z_\odot$. This relative under-abundance of Iron is consistent with previous results arguing for Iron depletion in the GC ISM (Ponti et al., 2016). Therefore, in our RIAF model procedure, we fix the general plasma abundance to 2 $Z_\odot$(with the catalog from GA89; Grevesse & Anders, 1989) and only allow the Iron abundance, Z_{Fe}, to vary. When calculating the predicted HEG spectrum, we note that the resulting 6.4 keV$-$7.2 keV spectra calculated with 4 $Z_\odot$ vs. 2 $Z_\odot$ only differ by 0.1%.

The canonical Bondi radius for a spherical, non-rotating cloud of gas is determined by the sound speed, $R_{Bondi} = \frac{GM_*}{c_s^2}$, where the sound speed of the plasma is dependent on the metallicity in the form of the mean molecular weight, μ. When incorporating the galactic potential, the Bondi radius has been estimated to be 0.07 pc, or $3.5 \times 10^5 R_g$ (Quataert, 2002), while incorporating the rotation of the plasma yields a wider range of values (Yuan & Narayan, 2014). R_{Bondi} is important in our model because it is the scale factor by which we determined the electron density and temperature at a given radius (see Equation 2.1). The canonical values we are using for n_0 and T_0 (26 cm^{-3} and 1.3 keV, respectively) come

from Baganoff et al. (2003), which assumes a Bondi radius of $1'' - 2''$ and metallicity of 2 $Z_\odot$. With $Z \sim 2\ Z_\odot$ and an updated mass for Sgr A*, the Bondi radius is $R_{Bondi} = 1.1 \times 10^6 R_g$, corresponding to $5.5''$. We note that for a given RIAF $s, q,$ and Z_{Fe}, changing the value of R_{Bondi} to $4''$ has no discernable effect on the predicted spectrum.

We find that our RIAF emission model is insensitive to the number of radial bins used, NR. We choose to use 150 log-spaced bins from $10^3 - 2.4 \times 10^6 R_g$ over which to calculate the plasma model.

We chose an inner radius of $R_{in} = 1000\ R_g$ because we cannot resolve the inner regions ($1000\ R_g \sim 5 \times 10^{-3}''$, while the HETGS angular scale is $0.5731''$). Setting an inner boundary allows us to ignore effects from synchrotron and inverse Compton scattering that arise in the inner regions of the black hole. Close to the black hole's event horizon, magnetic effects start to dominate; many magneto-hydrodynamic simulations of Sgr A* choose 100 R_g as their outer boundary (e.g. Dexter et al., 2020; Ressler et al., 2020a,b). Outside of $\sim 10^2 - 10^3 R_g$, the electron temperature is too low for significant synchrotron emission (Yuan et al., 2003) and significant Comptonization of electrons (Melia, 1992). In addition, as we are focusing on a small energy range, any synchrotron or Comptonization effects would add to the continuum and manifest as a powerlaw, which we are already introducing in our fitting procedure (Section 2.4.2). We note that changing the inner radius from $R_{in} = 1000 R_g$ to $R_{in} = 10^4 R_g$ changes the spectrum by less than 5%.

Finally, we consider the outer boundary for the integral described in Section 2.4.1.1. The outer limit of the cylindrical projection is important as it determines the contribution from cooler RIAF layers in the model. To maintain consistency with the stellar wind simulations we use in Chapter 3, we chose a fixed R_{out} corresponding to $12''$, or $2.4 \times 10^6 R_g$.

2.4.2 Modeling the HEG Spectrum

The RIAF emission must be processed to mimic observation through the HEG. In order to directly compare these models to the extracted HEG spectrum, it is necessary to include effects of interstellar extinction and contaminating background, before calculating the predicted photon counts via folding through the detector response function.

As mentioned in Section 1.1.2, *Chandra* HETG is a slitless spectrograph. The background stems from both physical plasma and non-physical zeroth order (non-dispersed) image photons, impacting the spectrum. Given our focus on a narrow energy range (6.4 - 7.2 keV), we utilize a power law model to characterize these contaminating photons.

$$PL = N_{PL} \left(\frac{E}{6.7 \text{ keV}} \right)^{-\gamma} \tag{2.5}$$

and fit for N_{PL} and γ, where N_{PL} represents the photon flux at 6.7 keV, and γ determines the slope of the added powerlaw.

We modeled the effect of interstellar extinction with the Verner & Yakovlev (1995) absorption cross-sections for gas-phase elements, following the ISM abundance table of Wilms et al. (2000), and the dust extinction cross-sections from the `ISMdust` model (Corrales et al., 2016). We fix the GC column density to $N_H = 10^{23}$ cm^{-2} (Baganoff et al., 2003). The high column density leads to significant extinction; at 6.7 keV, we lose 23.2 % of the photons to gas and dust (8% to gas absorption, 15.3 % to dust scattering) along the line-of-sight.

In summary, our final flux model can be described as:

$$\begin{aligned} F^{\rm src}_{HEG} &= F^{\rm src}_{\rm RIAF}(s, q, Z_{Fe})\ e^{-\tau} + PL(N_{PL}, \gamma) \\ F^{\rm bkg}_{HEG} &= F^{\rm bkg}_{\rm RIAF}(s, q, Z_{Fe})\ e^{-\tau} + f_{\rm BACKSCAL}\ PL(N_{PL}, \gamma) \end{aligned} \tag{2.6}$$

where $F_{\rm RIAF}$ is the RIAF model computed from Equation 2.2, integrated over R and divided by $4\pi d^2_{\text{Sgr A}*}$, and $f_{\rm BACKSCAL}$ conveys the scale factor between the background and source extraction region sizes, stored in the 'BACKSCAL' data header keyword. We use the publicly available Python package `pyxsis`[3] to convolve this model flux with the instrumental response. Applying the HEG response function accounts for the energy-dependent effective area and line spread functions of the detector.

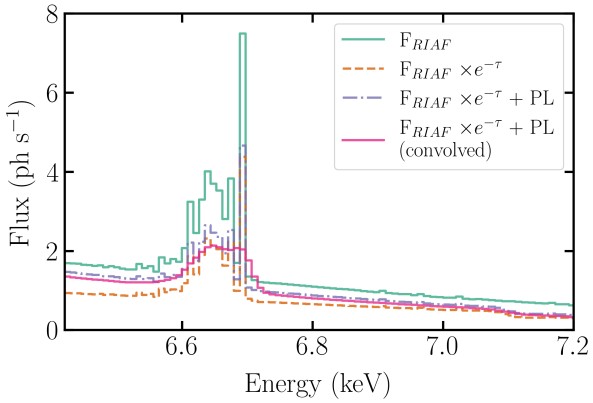


Figure 2.3: Demonstration of the procedure used to predict the HEG +1 source region counts histogram for a given RIAF model. The green curve shows the RIAF emission (in ph s^{-1}) calculated with `pyatomdb`, integrated over the differential volume corresponding to the physical region probed. We incorporate extinction (orange dashed) and a powerlaw for contaminating photons (blue dot-dashed). Convolving with the HEG ancillary response file (ARF) and response matrix file (RMF) leads to the final counts histogram (pink), washing out the fine structure from the original line profiles.

[3]https://github.com/eblur/pyxsis

In Figure 2.3, we demonstrate how each step in our processing affects the model spectrum for the HEG +1 source region. We begin by calculating the RIAF emission (green line) for a given $s, q,$ and Z_{Fe}, calculated with the HEG +1 energy bins and integrated over the effective physical region contributing the spectrum (Figure 2.2). Subsequently, we incorporate extinction (orange dashed line) and a powerlaw for contaminating photons (purple dot-dashed line). Lastly, we apply the instrumental response files to generate the predicted counts histogram (pink). It is clear that the instrumental line spread function washes out much of the fine line structure between 6.6 and 6.7 keV.

2.4.3 Fitting

We fit the data between 6.4 keV and 7.2 keV using the Python package `emcee`, which implements Markov chain Monte Carlo (MCMC) sampling with the Metropolis-Hastings algorithm (Foreman-Mackey et al., 2013). We fit the unbinned background and source region spectra from the HEG +1 and -1 orders simultaneously. In the RIAF models, we fit for s (slope of the electron density distribution), q (slope of the temperature distribution), Z_{Fe} (Iron abundance in units of $Z_\odot$), N_{PL} (normalization of the background powerlaw), and γ (powerlaw index). The powerlaw component, representing the background, is allowed to be different for the +1 and -1 HEG orders. This gives us in total 7 free model parameters: the s, q, and $Z_{\rm Fe}$ values, which are the same across both +1 and -1 orders, and four background parameters, N_{PL} and γ for each +1 and -1 order. Due to the small number of counts in each histogram bin, we need to utilize Poissonian statistics. We therefore use the Cash statistic to describe the model likelihood,

$$C = 2\Sigma_i \left(m_i - x_i \ln m_i\right) \tag{2.7}$$

where m_i denotes the given model and x_i refers to the data, and i represents each energy bin in the counts histogram. To maximize the likelihood, we minimize the sum of four Cash statistics corresponding to a specified set of model parameters, aggregating C values across both source and background regions for both spectral orders.

The walkers were guided using the priors detailed in Table 2.1. The MCMC was run until the auto-correlation time τ_f, indicating the number of steps required for the chain to achieve a state independent of its previous state, changed by less than 10%. We ran the MCMC sampler with 40 walkers for a total of 1600 steps. We excluded the initial 100 steps, after visually inspecting the walkers' exploration of the parameter space, as part of the burn-in phase. This left us with a total of about $57,000$ samples in the posterior distribution. Table 1 gives the best fit values for each of the seven free model parameters and their corresponding

Parameter	Priors		Fit Results	
	Gaussian $(\bar{x}, \sigma)$	Limits	Best	(90% C.I.)
s	-	$[0, 5)$	0.74	$(0.62, 1.40)$
q	-	$(0, 5)$	0.22	$(0.005, 1.56)$
Z_{Fe}	(1,2)	(0.001, 10)	0.13	$(0.03, 0.32)$
$\log N_{PL,+1}$	(-6, 3)	(-12,-3)	-7.81	$(-9.96, -7.53)$
$\log N_{PL,-1}$	(-6, 3)	(-12,-3)	-7.29	$(-7.52, -7.21)$
$\gamma_{PL,+1}$	-	$(-20, 20)$	10.54	$(-6.26, 20)$
γ_{PL}	-	$(-20, 20)$	3.91	$(-0.53, 11.30)$

Table 2.1: Summary of priors and fit results from our MCMC sampling. The Iron abundance, Z_{Fe} is given in units of $Z_\odot$. Z_{Fe} and the normalization on the powerlaw, N_{PL}, are given gaussian priors in additional to hard limits. For each parameter, we list the best-fit value and the 90% credible intervals.

90% credible intervals.

2.5 Results

2.5.1 HETG Spectral Fitting

In Figure 2.4, we show the best-fit models determined through our fitting procedure in blue, corresponding to $s = 0.74\ (-0.22, +0.66)$, $q = 0.22\ (-0.22, +1.35)$, and $Z_{Fe} = 0.13 Z_\odot\ (-0.10, +0.19)$. The best-fit values and 90% credible intervals for all the model parameters are listed in Table 2.1. For visual clarity, the spectra are binned by a factor of 4, and accompanying each spectrum are residual counts, $(x_i - m_i)$. While the RIAF model effectively captures the structure in the HEG +1 source region, it predicts a narrower 6.7 keV feature compared to observations from the HEG -1. Additionally, apparent features in the background spectrum around 6.5 and 7 keV are not accounted for by the RIAF model. The HEG -1 falls on a back-illuminated chip, which has a higher background level, likely explaining the large variance in the HEG -1 order data. In background regions, the best-fit RIAF model predicts a weak 6.7 keV line that is not observed in the data; here, the power law dominates, providing roughly 95% of the flux, indicating that most of these photons do not originate from the accretion flow. Due to degeneracies in the best-fit parameter space, predicted counts histograms were constructed using combinations of s, q, and Z_{Fe} from walkers with the top 5% of likelihood values. These are used to draw the model contours on top of the best-fitting RIAF models, and it is clear that different combinations of RIAF parameters are difficult to distinguish given the signal in the data. The number of counts in

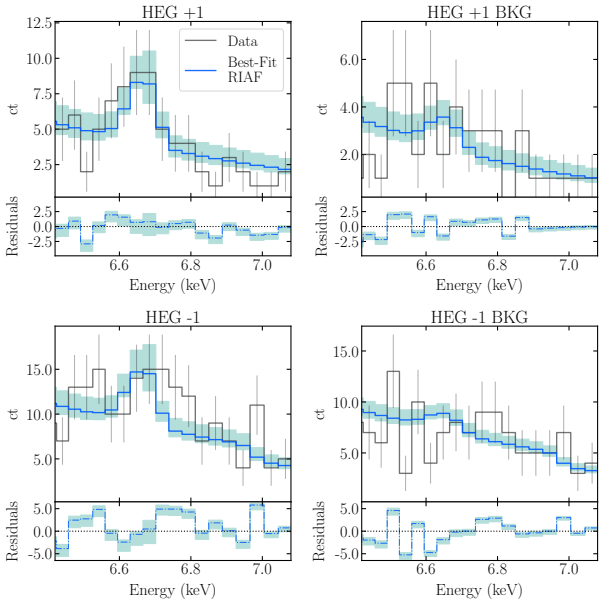


Figure 2.4: Final fits to the HEG +1 and -1 source and background regions, with error contours corresponding to RIAFs with parameters from chains within the top 5% likelihood range. The data and best-fit RIAF are plotted in black and blue, respectively, and are binned to have 4 cts/bin for visual clarity. The residual counts ($x_i - m_i$) are plotted in dashed blue lines (note the limits on the y-axis are different for the HEG +1 and HEG -1 residuals). The model captures some of the 6.7 keV emission but does not capture any structure in the background.

each bin are too small to make comments on the statistical significance of the residuals in this spectrum.

Figure 2.5 shows the posterior distribution obtained for s, q, and Z_{Fe}. Among these parameters, we observe that the slope of the temperature profile, q, and slope of the density profile, s, are degenerate. However, the distributions for each parameter are quite well-defined and constrained. The best fit suggests that $s = 0.74$, indicating an inflow slightly stronger than an outflow in this region. While this aligns with the findings of W13, the best-fit temperature profile has $q = 0.22$, indicating a much shallower profile than the assumed $q \sim 1$ in W13. According to conservation of energy arguments within a gravitational potential where $U = \frac{1}{r}$, the temperature profile should theoretically show a linear decrease with radius (Quataert, 2002). Such a flat temperature profile has been commonly assumed in ADAF models (Begelman, 2012; Yuan & Narayan, 2014). In contrast, our RIAF model predicts a less steep dependence on temperature. The data demonstrably prefer low values of Z_{Fe}, indicating a subsolar Iron abundance that is broadly consistent with the results of the APEC fits (Section 2.4.1.2) and Ponti et al. (2016).

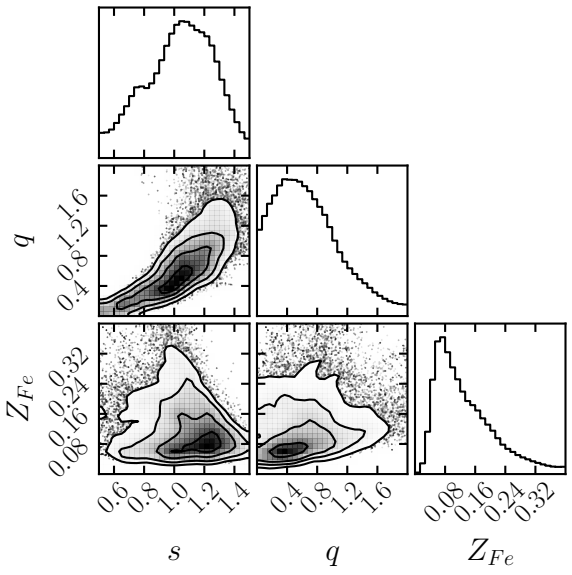


Figure 2.5: LEFT: Corner plot from the final fits of our RIAF model with `pyatomdb`, showing the distributions for RIAF s (material density slope), q (temperature profile slope), and Z_{Fe} (relative to solar; all other elemental abundances were set to 2 $Z_\odot$). Overall, the data prefer sub-solar Iron abundances, s values close to 1, and $q \approx 0.22$.

2.6 Summary & Conclusions

As the closest SMBH, low-luminosity Sgr A* offers unique opportunities to study inefficient accretion flows. The quiescent high-resolution *Chandra* X-ray Visionary Program (PIs: Markoff, Nowak, & Baganoff)[4] spectrum of Sgr A* contains line structure that could hint at potential temperature structure, but could also be an artifact of extraction techniques and noise (Corrales et al., 2020). To better understand this spectrum, we develop a model for emission via the RIAF prescription (e.g. Yuan & Narayan, 2014), accounting for the specific geometry and extraction procedures of the *Chandra* HETG-S instrument. RIAFs are characterized by power-law density ($n \propto r^{-3/2+s}$) and temperature ($T \propto r^{-q}$) profiles, with $s = 0$ and $s = 1$ corresponding to classical Bondi accretion, where mass is conserved in the accretion inflow, and a balanced inflow and outflow, respectively.

We calculate the RIAF emission under the assumption of collisional ionization equilibrium within nested spherical shells. The `pyAtomDB` code is employed for photon emissivity modeling in each shell, considering optically thin, spherically symmetric plasma in the region that is physically probed by various HETG-S extraction regions. We choose a general metal abundance of 2 $Z_\odot$ to model the plasma (Do et al., 2018), but allow the Iron abundance, Z_{Fe}, to vary. We note that our RIAF model depends on certain hyperparameters which

[4]https://www.sgra-star.com/

change the resulting counts histogram by less than 10%, a difference that cannot be resolved with the current dataset.

We simultaneously fit HEG +1 and HEG -1 source and background regions with our RIAF emission model. Our model is unable to capture any line features other than the 6.7 keV He-like Iron lines, implying that a majority of the line structure arises due to a high X-ray background in the region and statistical noise. The elevated X-ray background indicates that the photons we detect outside of 1.5″ may not come from the Sgr A* accretion flow but rather from numerous unresolved point sources within this region (Muno et al., 2003).

When allowing both s and q to vary, we find a best fit of $s = 0.74^{+0.66}_{-0.12}$, indicating an inflow and outflow balance consistent with both previous fits to the non-dispersed *Chandra* X-ray spectrum (W13) and multiwavelength models with boundary conditions fixed to the accretion rate at the Bondi radius ($s \approx 0.6$ Ma et al., 2019). The posterior distribution we obtained for q suggests a shallower temperature profile than that typically assumed by ADAF models (Quataert, 2002; Yuan et al., 2003; Begelman, 2012). Our best fit is $q = 0.22^{+1.35}_{-0.22}$. The data also require a low Iron abundance, $Z_{Fe} < 0.32 Z_{\odot}$. Considering measurements of stars in the GC ($Z \sim 2\ Z_{\odot}$; Do et al., 2018), this argues for Iron depletion in the GC, and is consistent with Ponti et al. (2016). The slopes of the density and temperature profiles are degenerate with each other. In Chapter 3, we compare the RIAF model to predictions of the shocked plasma arising from colliding winds in the central parsec (Cuadra et al., 2015; Russell et al., 2017), and provide microcalorimeter predictions for both these models.

CHAPTER 3

Modeling the High-Resolution Spectrum of Sgr A's accretion flow with Hydrodynamical Simulations of Stellar Winds

The contents of this chapter were published in The Astrophysical Journal, Volume 947, Issue 1, in collaboration with Christopher M. P. Russell, Lia Corrales, Diego Calderón, Jorge Cuadra, Daryl Haggard, Sera Markoff, Joey Neilsen, Michael Nowak, Daniel Q. Wang, and Fred Baganoff in the *Astrophysical Journal* volume 974, issue 1, and can be found in full at this link.

3.1 Abstract

Hydrodynamic simulations of the stellar winds from Wolf-Rayet stars within the Galactic Center can provide predictions for the X-ray spectrum of supermassive black hole Sgr A*. Herein, we present results from updated smooth particle hydrodynamics simulations, building on the architecture of Cuadra et al. (2015); Russell et al. (2017), finding that a "cold" (10^4 K) gas disk forms around Sgr A* with a simulation runtime of 3500 years. This result is consistent with previous grid-based simulations, demonstrating that a cold disk can form regardless of numerical method. We examine the plasma scenarios arising from an environment with and without this cold disk, by generating synthetic spectra for comparison to the quiescent Fe Kα Sgr A* spectrum from *Chandra* HETG-S, taken through the *Chandra* X-ray Visionary Program. We find that current and future X-ray missions are unlikely to distinguish between the kinematic signatures in the plasma in these two scenarios. Nonetheless, the stellar wind plasma model presents a good fit to the dispersed *Chandra* spectra within 1.5″ of Sgr A*. We compare our results to the Radiatively Inefficient Accretion Flow (RIAF) model fit to the HETG-S spectrum presented in Chapter 2 and find that the Bayesian model evidence does not strongly favor either model. With 9″ angular resolution and high

spectral resolution of the X-IFU, *NewAthena* will offer a clearer differentiation between the RIAF plasma model and hydrodynamic simulations, but only a future X-ray mission with arcsecond resolution will significantly advance our understanding of Sgr A*'s accretion flow in X-rays.

3.2 Introduction

Sagittarius A* (Sgr A*), the supermassive black hole in the center of the Milky Way, is immersed in a complex, multi-phase gaseous medium, and surrounded by a parsec-scale nuclear star cluster (see Genzel et al., 2010, for a review). While most of the cluster is comprised of old stars (Nogueras-Lara et al., 2020), there is also a young population, including some 30 Wolf-Rayet (WR) stars with orbits that extend as close as ≈ 0.05 pc from Sgr A*(Paumard et al., 2006; Lu et al., 2013). WR stars are evolved, massive stars, characterised by powerful stellar winds that have mass-loss rates $\dot{M} \sim 10^{-5} M_{\odot}\,\mathrm{yr}^{-1}$ and terminal speeds $v \approx 500 - 2500\,\mathrm{km\ s}^{-1}$ (Martins et al., 2007). The relatively small separation between the WR stars means that their stellar winds collide in relatively high-density shocks, producing plasma that reaches 10^7 K, emits in X-ray (Baganoff et al., 2003; Quataert, 2004; Wang et al., 2013), and is accreted onto the supermassive black hole (Cuadra et al., 2005).

The number of relevant wind sources and their non-trivial orbital distribution (von Fellenberg et al., 2018; Jia et al., 2023), makes this region hard to model analytically, in particular if we want to obtain the amount of gas available for accretion onto Sgr A*. Several studies have therefore relied on hydrodynamic simulations to model the gas dynamics of the material supplied by the WR stars orbiting Sgr A*. The predicted accretion rate arising from hydrodynamic simulations (Cuadra et al., 2015, hereafter C15) at the Bondi radius ($\sim 4 - 5''$, or 0.2 pc; $\dot{M}_{\mathrm{SMBH}} \sim 10^{-6} M_{\odot}\,\mathrm{yr}^{-1}$) is in agreement with theoretical estimates based on X-ray observations at the same scale (Baganoff et al., 2003). Further numerical work has reached deeper into the Galactic center, by first running parsec-scale simulations of the stellar winds (Ressler et al., 2018, 2020a), and then zoom-in magnetohydrodynamic (MHD) and general relativistic magnetohydrodynamic (GRMHD) models of regions progressively closer to Sgr A* (Ressler et al., 2020b). While these simulations do not currently fit observations close to the event horizon (Event Horizon Telescope Collaboration et al., 2022a), they provide a promising framework for understanding how the observed properties of the accretion flow came to be.

The simulations used in C15, Russell et al. (2017, hereafter R17), and Calderón et al. (2020) focus on the WR stars as they have the largest mass-loss rates of any stars in the region (Martins et al., 2007). There is likely some outflow produced by the accretion flow of

Sgr A* itself, predicted by simulations (Ressler et al., 2018; Dexter et al., 2020; Chatterjee et al., 2021) and Radiatively Inefficient Accretion Flow (RIAF) models (e.g., Blandford & Begelman, 1999). RIAFs are parameterized by mass accretion rate, $\dot{m} \propto r^s$, material density, $n \propto r^{-3/2+s}$, and temperature $T \propto r^{-q}$. Here, $s = 0$ corresponds to classical Bondi accretion and $s = 1$ indicates an inflow balanced by an outflow (Begelman, 2012). Observational fits to the multiwavelength spectral energy distribution (SED) of Sgr A* and *Chandra* ACIS spectrum with RIAF models suggest varying s values, with $s \sim 0.05 - 0.3$ closer to the BH (Yuan et al., 2003; Ma et al., 2019) and $s \sim 0.6-1$ at the Bondi radius (Ma et al., 2019; Wang et al., 2013), demonstrating that this outflow is more prominent at higher radii. However, incorporating this outflow into WR simulations has minimal impact on the predicted X-ray spectral shape and only marginally reduces the X-ray flux compared to simulations without Sgr A* feedback (R17). Main sequence OB-star winds, with mass-loss rates three orders of magnitude smaller than the WR stars, may also affect the net mass accretion rate in this region but are found to underpredict the accretion rate at the Bondi radius (Lützgendorf et al., 2016). Therefore, we solely consider mass loss from WR stars for our analysis.

The WR stars alone are able to explain an exceptional amount of the observed behaviour in this region, namely the predicted emission fully explains the X-ray spectrum of Sgr A* (R17). R17 post-processed the simulations of C15 using radiative-transfer tools, producing synthetic X-ray maps and spectra. Analysis of the synthetic observations shows that the overall X-ray flux depends mostly on the mass-loss rates, while the spectral shape is determined by the wind velocities. R17 found that the models closely reproduce the 2-10 keV *Chandra* ACIS spectrum in the $2''-5''$ region. This is rather noteworthy, as the models take as input the stellar wind and orbital properties obtained from infrared observations (Paumard et al., 2006; Martins et al., 2007), and are therefore completely independent of the X-ray data they explain.

The stellar wind simulations predict other observed structures. Depending on the stellar wind collision properties, the plasma can be prone to instabilities and form dusty, gaseous blobs (Fritz et al., 2011; Peißker et al., 2023), which may explain some of the gaseous structure observed in infrared and radio in the same region (Gillessen et al., 2012). Moreover, the stellar winds can perturb some of the larger-scale gaseous streams reaching the central region (Wang et al., 2020) or the circumnuclear disk (Solanki et al., 2023). The mechanisms that enable cold and hot phase plasma structures to co-exist in this way remains a mystery.

There have been claims of detection of a cool ($\sim 10^4$ K) H30α disk co-spatial with the $\sim 10^7$ K accretion flow. Murchikova et al. (2019) measured line shifts at 231.9 GHz with the Atacama Large Millimeter/submillimeter Array (ALMA), finding red- and blue-shifted components approximately 0.004 pc from Sgr A*. The estimated mass of this ionized disk

structure is approximately $10^{-4} - 10^{-5} M_{\odot}$. These results were confirmed in Yusef-Zadeh et al. (2020), who also found these line shifts in H39α, H52α, and H56α emission. However, Ciurlo et al. (2021) obtained observational upper limits for the undetected Brγ disk ($\sim$ 6000 K) that are 80 times lower than the expected emission given the H30α flux. These authors also argue that a maser explanation for this discrepancy, proposed originally by Murchikova et al. (2019), is not consistent with the expected properties of the plasma nor with the putative disc geometry. The results in Ciurlo et al. (2021), however, are consistent with Brγ emission levels predicted by Calderón et al. (2020), who showed that running the simulations for long-enough timescales ($>$ 3000 yr) leads to the accumulation of a $\approx$ 0.01 pc cold gas disk ($\sim 10^4$ K) around Sgr A*. This study utilized `ramses`, which follows an Eulerian approach and incorporates adaptive mesh refinement (AMR) for increased resolution, identifying two distinct mass accretion phases: quasi-steady and disk regimes. The quasi-steady phase, characterized by $\dot{M}_{in} > \dot{M}_{out}$, eventually transitions into the disk phase when a bow shock facilitates rapid cooling, leading to the formation of a cold gas disk. This process results in increased rates of inflow and outflow, eventually reaching a balance where $\dot{M}_{in} \sim \dot{M}_{out}$, indicative of $s \sim 1$ as predicted by RIAF models. We note that this disk is not generated in another series of simulations (Ressler et al., 2018, 2020a), even after extending the simulation run time to 9000 yrs in the past (Ressler et al., 2020a). This discrepancy could be due to differences in the cooling prescriptions; the effect of cooling on the formation of this disk is investigated further in Calderón et al. (2025).

To test whether the cold disk formed in Calderón et al. (2020) is an artifact of the grid-based approach, we extend the SPH simulations of R17 to a longer timescale of 3500 yr. In addition, we test whether we can identify signatures of the cool accretion disk in the particle-based simulations by examining the predicted X-ray emission in both plasma scenarios.

Although the predicted "cold" ($\sim 10^4$ K) disc is not directly observable in X-rays, we wish to investigate whether its kinematics might leave a signature in the hot gas. *Chandra* HETG currently offers the best available spectral resolution combined with sub-arcsecond imaging resolutions, which is required to study the Sgr A* accretion flow. While the low-resolution spectrum from this dataset is reproduced by the stellar winds (R17), we leverage the legacy *Chandra* HETG-S dataset from Corrales et al. (2020) to test whether hydrodynamic simulations of shock-heated WR stellar winds are also able to reproduce the observed X-ray spectrum at the high spectral resolution offered by *Chandra*. The High Energy Transmission Grating Spectrometer (Canizares et al., 2005, HETGS) on *Chandra* disperses a fraction of the incoming photons, providing a high-resolution spectrum with a spectral resolution between 60$-$1000. It consists of two gold gratings, MEG (0.4$-$5 keV sensitive) and HEG (0.8$-$10 keV sensitive, $E/dE \sim 170$ at 6.7 keV). Here we focus on the Fe Kα complex ($\sim$ 6.7

keV) of the Sgr A* accretion flow captured by the HEG (Corrales et al., 2020) to evaluate the possibility that the observed line structure is a direct probe of the velocity structure in the accretion flow.

In Section 3.3, we describe our methodology, with details on the hydrodynamic simulation of the Wolf-Rayet winds followed by how predicted HEG spectra are generated. In Section 3.4, we show our X-ray line profiles and results from fitting these predictions to the HEG data. We compare the stellar wind profiles to the best fits for a RIAF model, presented in Chapter 2, and show micro-calorimeter predictions of these two models. We end this chapter with a summary of our results and conclusions.

3.3 Methods

We once again utilize the high-resolution spectrum used in Chapter 2, originally extracted in Corrales et al. (2020).

Figure 3.1 shows the counts histograms for the source ($0-1.5''$; in solid black) and background ($1.5''-5''$; in dashed blue) regions, for both the HEG +1 and -1 orders. The data are binned to a factor of 3 for visual clarity. Peaks around 6.7 keV are visible in the source regions; numerous other features suggest potential velocity or temperature variations, but might also arise from statistical noise. The velocity resolution of the Chandra HEG is $\Delta v \sim 1500\text{km s}^{-1}$, which is close to the maximum line-of-sight velocities seen in the stellar wind simulations, indicating we may be able to probe the complex velocity structure in the Sgr A* accretion flow with the high resolution spectrum. To examine whether these line features can be explained by a non-homogeneous, multi-temperature plasma with velocity features, we utilize updated simulations from C15 and R17. We calculate the expected X-ray emission generated by stellar winds for each of the source and background regions, and process this thermal emission, accounting for any effects induced by the HETG-S detector. See Chapter 2 for more details regarding corrections made for HETG-S geometry.

3.3.1 Simulation Setup

This work utilizes simulations for the plasma environment of Sgr A* created by WR stars in the central parsec, as developed by C15 and R17. These simulations use the smoothed particle hydrodynamics (SPH) code `GADGET-2` (Springel, 2005) to follow the orbits of the 30 WR stars around Sgr A*, all while ejecting their stellar winds into the simulation domain of a half parsec in radius. The WR stellar mass-loss rates, wind speeds, and spectral types come from Martins et al. (2007), and the stellar orbits are from Paumard et al. (2006).

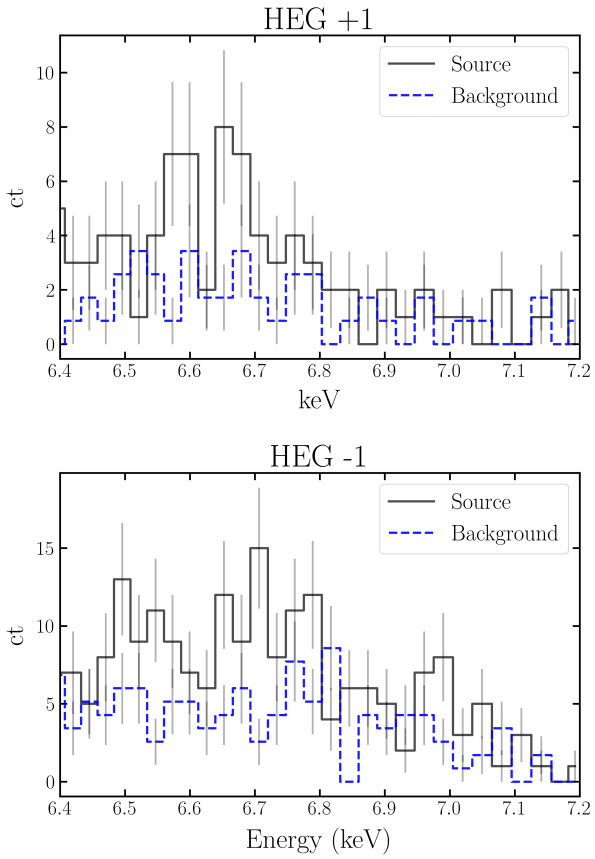


Figure 3.1: The high-resolution quiescent spectrum of Sgr A*, extracted in Corrales et al. (2020), plotted in counts. The top and bottom panels show the data from the HEG +1 and -1 orders, respectively. In this work, we focus on the Fe Kα complex, between 6.4 and 7.2 keV. The spectra extracted from the source (out to 1.5 $''$) and background (between 1.5$''$and 5$''$) regions are plotted in black and blue, respectively, and are rebinned to a factor of 3.

These supersonic winds collide with one another, creating a complex structure of cold, free-streaming winds and hot, post-shock gas that emits thermal X-rays. Material flowing towards the SMBH is removed from the simulation at an inner radius of $r_{\rm min} = 1.2 \times 10^{16}$cm $\approx 10^4 R_g$ (where $R_g = GM_*/c^2$), corresponding to a projected angular distance of $0.02''$ from Sgr A* while material flowing outward is removed at $r_{\rm max} = 1.2 \times 10^{18}$cm $\approx 2.4 \times 10^6 R_g$, corresponding to a projected angular distance of $12''$. In order to reproduce the work of Calderón et al. (2020), which found two different accretion modes onto Sgr A*(quasi-steady and disk mode), we perform two sets of simulations that have different initial starting times. Starting from 3500 yr (as done in Calderón et al., 2020) in the past yields a cold disk around the SMBH, while starting from 1100 yr ago (as done in C15) does not. Additionally, compared to the C15 simulations, the SMBH mass has been updated to $M_{\rm SMBH} = 4.28 \times 10^6 M_\odot$ (Gillessen et al., 2017), and the separation of the WR stars in the IRS 13E cluster has been increased to bring the cluster's X-ray flux into better agreement with the observations (R17; see also Wang et al., 2020). We note that this mass is slightly different to that used in Chapter 2 ($M_{\rm SMBH} = 4.15 \times 10^6 M_\odot$; GRAVITY Collaboration et al., 2019); however, changing the mass in the RIAF model to match Gillessen et al. (2017) changes the counts histogram by less than 4%. These versions of the simulations do not take feedback from the SMBH into account; as shown in R17, this feedback does not change the shape of the X-ray spectrum significantly. The simulations include the same radiative cooling prescription as C15, which uses a $Z = 3Z_\odot$ cooling curve for all winds.

We can predict the HEG spectra from both sets of simulations to see if we can distinguish between the two accretion modes with X-ray spectra. A model spectrum for the thermal X-ray emission is synthesized from the hydrodynamic simulations in a similar fashion as R17, which is built upon a modified version of the visualization program `Splash` (Price, 2007). All mass elements hot enough to emit thermal X-ray emission over $\sim 10^6$ K (indicated by superscript k) are assigned energy-dependent X-ray emissivities, $j_E^k = n_e^k n_i^k \Lambda(E, T^k)$ from the `vvapec` model (Smith et al., 2001) (obtained from `XSPEC`, Arnaud, 1996). The temperature and emission measure of each mass elements' `vvapec` spectrum $\Lambda(E, T^k)$ corresponds to the temperature (T^k) and density (electron number density n_e^k and ion number density n_i^k) of the mass element computed in the hydrodynamic simulation. To distinguish between the various abundances of the winds, the winds and their `vvapec` spectra are split into three categories: WC8-9 stars, WN6-7 stars, and WN8-9 & Ofpe/WN9 stars (following R17). The optical depths through the simulation domain ($\int \kappa_E \rho^k dz$ with z being the line-of-sight integration direction) in the observed X-ray energy range are in the optically thin limit; this calculation made use of X-ray opacities (κ_E) of Verner & Yakovlev (1995) obtained via an abundance-modified version of the `windtabs` model (Leutenegger et al., 2010).

While the density and temperature of the plasma is set by the hydrodynamic simulations, which use a 3 $Z_\odot$ cooling prescription, our predicted Iron line profiles were calculated with abundances of $Z_{Fe} = 0.6-1\ Z_\odot$ (Asplund et al., 2009) depending on the specific WR subtype (see Table 1 of R17 for details). A high metal abundance in the plasma is well-justified; WR stars have low (or non-existent) Hydrogen abundances but high Carbon, Nitrogen, or Oxygen abundances (Sander et al., 2019). Being young stars, WR stars are indicators of recent star formation, so it is reasonable to expect an Iron abundance $\sim Z_\odot$ or higher in the X-ray emitting plasma due to past stellar explosions. However, X-ray studies of WR stars are rare, and there is not yet a generally accepted value. Recent spectral fitting of the 6.7 keV line in the S 308 bubble around a galactic WR system finds a Nitrogen abundance of $\sim 3\ Z_\odot$ and an Iron abundance consistent with $1\ Z_\odot$ (Camilloni et al., 2024). Other studies have used Iron abundances as low of $0.4\ Z_\odot$ (Sander et al., 2019). These abundances are similar to those found from fits to the X-ray emitting plasma around Sgr A*. The RIAF fit from Wang et al. (2013) found an Iron abundance of $Z_{Fe} = 1.23\ Z_\odot$ (Asplund et al., 2009), while in Chapter 2, we found that the spectrum was best-fit an average Iron abundance of $Z_{Fe,\ \text{Paper I}} = 0.18\ Z_\odot$ (relative to Asplund et al., 2009, ; see Section 3.4.2 for further discussion).

We calculate the thermal X-ray intensity from the Sgr A* plasma with the X-ray emissivities above, while incorporating the line-of-sight velocities (v_{LoS}) in each plasma element. The profile function for mass element k is a Gaussian of the form:

$$\phi^k(v_{\text{LoS}}) = \frac{1}{\sqrt{\pi}} \exp\left(\left(v^k_{\text{LoS}} - v_{\text{LoS}}\right)^2 / v^2_{\text{th}}\right) \tag{3.1}$$

where v^k_{LoS} is the element's line-of-sight velocity, v_{LoS} is the particular line of sight velocity being computed, and v_{th} is the thermal/sound speed. `Splash` sums the contribution of each mass element across the $\{x, y\}$ pixel map to obtain thermal X-ray intensity at a particular energy, and we incorporate v_{LoS} as follows:

$$I_E(x,y) = \int j^k_E(x,y)dz = \int n^k_e n^k_i \Lambda(E, T^k)\phi^k(v_{\text{LoS}})dz \tag{3.2}$$

where we integrate z, or line-of-sight direction, from $-2.4 \times 10^6 R_g$ to $2.4 \times 10^6 R_g$ where Sgr A* is situated in the plane of $z = 0$. Computing a single energy's line profile requires looping over the full range of v_{LoS}, which ranges from -3000 to 3000 km s^{-1} in the simulation. The Fe complex has many lines that overlap each other when their v_{LoS} ranges are converted to energy space, so we compute a line profile for each entry in the VVAPEC tables, yielding 150 line profiles at an energy resolution of 6400/dex. All of these overlapping line profiles are then finely interpolated to the same energy grid, where they are summed to yield the

complete $v_{\rm LoS}$-dependent spectrum in the Fe complex. Similarly, in the continuum region, calculations at specific energies blend into adjacent lines due to their proximity, resulting in a composite spectrum. Therefore, we conduct comprehensive line profile calculations across every point within both the continuum and line-complex regions to account for their influence on one another.

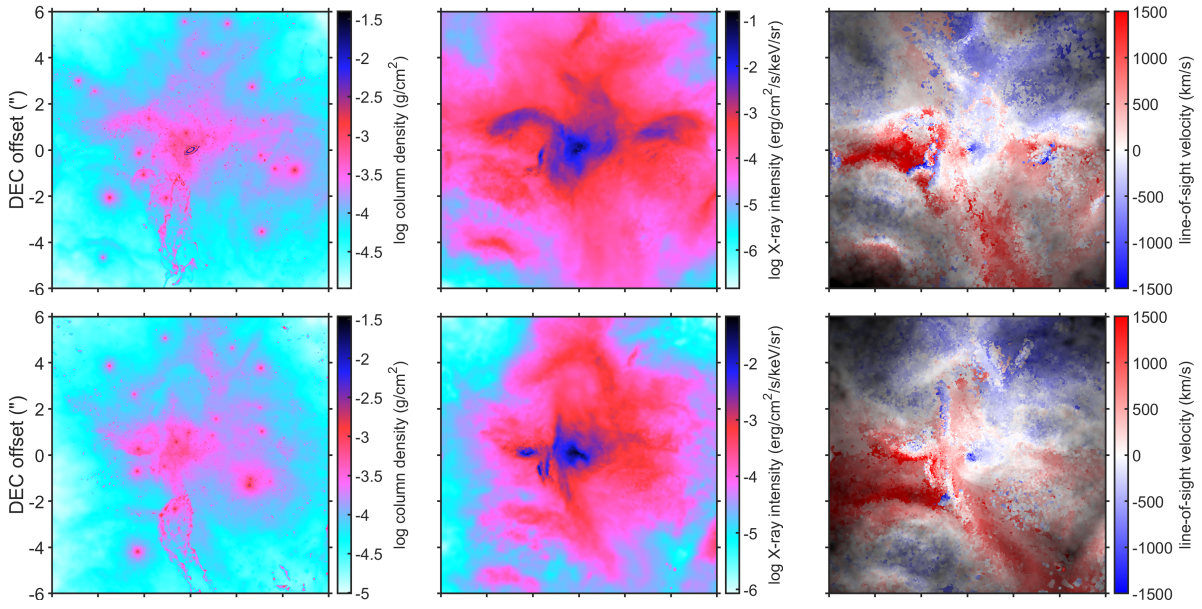


Figure 3.2: The top and bottom rows show the results of the disk (runtime of 3500 yr) and no-disk (runtime of 1100 yr) scenarios, respectively, for gas emitting at 6.7 keV. The plots span the central $12'' \times 12''$ surrounding Sgr A*, with North upwards and East to the left. LEFT: Column density map of the region, with the cool disk of gas seen clearly in the top left panel. MIDDLE: 6.7 keV X-ray intensity with the dark blue highlighting high levels of Fe Kα emission. RIGHT: Illustration of the velocity structure in this complex plasma, with color denoting the line-of-sight velocity corresponding to the line profile's maximum X-ray brightness for each pixel. The grayscale overlay reflects X-ray emission intensity, i.e. dimmer regions indicate X-ray dim gas.

In Figure 3.2, we show the column density, X-ray intensity, and velocity maps corresponding to the disk (top row) and no-disk plasma scenarios (bottom row). Large scale density and X-ray emissivity field differences are at least in part due to the different run times, with the top row showing a snapshot at $t = 3500$ yr and the bottom row reflecting the plasma conditions at $t = 1100$ yr. The disk is visible in the top left plot owing to its high column density. Contributions from slower winds result in high density shocks that cool radiatively, resulting in instabilities that lead to clumpy structure seen in the images. To make the velocity maps, we split the X-ray emission of the same line into 5 km/s bins for each pixel's $v_{\rm LoS}$. Subsequently, we assigned colors to each pixel based on the $v_{\rm LoS}$ corresponding to the

maximum velocity-binned X-ray emission, utilizing a blue-white-red color gradient. Next, to highlight X-ray bright areas and consequently identify X-ray dim regions, we combined this color-coded $v_{\rm LoS}$ image with a grayscale image representing X-ray brightness. This process preserves the X-ray bright sections of the velocity map while enhancing the contrast of the X-ray dim areas. The disk and quasi-steady accretion scenarios lead to different kinematics in the gas that might be resolvable with the high-resolution *Chandra* spectrum.

3.3.2 Modeling the HEG spectrum

To calculate the predicted spectrum from the plasma surrounding Sgr A*, we only include emission from regions physically probed by the HEG (described in Chapter 2). We also incorporate extinction from the interstellar medium (ISM). We calculate the predicted HEG spectrum for the +1 and -1 orders separately instead of combining them due to the differences in the instrumental response matrices, which would be more apparent in this low count regime. The background regions extracted from Corrales et al. (2020) were stacked by roll angle, with the background "up" or "down" regions (in the cross-dispersion direction) opposite from PWN G359.95-0.04 and IRS 13E, chosen to minimize contamination. Since the simulated stellar wind plasma is not radially symmetric, we slice the annular region in half along galactic coordinates; Galactic North refers to regions where $b > 0$ and Galactic South refers to regions where $b < 0$. These two halves roughly correspond to the background regions considered. We use the spectrum calculated solely from the Galactic South as our background model, which ensures that we are capturing the plasma that is opposite in projection from PWN G359.95-0.04 and IRS 13E.

The standard spectral extraction for HETG-S data captures X-ray events within a $1.5''$ radius in the dispersion direction and $3''$ along the dispersion axis[1]. The source region, with a $1.5''$ radius, is fully encompassed within the projected HETG extraction area. However, the background region extends beyond $1.5''$ in the cross-dispersion direction. Accordingly, we introduce a scaling factor to the predicted background spectra denoting the area captured by HETG, which is the ratio of the background extraction region to the Galactic South half-annulus region described above ($f_B = 0.3$).

Following the procedure described in Section 3.2 of Chapter 2, we take into account the slitless nature of the HETGS by implementing a powerlaw background model. We include extinction due to the interstellar medium, employing the ISM abundance table of Wilms et al. (2000) and the dust extinction cross-sections from the `ISMdust` model (Corrales et al., 2016). We use the publicly available Python package `pyxsis`[2] to apply the instrumental

[1] https://cxc.harvard.edu/proposer/POG/html/chap8.html
[2] https://github.com/eblur/pyxsis

response functions and perform a joint fit for the background models of the HEG +1 and HEG -1 spectra from Corrales et al. (2020).

3.4 Results

We calculated line profiles from the two accretion modes (a disk versus a quasi-steady flow) that arise in the stellar wind simulations. We also compare the goodness-of-fit metrics for the stellar wind models with the best fitting radiatively inefficient accretion flow (RIAF) model found in Chapter 2.

3.4.1 Searching For Signatures of a Cold Disk

There is evidence of a cold gas disk around Sgr A* that simulations demonstrate could arise from shocked stellar winds. Observations of H30α emission indicate the presence of a cold disk of gas $\sim 10^4$K that extends about $0.23''(\sim 4.6 \times 10^4 R_g)$ wide and is co-spatial within the hot accretion flow (Murchikova et al., 2019). Interestingly, this observed cooler gas disk rotates counter to the hot plasma, but aligns with the rotation of the Galaxy, the circumnuclear disk, the mini-spiral, and the clockwise stellar disk (Murchikova et al., 2019). We find that a cool disk naturally arises in the stellar wind plasma in both particle-based and grid-based simulations. However, in both cases, the simulated cold gas disk has an angular momentum vector offset by 90° orientation with respect to the observed disk. This misalignment suggests that other interacting structures, such as the minispiral or circumnuclear disk, which have not been incorporated into the simulations, may play a crucial role in its formation. This cold gas disk would not emit in the X-ray, but the presence of the cool disk heightens the accretion rate, resulting in slightly different plasma conditions (see Figure 3.2) which might be resolvable with X-ray spectroscopy. Differences in X-ray line profiles arising due to numerical method (i.e. particle-based vs. grid-based simulations) are investigated further in Calderón et al. (2025).

To test whether we can resolve the differences between a hot plasma with and without a cool gas disk, we calculated the X-ray emission arising from both scenarios and generated predicted *Chandra*-HETG spectra. Figure 3.3 (left) compares the simulated X-ray gas emission arising from a plasma with and without a cold gas disk. The top row pertains to plasma within the source extraction region, ranging from $0''$ to $1.5''$, while the bottom row shows plasma within the Galactic South section of the background annulus, spanning from $1.5''$ to $5''$. Within the plots, the disk and no-disk scenarios are represented by solid and dash-dotted lines, respectively. Unfortunately, the HEG predicted spectra from the two accretion

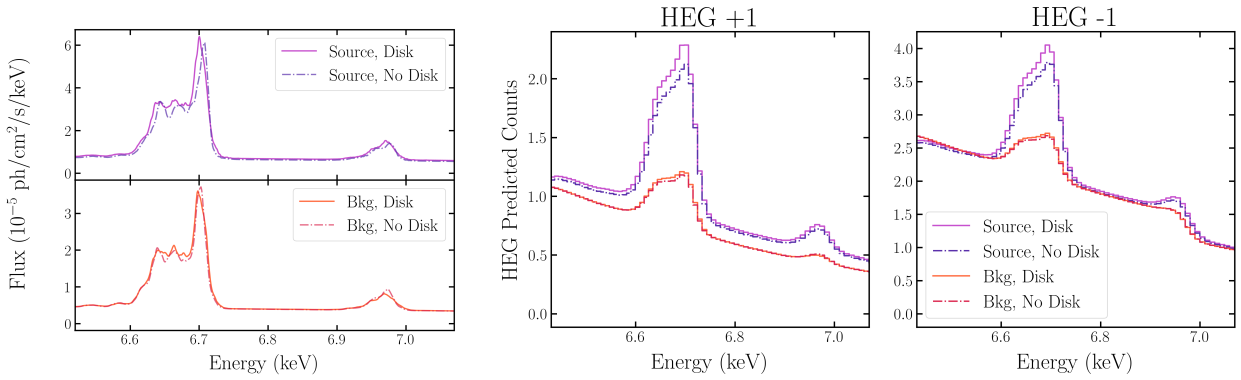


Figure 3.3: LEFT: Line profiles generated by plasma simulated in the 0″- 1.5″source region (top) and 1.5″- 5″background region (bottom). MIDDLE & RIGHT: Predicted counts histograms calculated for HEG +1 (middle) and HEG -1 (right) for the disk (solid curves) and no-disk (dashed curves) plasma scenarios in the stellar winds simulation. We plot the source and background regions in purples and reds, respectively. The small differences between the final spectra with and without a cold gas disk are slight and not resolvable with *Chandra*-HETG, differing only by $\sim 2.6\%$ at the peaks. We are thereby unable to detect evidence of the $\sim 10^4$ K disk from X-ray spectroscopy alone.

modes are almost indistinguishable. The distinction between the disk and quasi-steady flow scenarios is clearest in the Fe Kα emission features, where the peaks are shifted, but not to a degree that can be easily resolved by *Chandra*. The maximum vertical difference between the two spectra is 2.6%. Therefore, our current dataset is not sufficient to differentiate between the different plasma conditions that arise in the disk accretion and quasi-steady flow modes. Given the observational evidence of a cool accretion disk surrounding Sgr A* (Murchikova et al., 2019), we only consider the X-ray line profiles from the disk scenario, moving forward.

3.4.2 Stellar Winds vs. RIAF

In Chapter 2, we used `pyatomdb` to calculate the emission from plasma in Coronal Ionization Equilibrium (CIE) governed by density and temperature profiles according to the Radiatively Inefficient Accretion Flow (RIAF) parametrization (Yuan et al., 2003; Xu et al., 2006; Narayan et al., 2012). The main parameters are the slope of the temperature profile, q, and the steepness of the mass accretion rate and electron density, s. We also fit for the relative abundance of Iron in `pyatomdb`, leading to a total of three free parameters in our RIAF model: s, q, and Z_{Fe}. The predicted HEG spectrum was computed with the same method as the stellar wind emission, accounting for geometry, instrumental effects, and ISM extinction. A significant distinction between the RIAF and stellar wind models is that the former does not take into consideration any potential velocity structure inside the plasma,

including rotation. This has limited impact on our results, as extinction coupled with the HEG instrument response wash out the fine structure (see Chapter 2 for more details). A Monte-Carlo Markov Chain (MCMC) fit to the data yields best-fit and 90% credible intervals of $s = 0.74$ $(-0.12, +0.66)$, $q = 0.22$ $(-0.22, +1.35)$, and $Z_{Fe} = 0.13 Z_{\odot}$ $(-0.10, +0.19)$. The best-fit RIAF s value is roughly consistent with an inflow balanced by an outflow ($s \sim 1$). The data prefer a RIAF model with a low Iron abundance, where $Z < 0.3 Z_{\odot}$.

Similarly, we use the publicly available `emcee` package to perform an MCMC fit for the background model with the static spectral model computed from the hydrodynamic simulations of WR stellar winds. The background contamination comes from different regions of the Galactic Center X-ray image, so the powerlaw parameters are allowed to be different for the +1 and -1 HEG orders, yielding a total of four free parameters. We fit the source and background regions for both orders simultaneously, using Cash statistics. We initiated the model with 20 walkers and applied uniform priors of $-20 < \gamma < 20$ and $-12 < \log N_{PL} < -3$. We ran the MCMC chains until the autocorrelation time, which measures the number of steps required for the chain to achieve a state independent of its previous state, was less than 5%. The resulting best fits and 90% credible intervals for the powerlaw components are: $\log N_{PL,+1} = -7.6$ $(-0.1, +0.1)$, $\gamma_{+1} = 6.7$ $(-6.7, +7.4)$, $\log N_{PL,-1} = -7.2$ $(-0.1, +0.1)$, $\gamma_{-1} = 4.1$ $(-3.8, +3.7)$.

In Figure 3.4, we plot the stellar wind plasma model on top of the best-fitting background model (pink), best-fit RIAF from Chapter 2 (blue), and the observed HEG spectra (black). We have binned the models and data to a factor of 4 for visual clarity, including the residuals. Focusing solely on the model counts histograms, it is intriguing that the simulation of stellar winds and the RIAF model both predict peaks in Iron at 6.7 keV with comparable strengths. The line intensity in the simulations is determined by assuming a plasma abundance of $0.6 - 1$ $Z_{\odot}$ (Asplund et al., 2009) depending on the specific WR subtype, whereas the RIAF fit yielded a lower value of $Z_{\rm Fe} = 0.13 Z_{\odot}$ (Anders & Grevesse, 1989). Converting from Anders & Grevesse (1989) to (Asplund et al., 2009) yields a $Z_{RIAF} = 0.18$ $Z_{\odot}$ and a 90% credible upper limit of 0.45 $Z_{\odot}$.

We investigated whether differences in the temperature and density profiles from both models could explain the lower metallicity predicted by the RIAF model. The WR plasma model predicts elevated plasma temperatures compared to the RIAF temperature profile. At higher temperatures, a higher fraction of the Iron will be in the Fe XXVI state, which reduces the strength of the 6.7 keV line complex. Therefore, the cooler temperatures in the RIAF model are able to produce the same strength 6.7 keV line with less total Iron abundance. One major difference between the RIAF and WR spectral models is that the WR plasma predicts a more significant 6.97 keV feature from Fe XXVI. We are unable to

detect this feature in the HEG spectrum due to the very low effective area at this energy.

Examining the fits to the data, both models capture some of the features in the HEG +1 and -1 source spectra. However, the HEG -1 model spectra recreate neither the broadening in the 6.7 keV line nor the features at 6.5 and 7.0 keV. The background and extra features for the HEG -1 are likely influenced by its placement on a back-illuminated chip, which has a higher background, as opposed to rotation or other broadening effects inherent in the plasma. Both the simulations and the RIAF model anticipate a 6.7 keV feature in the background area that is not very pronounced, suggesting that other sources of photons are likely more dominant $3 - 10 \times 10^6 R_g$ away from Sgr A*. Indeed, the flux from the powerlaw contributes 95% - 98% of the flux in the background spectra.

In all procedures, the Cash statistic was used to evaluate goodness-of-fit in our MCMC sampling. Figure 3.5 shows the distributions of the Cash statistic resulting from fitting the stellar wind plasma (pink) and the RIAF model (blue). While the stellar wind plasma model may appear to offer a better fit, there is considerable overlap in the Cash statistic distributions. To evaluate which model is statistically preferred, we utilize the Bayesian model evidence.

Bayesian inference provides a consistent approach to the estimation of a set of parameters in a model H using Bayes' theorem (Feroz, 2013). For a helpful overview of Bayesian inference in astronomy and variation in notation, see Eadie et al. (2023). Bayes theorem provides the probability distribution of model H parameters, Θ, given the dataset, D:

$$p(\Theta|D, H) = \frac{p(D|\Theta, H)p(\Theta|H)}{p(D|H)}. \tag{3.3}$$

On the left, $p(\Theta|D, H)$, we have the posterior distribution. On the right, $p(D|\Theta, H)$ is the model likelihood $\mathcal{L}(\Theta)$, for which we use the Cash statistic, and $p(\Theta|H)$ is the prior for the model parameters. The denominator, $p(D|H)$, refers to the marginal likelihood or Bayes/model evidence. The Bayes evidence does not depend on the parameters, and is not used in parameter estimation, but is helpful when comparing two models. Selection between competing models H_0 and H_1 can be done by comparing their respective posterior probabilities to compute the model odds (Bayes Factor), $\mathcal{R}$, as follows:

$$\mathcal{R} = \frac{p(H_1|D)}{p(H_0|D)} = \frac{p(D|H_1)}{p(D|H_0)} \frac{p(H_1)}{p(H_0)}$$

where $p(H_1)/p(H_0)$ is the prior probability ratio for the two models. Once the posterior has been determined, the model evidence, $p(D|H)$ can be evaluated numerically by integrating the likelihood over the prior: $p(D|H) = \int L(\Theta)p(\Theta|H)d^n(\Theta)$ over the parameter space.

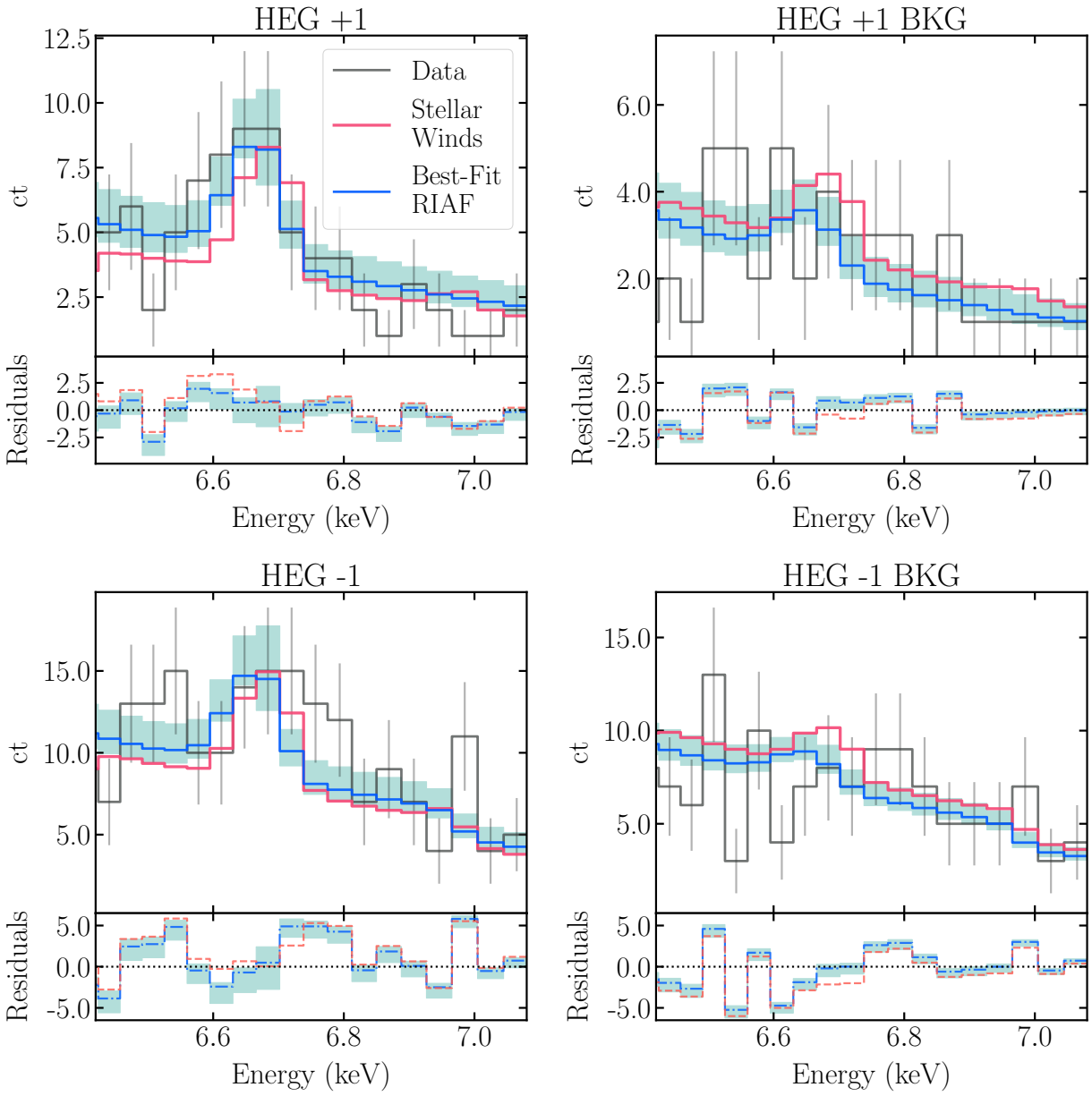


Figure 3.4: Final fits to the HEG +1 and -1 source and background regions. The observation is plotted in black, with the best-fit RIAF model in blue and the stellar wind simulations plotted in pink. The residual counts spectrum (observation − model) are plotted below each subplot. The data is binned to a factor of 4 for visual clarity, however, the fitting was performed on the unbinnned HEG data. While the models capture the 6.7 keV peak in the source spectrum, most of the observed line structure is not predicted in the simulations.

Calculating the Bayes evidence involves an integral that can be numerically challenging; several methods have arisen to address this (Feroz et al., 2009; Handley et al., 2015; Cai et al., 2021). We use the learnt harmonic mean estimator, which uses machine learning techniques

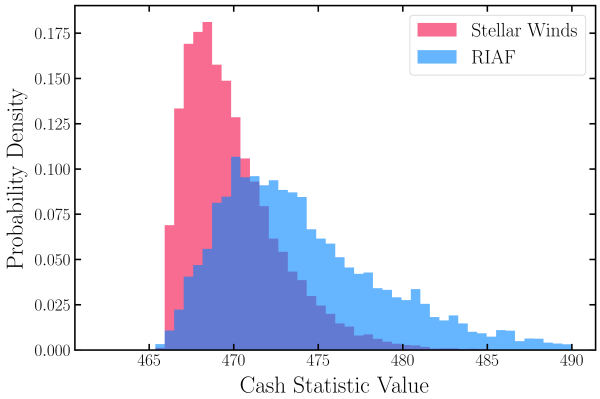


Figure 3.5: Histograms showing the Cash statistic from the posterior distributions of both the RIAF (blue) and stellar wind simulation fits (pink).

to approximate the harmonic mean of posterior probabilities, providing a more efficient estimation method compared to traditional sampling (McEwen et al., 2021). By leveraging predictive models trained on observed data, it offers a more tractable computational solution for estimating the Bayesian evidence. We used the open source code `harmonic` (McEwen et al., 2021) to compute the model evidence and the Bayes Factor from the posterior samples calculated in our `emcee` runs. The Bayesian evidence is larger for a model if more of its parameter space has high likelihood values and smaller for a model with large areas in its parameter space having low likelihood values. Thus, using the Bayes evidence for model selection accounts for the differences in model complexity between our RIAF and stellar wind models. The value of the Bayes factor, $\mathcal{R}$, is often interpreted using Jeffreys' scale (Jeffreys, 1998; Lee & Wagenmakers, 2013), where $0 < \log \mathcal{R} < 2$, $2 < \log \mathcal{R} < 6$, and $6 < \log \mathcal{R} < 10$ indicate the ranges for weak, moderate, and strong evidence for model H_1 over model H_0, respectively. With H_1 denoting the RIAF model and H_0 denoting the stellar wind simulations, we find that $\log \mathcal{R} \sim 2$, indicating a weak favour towards the RIAF model. However, the Bayes evidence is not strong enough to support either model for the accretion flow of Sgr A*. We note that non-linearities in the parameter space for the RIAF model make calculating the Bayes evidence challenging, adding to our conclusion the data do not strongly prefer either model.

3.4.3 Sgr A* at micro-calorimeter resolution

While the *Chandra*-HETG is not able to strongly differentiate between the stellar wind plasma and a RIAF model, new and future missions, especially those utilizing microcalorimeters, could theoretically elucidate the mechanics at play. The HETG-S provides high spectral

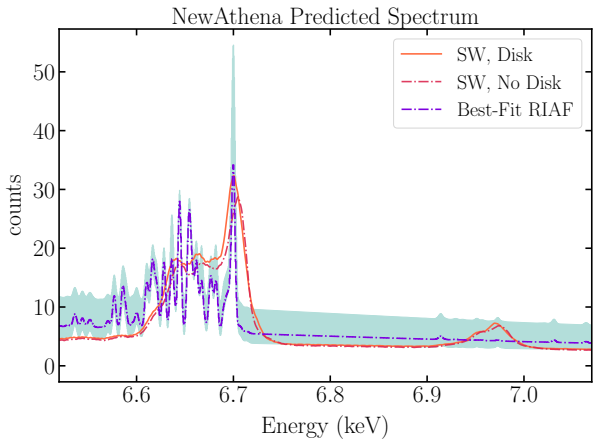


Figure 3.6: The anticipated *NewAthena* photon counts spectra for the stellar wind plasma models (red) under both disk (solid) and quasi-steady (dot-dashed) accretion scenarios in the Fe Kα region. The best-fit RIAF and contours from Chapter 2 are overlaid in blue. The stellar wind model will be differentiable from the RIAF model, and it is possible, with a high signal-to-noise, to detect signatures of the cold disk in the X-ray plasma.

resolution for point sources, reaching $\sim$ 60-70 eV at 6.7 keV, coupled with a spatial resolution of 0.5″. The approved ESA L-class mission *NewAthena*, launching late 2030s, will have an imaging resolution of 9″, and the X-IFU microcalorimeter will provide a spectral resolution of $4 - 5$ eV at 6.7 keV.[3] The advantages of microcalorimetry over a dispersive spectrograph can be seen in Figure 3.6, where we have convolved our best-fit RIAF and stellar wind models out to 5″, including ISM extinction effects, with the *NewAthena* X-IFU instrument response function. The model spectra were calculated with an exposure time of 100 ks. Unfortunately, the spatial resolution of *NewAthena* will result in spectral contamination from both PWN G359.95-0.04 and IRS 13E, which lie a projected distance of approximately 4″ from Sgr A*. It is unlikely that the signal-to-noise will be high enough to differentiate between the disk and no-disk models, but it may be possible to distinguish between the simplified RIAF model and the predictions of hydrodynamic simulations. In particular, the heightened temperatures anticipated by the stellar wind simulations can be readily tested through the detection of the 6.97 keV Fe XXVI line, which is not predicted by the current RIAF model. The *Lynx*[4] concept mission is the only concept mission that would significantly advance our understanding of the X-ray emitting accretion flow of Sgr A*. With a spatial resolution approaching 1″, *Lynx* would be able to isolate Sgr A* from nearby PWN G359.95-0.04 and IRS 13E. The unprecendeted sensitivity of *Lynx* would open a completely new window on the Sgr A* accretion flow, possibly allowing for constraints on the bulk and

[3] https://www.cosmos.esa.int/web/athena/supporting-sci-documents
[4] https://www.lynxobservatory.com/mission

turbulent motions of the hot plasma.

3.5 Summary & Conclusions

Besides black hole accretion models, hydrodynamic simulations of shocked plasma from colliding winds of nearby WR stars alone can accurate reproduce the X-ray spectrum of Sgr A*. We investigate whether the formation of a cold accretion disk, seen in both grid-based (Calderón et al., 2020) and particle-based codes (this work), leaves signatures in the gas resolvable by X-ray spectroscopy. The quiescent high-resolution spectrum from the the legacy *Chandra*-HETG dataset (PIs: Markoff, Nowak, & Baganoff)[5] may hint at complex velocity structure in the plasma (Corrales et al., 2020), with possible line shifts close to the maximum line-of-sight velocities predicted by the simulations ($v \sim 1500$km s^{-1}). However, this line structure could be due to extraction techniques or stochastic fluctuations from the relatively high X-ray background.

We compare the HETG-S spectrum to hydrodynamic models that incorporate complicated velocity structure in the dynamic plasma, accounting for the unique geometry and extraction processes of the *Chandra* HETG-S instrument. Building on the work of R17, we examine the X-ray emission from updated simulations of the plasma environment around Sgr A* created by shocked WR stellar winds, using the smoothed particle hydrodynamics (SPH) code `GADGET-2`, and incorporating updates for the SMBH mass and stellar separations. These models do not consider SMBH feedback but include optically-thin radiative cooling.

We find that the stellar wind plasma cools enough to form a cool disk within the hot accretion flow in both particle-based and grid-based simulations. We are able to reproduce a disk similar to the observed $\sim 10^4$ K H30α recombination disk (Murchikova et al., 2019) when we run our SPH simulations for 3500 yr. We generate column density, X-ray intensity, and velocity maps for plasma conditions with and without the cold disk. There are minor variations in the X-ray line profiles resulting from the different accretion scenarios, evidenced by slight shifts in the Fe Kα peaks. However, these differences are not discernible with the current signal and spectral resolution of the *Chandra* HETG-S.

We compare the predicted X-ray counts histogram from the SPH simulations to a general RIAF model, described in Chapter 2 (Balakrishnan et al. 2024a). We find that the stellar winds make the plasma hotter than predicted by the RIAF. Utilizing Bayesian model evidence to select between models, we find that the RIAF model is weakly preferred. Therefore, hints of a velocity-shifted line complex in the *Chandra* high-resolution HETG spectrum is not proof of complex velocity and temperature structure, but is more likely due to statistical

[5] https://www.sgra-star.com/

noise. Spectra of Sgr A* taken by the future mission *NewAthena* may be able to differentiate between the RIAF model and stellar wind emission, depending on the strength of the observed 6.97 keV Iron line. Identifying plasma signatures of the cold disk will still be difficult solely with X-ray data. If stellar winds simulations alone, which do not include a feedback mechanism launched from within $10^4 R_g$, sufficiently explain the quiescent X-ray spectrum of Sgr A*, it suggests that accretion stalls in the outer regions of the accretion flow and that feedback is not limited to regions close to the event horizon. This implies that the day-to-day flares from Sgr A* are not necessarily the main drivers of feedback.

While *Chandra* offers the best current combination of spatial and spectral resolution, of all future X-ray missions proposed, only *Lynx* would be able to isolate the Sgr A* accretion flow from its surroundings and provide high enough sensitivity to make significant advances constraining the structure of the Sgr A* accretion flow between 10^4 and $10^6 R_g$.

CHAPTER 4

Through a Fog of Plasma: Separating SNR Sgr A East from the Sgr A* Plasma Environment

The contents of this chapter represent work that is in preparation, in collaboration with Lia Corrales, Adrien Picquenot, and Fabio Acero. We expect the manuscript to be submitted to *the Astrophysical Journal* later in 2025.

4.1 Abstract

In this chapter, we apply the signal separation technique pGMCA on stacked *Chandra* ACIS-I observations of the GC in order to separate the different X-ray emission components so that we can better understand the plasma environment, which includes supernova remnant Sgr A East and plasma surrounding Sgr A*, which overlap along our line-of-sight. By decomposing the X-ray emission and comparing results to multiwavelength images, we identify the location of the reflected shock and make maps of Fe vs. S/Ar/Ca emission, showing that the Fe emission is centrally concentrated and isothermal, consistent with other Mixed-morphology Supernova Remnant (MMSNR)s. Our findings support previous studies that suggest that dust created within the supernova remnant has survived the passage of the reflected shock. We show that the supernova remnant is exploding from within a molecular filament being pulled into Sgr A*, making it a typical case of what would happen in a star forming region. The remnant has likely vaporized clumps of molecular material, creating cavities into which the X-ray plasma is expanding unimpeded.

4.2 Introduction

SNR Sgr A East lives in one of the most intricate and densely populated regions in the Milky Way, with its iron emission peaking ∼1 arcmin in projected distance from 4.5 × 10^6 $M_\odot$ central SMBH Sgr A*. The extensive plasma region surrounding Sgr A* significantly coincides with Sgr A East in our line of sight, which complicates the analysis of each and renders previous efforts to distinguish the X-ray structures of the remnant from the plasma environment incredibly challenging. The remnant also appears to envelope the mini-spiral Sgr A West, a structure comprising three distinct streams of ionized gas channeling material from the CND to Sgr A*. This reservoir of dense, warm molecular and atomic gas, with a mass of 10^5–10^6 $M_\odot$, spans 1.5–3 parsecs from Sgr A*. As infalling gas approaches the black hole, it becomes ionized by intense ultraviolet radiation from the NSC, which hosts numerous young, massive stars (Martins et al., 2007). Many of these are WR stars, whose powerful winds generate shocks that heat the surrounding medium to X-ray-emitting temperatures, creating the extended emission around Sgr A* (Cuadra et al., 2015; Calderón et al., 2020). The NSC, containing $\sim 10^7$ $M_\odot$ within the central 4 parsecs (100 arcseconds; Chatzopoulos et al., 2015), exerts a strong wind (Rockefeller et al., 2005) that may even have influenced Sgr A East's development (e.g., Ehlerová et al., 2022). Despite the extreme tidal forces and radiation environment near Sgr A*, 4% of the NSC consists of young, massive stars (∼6 Myr; Paumard et al., 2006; Martins et al., 2007), challenging conventional expectations for star formation in such a hostile region. Investigating Sgr A East, whose progenitor may have been a member of the NSC, may provide insight into the formation of this young stellar population.

Sgr A East belongs to a rare class of supernova remnants known as MMSNRs. These remnants are characterized by thermal X-ray-filled centers surrounded by radio-bright shells, a morphology that deviates from standard SNR evolution models. MMSNRs, such as W44, W28, 3C391, and W49B, often exhibit associations with molecular clouds and 1720 MHz OH masers, indicating interactions with dense ambient media (see Vink, 2012, and references therein). These OH masers arise in nondissociative, collisionally pumped C-type shocks, where the expanding blast wave compresses but does not destroy molecular material, making them unambiguous tracers of SNR–cloud encounters (Yusef-Zadeh et al., 1996, 1999b). The close association of these remnants with dense interstellar material underscores the importance of understanding their evolution, as their ejecta are most directly linked to enriching the medium from which future generations of stars will form. The origin of the centrally peaked X-ray emission and the tendency for these SNRs to have signatures of overionization remains a topic of debate. One proposed explanation is thermal conduction, which

redistributes heat and increases the central density while smoothing temperature gradients (Vink, 2012). Another scenario involves the evaporation of ambient cloudlets engulfed by the SNR shock, which increases the density in the remnant's interior (White & Long, 1991b). Like many MMSNRs, Sgr A East is in close proximity and has demonstrated interaction with nearby molecular cloud M0.02-0.07 (also known as the +50 $\mathrm{km\,s^{-1}}$ cloud) through detection of masers (Yusef-Zadeh et al., 1999a). Unlike most MMSNRs, however, the remnant is located near a significant energy source that may have supplied the additional energy required for overionization. Rather than resulting from interactions with dense ambient material, the overionization in Sgr A East may have been driven by past activity of Sgr A*, potentially influencing the remnant's evolution.

Sgr A East displays a complex set of spectral and morphological properties that reflect its evolution in this unique and densely populated environment. In radio, it appears as a nonthermal shell (Yusef-Zadeh, 1986), while in X-rays it has very concentrated 6.7 keV Fe Kα emission, with an X-ray centroid offset by 5 pc from Sgr A* (Maeda et al., 2002; Park et al., 2004). The X-ray core appeared to extend only 2 arcmin (Maeda et al., 2002), in comparison to the radio shell which is $\sim$ 10 arcmin across (Yusef-Zadeh, 1986) suggesting significant interaction with gaseous structures nearby. Overlapping molecular cloud contours on X-ray emission, Park et al. (2004) found that Sgr A East is unlikely to be interacting with the 20 $\mathrm{km\,s^{-1}}$ cloud (M0.13−0.08), but has had its expansion inhibited by the 50 $\mathrm{km\,s^{-1}}$ cloud located Northeast of Sgr A* (Tsuboi et al., 2011). Absorption features from Sgr A West indicate the majority of the remnant is behind Sgr A* (Yusef-Zadeh & Morris, 1987). The concentrated iron core implies that a reflected shock (an inward-propagating wave driven back into the ejecta when the blast wave encounters dense ambient gas such as the circumstellar cavity; Chiotellis et al., 2024) has already propagated inward, reheating the ejecta (Maeda et al., 2002; Park et al., 2004). The center of the iron core is displaced by roughly 5 pc from the radio shell center (Maeda et al., 2002), it is elongated along Galactic latitude (Sakano et al., 2004), and it displays a steep lateral iron abundance gradient with faint protrusions extending toward Sgr A* (Park et al., 2004). Models of a remnant expanding into a pre–existing density gradient can reproduce the offset and ellipticity (Ehlerová et al., 2022) but fail to generate the sharp abundance gradient and one–sided protrusions. These features might still require an intrinsically asymmetric explosion or tidal distortion by the SMBH's gravitational field (Rimoldi et al., 2015). *Chandra* and *XRISM* spectral analysis of the remnant indicate the presence of recombination lines, characteristic of overionization that could be due to past Sgr A* activity (Ono et al., 2019), or driven by other processes such as thermal conduction or adiabatic expansion (Yusef-Zadeh et al., 2010; Zhao et al., 2013). Its evolution in this complex environment has complicated estimates of some

significant properties, such as its age.

Estimates of the age of Sgr A East vary, but it is generally thought to be around 10,000 years old. For instance, if the gas in the region were moving at velocities typical of noncircular motions near the Galactic nucleus (50 $\mathrm{km\,s^{-1}}$), a displacement of 2.5 parsecs could be the result of a supernova event approximately 50,000 years ago (Yusef-Zadeh & Morris, 1987). Maeda et al. (2002) estimated an age of 12.5 kyr using the Sedov-Taylor model, assuming a shock velocity of 1000 $\mathrm{km\,s^{-1}}$ (derived from iron line broadening) and an ambient density of 10^3 $\mathrm{cm^{-3}}$, while accounting for shearing by Galactic rotation. On the other hand, Tsuboi et al. (2011) estimated an older age of 200 kyr, citing shock velocities around 50 $\mathrm{km\,s^{-1}}$ derived from CS/CO line measurements. However, this figure likely overstates the age as it does not factor in the turbulence present within the surrounding cloud structures. Simulations that incorporate a wind generated by the NSC generally suggest a younger age of 1,000 to 2,000 years (Rockefeller et al., 2005; Yalinewich et al., 2017). The cannonball pulsar (CXO J174540.0-290031), moving at ∼500-1000 $\mathrm{km\,s^{-1}}$ away from the Sgr A East center, has been hypothesized to be the progenitor of the remnant, and if so dates the remnant to approximately 9000 years old.

A deeper understanding of Sgr A East offers valuable insights into several astrophysical questions. For instance, how has the remnant's evolution been shaped by the wind generated by the nuclear star cluster? Was the progenitor of Sgr A East a Type Iax or Type II supernova, and what can the remnant's properties reveal about the progenitor star? The spatial distribution of iron-rich ejecta and the hot plasma cavity within Sgr A East can provide clues about the explosion dynamics and the nature of the progenitor. Additionally, the past expansion of Sgr A East, if accurately dated, could have triggered past outbursts of Sgr A* (see, e.g., Baganoff et al., 2003). Furthermore, studying Sgr A East as an MMSNR can shed light on the broader population of mixed-morphology remnants, particularly in terms of their interaction with dense environments and the mechanisms driving their unique X-ray morphologies. In this work, we aim to unravel the complex interactions between the various substructures within the central few arcminutes of the Galactic Center. Using 1.5 Ms of *Chandra* ACIS-I observations, we apply signal separation technique pGMCA (Poissonian Generalized Morphological Component Analysis; Section 1.3.3) to decompose the extended X-ray emission surrounding Sgr A*. By isolating distinct substructures and analyzing their contributions, we aim to elucidate the dynamical processes and evolutionary history of the supernova remnant.

Section 4.3 outlines the *Chandra* data reduction and stacking procedures, as well as the supplementary multiwavelength datasets incorporated to construct a comprehensive interpretation of the underlying mechanisms. In Section 4.4, we conduct an exploratory analysis

of the X-ray data, identifying salient features that inform subsequent pGMCA decomposition in Section 4.5. Section 4.6 contextualizes the pGMCA-derived components within a multiwavelength framework to derive their physical properties. Finally, we conclude with a synthesis of our findings.

4.3 Datasets

First, we describe the complementary multiwavelength datasets used to build a complete physical understanding of the X-ray plasma components isolated by signal separation technique pGMCA. Next, we detail the processing and stacking of all the archival *Chandra* ACIS-I observations used in this work to study the diffuse and extended X-ray plasma structures. The exact procedures taken to remove point sources and create diffuse X-ray images can be found in Appendix Chapter A.

4.3.1 Multiwavelength Datasets

To get a better idea of the landscape surrounding Sgr A East, we used images and datasets from several published works and/or publicly accessible archival data. Some of the more visually useful datasets are pictured in Figure 4.1, while all are briefly described in bullet point form below.

- SCUBA (on the James Clark Maxwell Telescope) CMZ Survey (Pierce-Price et al., 2000): Traces dense molecular material. The image shows the molecular filament into which Sgr A East appears to be expanding, made up of the "50 $\mathrm{km\,s^{-1}}$" and "20 $\mathrm{km\,s^{-1}}$" clouds as they have been referred to previously. (Figure 4.1; panel A)

- PPMAPS: Dust temperature maps from the Herschel HI-Gal survey (Marsh et al., 2017). The output units represent the column density of material with dust at a specific temperature for each sky position. For example, a 10 K map shows column densities (in N_{H_2}) where dust grains are near 10 K. The maps we use show the gas density associated with dust ranging from 20 to 50 K. The morphology of the dust changes greatly between 21 and 37 K, in particular. (Figure 4.1; panels B-D)

- VLA 5.5 GHz continuum image (Zhao et al., 2016): Highlights the radio shell of the supernova remnant and the four HII regions to the East of Sgr A East. Also shows some radio cavities and some protruding emission to the West. (Figure 4.1; panel E)

- SOFIA FORCAST 37.1μm warm dust emission ($\mathrm{T_{dust}} \sim 100$ K) (Lau et al., 2015): The warm dust emission morphology is very different to any other dataset. The nearby HII

regions East and Northwest of the Sgr A East are very bright. In addition, there is material that seems to surround the minispiral and co-spatial with plasma in the CND. There is also a protrusion in the West that is cospatial with the Western plume in the radio data. (Figure 4.1; panel F)

- Pa-α 1.875 μm continuum from the HST NICMOS Galactic survey. Point sources have been removed and the image has been processed. The emission in this panel arises from hot H gas that is recombining (5000-15000 K) (Wang et al., 2010). (Figure 4.1; panel G)

- ALMA observations of G0.02-0.07 (the 50 $\mathrm{km\,s^{-1}}$ MC) (Tsuboi et al., 2019): We use SiO emission maps at a range of velocities. This gas is a tracer of shocked material, with concentrations in the minispiral and numerous discrete blobs. The emission seems to be clustered at $\sim 0\ \mathrm{km\,s^{-1}}$ and $\sim 50\ \mathrm{km\,s^{-1}}$, suggesting two major interaction fronts.

- 1720 MHz OH Masers (Sjouwerman & Pihlström, 2008) and Class I 44 GHz Methanol Masers (McEwen et al., 2016), showing interaction sites at a variety of velocities.

4.3.2 Chandra Data

As mentioned in Section 1.1.2, ACIS-I is paramount for this work, as its field of view fully encompasses the supernova remnant and its surroundings, unlike ACIS-S. In this chapter, we utilize 1.5 Ms of *Chandra* archival ACIS-I observations, spanning over two decades, listed in Table 4.1. All observations during which the Galactic Center transient AX J1745 (located southwest of Sgr A*) was in outburst were excluded from our analysis. Due to its extreme brightness, an unusually large extraction radius was required for point source removal, which would have significantly impacted the data. Since these observations constituted only a small fraction of the total exposure time (in Ms), we opted to remove them entirely. All data was cleaned and analyzed using CIAO 4.17.

We created a merged event file with a total exposure time of 1.3 Ms by stacking 80 individual *Chandra* observations (listed in Table 4.1). To minimize contamination from background flares, we extracted light curves below 2 keV from the outer regions of the CCDs—areas primarily dominated by particle background—and removed time intervals affected by flaring. After flare filtering, we performed astrometric alignment across all observations by matching World Coordinate System (WCS) references using the `celldetect` tool. Observations with insufficient exposure time for reliable point-source detection were excluded from the final merge. The resulting dataset consists of the OBSIDs listed in Table 4.1, reprojected and co-added with `reproject_obs`, following standard *Chandra* analysis threads.

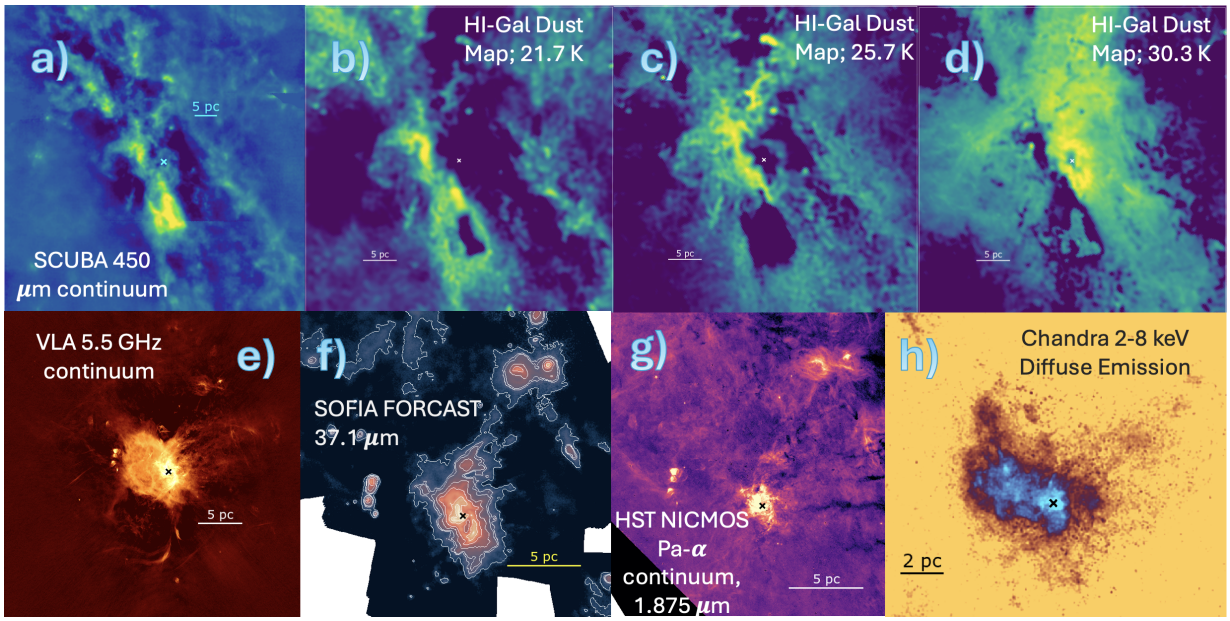


Figure 4.1: View of the region of interest in several different wavelength bands. In all panels, North is up and East is to the left, and an "X" denotes the location of Sgr A*. *a)* SCUBA 450μm continuum image, showing the distribution and density of the molecular gas; *b) - d)* Herschel HI-Gal dust temperature maps, reflecting the column density of material at a given dust temperature (labelled) along that line of sight (Marsh et al., 2017) ; *e)* VLA 5.5 GHz continuum image of the region, showing the extent of the supernova remnant shell (Zhao et al., 2016); *f)* SOFIA FORCAST 37.1μm emission, characterizing the warm dust in the region (Lau et al., 2015); *g)* HST NICMOS 1.875 μm Pa-α continuum (Wang et al., 2010); *g)* Chandra 2-8 keV diffuse emission, with point sources removed, showing the major plasma components: the Sgr A* plasma environment and the supernova remnant (this work).

For the diffuse emission analysis, we identified and masked point sources using `wavdetect` (details provided in Appendix Chapter A). We generated flux-calibrated images with `flux_obs`, masked out point sources, and filled the masked regions using `dmfilth` to achieve a smooth background. Finally, we applied exposure correction by dividing the flux images by their corresponding energy-dependent exposure maps, also produced by `flux_obs`. The resulting diffuse emission maps are shown in Figure 4.2.

4.4 Data Exploration

In this section, we examine the diffuse X-ray emission and energy hue maps to establish the physical context for interpreting our pGMCA results. The diffuse emission maps help in identification of energy-dependent morphological structures, while the energy hue maps highlight spectrally distinct structures. Together, these complementary methods characterize both the spatial distribution and spectral properties of the emission components across different energy bands, providing critical benchmarks for validating and interpreting the components derived from pGMCA.

4.4.1 Diffuse Emission

Following point source removal, we followed the procedures outlined in the CIAO documentation[1] to create images of the diffuse X-ray emission. The resulting exposure-corrected images across four energy bands are presented in Figure 4.2, each revealing different aspects of the diffuse X-ray emission in the GC region. The top left panel shows the broadest energy band image, with photons between 2−8 keV. Here, both the remnant and plasma bound to Sgr A* are visible, but not distinct. In the 1−2.6 keV band (top right panel), we detect faint emission from the Sgr A* plasma environment, along with a cloud of diffuse emission to the top right. The complete absence of the supernova remnant's morphology in this band strongly suggests that the SNR plasma is substantially hotter than the material surrounding Sgr A*. Between 2.6−5 keV, we start to see a structure emerge to the left of Sgr A*. This band contains the majority of the photons in our *Chandra* observations. Transitioning to higher energies (bottom right panel), the supernova remnant structure becomes more visible, while the plasma around Sgr A* lacks clear morphology. This aligns with previous studies that characterized the SNR morphology using 6−7 keV photons, as the remnant has strong Fe Kα emission (Maeda et al., 2002). However, even in this band, the remnant's morphology remains somewhat ambiguous – an issue we hope to solve with pGMCA.

[1] https://cxc.harvard.edu/ciao/threads/diffuse-emission/

OBSID	Exposure Time (ks)	Start Date
2953	11.59	2002-04-19
2952	11.86	2002-03-23
2951	12.37	2002-02-19
2954	12.45	2002-05-07
5954	17.82	2005-08-01
13016	17.83	2011-03-29
13017	17.83	2011-03-31
14941	19.82	2013-04-06
14942	19.83	2013-04-14
23295	23.37	2020-07-03
3549	24.79	2003-06-19
22707	25.69	2020-07-02
9170	26.80	2008-05-06
9172	27.44	2008-05-11
9169	27.60	2008-05-05
9171	27.69	2008-05-10
9173	27.77	2008-07-26
9174	28.81	2008-07-25
6363	29.76	2006-07-17
2943	37.68	2002-05-22
3663	37.96	2002-05-24
5951	44.59	2005-07-27
5952	45.33	2005-07-29
5953	45.36	2005-07-30
242	45.92	1999-09-21
22937	48.43	2020-08-20
5950	48.53	2005-07-24
1561	49.30	2000-10-26
4683	49.52	2004-07-05
4684	49.53	2004-07-06
11843	78.93	2010-05-13
3665	89.92	2002-06-03
10556	112.55	2009-05-18
3393	158.03	2002-05-28
3392	166.69	2002-05-25

Table 4.1: List of the *Chandra* observations used in this chapter and their respective exposure times and start dates.

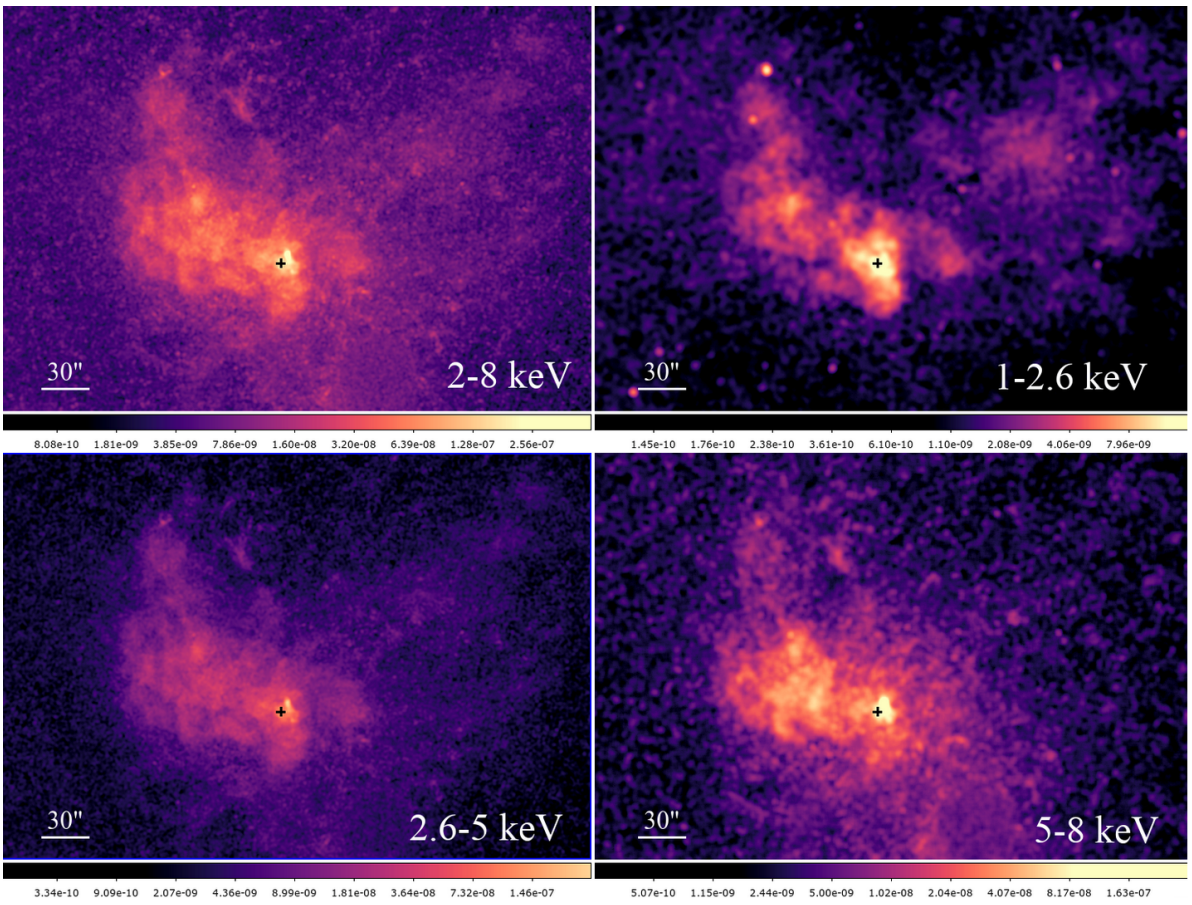


Figure 4.2: The results of stacking 1.3 Ms *Chandra* ACIS-I observations, listed in Table 4.1. Each image has a 30" bar in the bottom left. We have separated the data into the four energy bands of main interest: 2−8 keV (full band; top left), 1−2.6 keV (Si and S; top right), 2.6−5 keV (Ar; bottom left), and 5−8 keV (Fe; bottom right). Note that the smoothing scales differ between images.

4.4.2 Energy Hue Maps

Next, we developed energy hue maps to help visualize spectral information present in the X-ray data cube. We used `dmnautilus` to generate a map file identifying regions containing a sufficient number of photon counts, followed by `statmap` to calculate the per-pixel median energy values. Subsequently, we applied `aconvolve` to smooth the resulting energy map. The resulting median energy maps were then combined with diffuse X-ray intensity images (not exposure-corrected) to create a composite visualization where hue corresponds to photon energy, while lightness and saturation reflect the raw X-ray brightness in each pixel. Since median energy calculations depend on photon properties rather than detection efficiency, we used raw (non-exposure-corrected) intensities; exposure correction modifies count rates, but not spectral information.

The resulting energy hue maps generated using $2-8$ keV photon events is shown in Figure 4.3. The left panel highlights several prominent features that stand out in this visualization of the data. There are two areas with redder median pixels that are still X-ray bright. The northeast (NE) plume is brighter than the Western protrusion. Additionally, we label the iron core, which is visually more distinct in Figure 4.4. This region has the highest median pixel energies in the whole bright X-ray emission structure. A large, soft diffuse structure extends across the western portion of the image, possibly linked to past activity from Sgr A* (see, e.g. Maeda et al., 2002). The diffuse plasma near Sgr A* exhibits median energies softer than those of the iron core but slightly harder than redder X-ray features identified elsewhere in the field. Overlaid in the right panel are contours from the VLA 5.5 GHz continuum image (Zhao et al., 2016), which traces the approximate boundary of the SNRs radio shell. The iron core aligns approximately with the structure's center, and notably, the radio emission is significantly more extended than the X-ray-bright region.

To further investigate the hard X-ray components, we produced an additional energy hue map restricted to 5–8 keV photons (Figure 4.4). In this higher-energy band, the iron core of the SNR stands out starkly against the surrounding emission, confirming its significantly harder spectral nature compared to the softer plasma near Sgr A*. The spatial-spectral segregation strongly suggests that the SNR emission is dominated by higher-energy processes, potentially including non-thermal emission or highly ionized plasma, while the Sgr A* environment appears dominated by cooler thermal emission or distinct physical mechanisms.

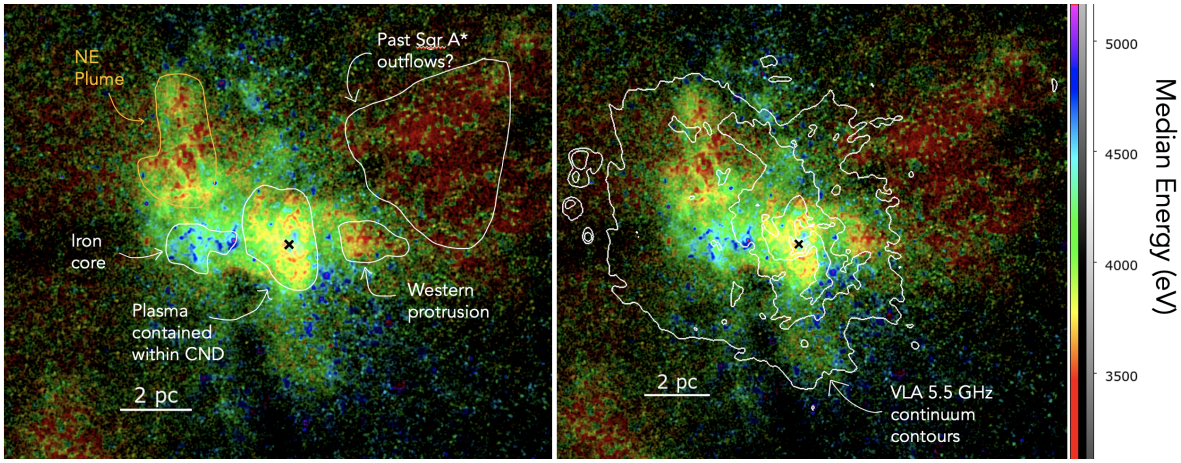


Figure 4.3: Both panels show energy hue maps spanning 2−8 keV, but differ in labeling. The color of each pixel is dictated by its median energy, while the lightness and saturation are determined by the X-ray intensity in that pixel. The median energy colorbar is shown on the right. LEFT: We identify spectrally differentiated features of interest. RIGHT: Overlaid are radio contours of the supernova remnant shell from (Zhao et al., 2016). Note that unlike the diffuse emission images, these are not exposure corrected; see text for details.

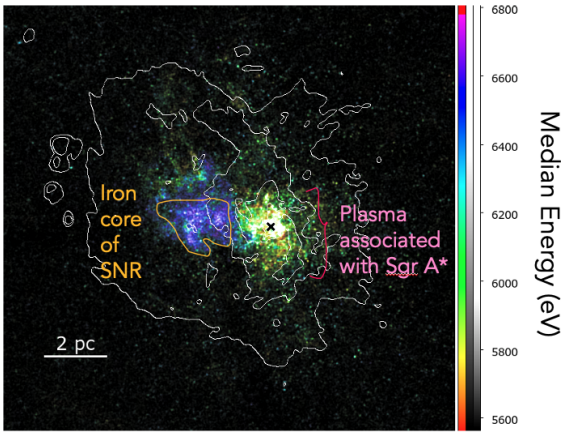


Figure 4.4: Energy hue maps generated only with photons between 5−8 keV. Here, the distinction between the SNR Iron core and the plasma surrounding Sgr A* is highlighted. The plasma associated with Sgr A* seems to correspond to median energies ∼6-6.2 keV while the SNR Iron core has median pixel energies closer to 6.7 keV.

4.5 pGMCA Results

To separate different plasma components, we used a blind source separation method based on GMCA (Bobin et al., 2015). GMCA presumes Gaussian-distributed noise, pGMCA models Poissonian counting statistics, making it far better suited for X-ray analyses. In this section, we briefly describe the algorithm and past applications, followed by our results in applying pGMCA to the point source-removed stacked ACIS-I data cube.

4.5.1 Methods

GMCA is a blind signal separation technique that works best in separating *spatially overlapping but morphologically and spectrally distinct* components. The original algorithm was designed to extract a CMB image from *Planck* data (Bobin et al., 2016), and relies on the sparsity of the wavelet transforms of all the (x, y) slices of the (x, y, E) data cube, in order to fully exploit both the three-dimensional nature of the data and the morphological diversity of the components to retrieve. Without any prior physical or instrumental information other than the number n of components to retrieve, the algorithm is able to disentangle n images, each one being associated with a mean spectrum. This disentanglement is made possible by the use of wavelet transforms on the (x, y) slices of the data set, because wavelets carry information on morphological features at different scales that allow the algorithm to separate morphologically distinct components.

This method was first introduced for X-ray observations by Picquenot et al. (2019). An updated version, the pGMCA, was developed to take into account Poisson statistics in Bobin et al. (2020). Both algorithms proved their ability to extract detailed and unpolluted maps of faint components from *Chandra* observations of extended sources (see for example Picquenot et al., 2021; Olivares et al., 2025). However, the lack of prior physical information makes the spectral reconstruction challenging, and the algorithm is usually more efficient at disentangling components in narrow energy bands. pGMCA's capabilities make it a great candidate to study the GC and Sgr A*.

4.5.2 Outputs

We applied pGMCA to the stacked, ACIS-I observations with point sources removed. The *Chandra* ACIS detector has a pixel scale of 0.492 arcsec and a full width at half maximum (FWHM) energy resolution of approximately 110 eV at 6.7 keV. To produce spectra with physical meaning, we rebinned the energy axis into 10 eV channels, allowing for accurate reconstruction of spectral features. Spatially, we grouped the native $0.492''$ pixels into $4''$

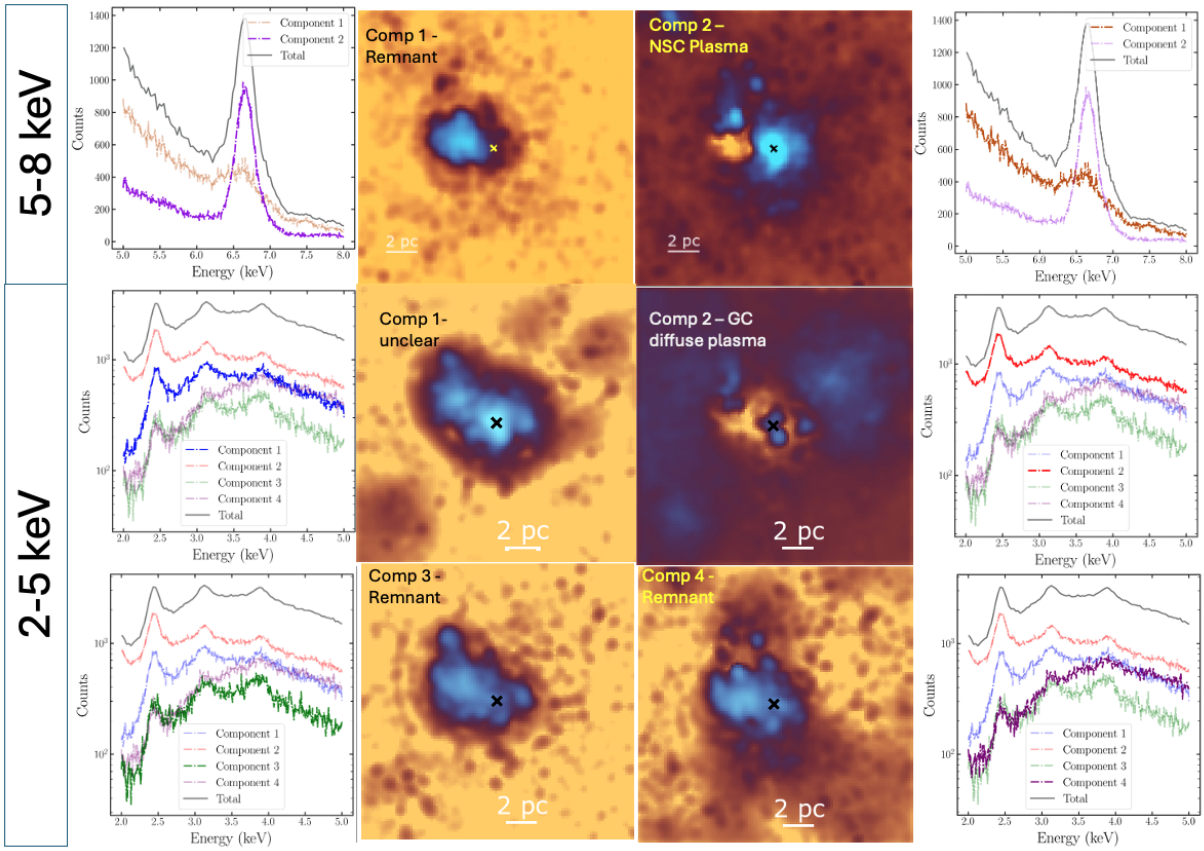


Figure 4.5: GMCA outputs and corresponding spectra. The output images have been divided by exposure maps created with `flux_obs`. All images are on the same log-spaced colorbar, with a scale bar denoting 2 pc and an "X" at the position of Sgr A*. The top row shows the two main components seen between 5−8 keV, while the bottom two rows display the four components identified by the algorithm in the 2−5 keV energy range. Each component is labeled with notation we refer to throughout this work.

bins to boost signal-to-noise without sacrificing the telescope's effective PSF resolution.As noted in the previous section, pGMCA performs optimally when applied to narrow energy intervals and is less effective across broad energy bands. We found that running the algorithm separately on the 2–5 keV and 5–8 keV bands yielded robust component separation, whereas narrower energy ranges were limited by insufficient signal-to-noise.

Figure 4.5 shows our results from applying pGMCA to photons between 5−8 keV (top row) and 2−5 keV (middle and bottom row). Each image has a scale bar denoting the extent of 2 pc (50 arcseconds at 8.1 kpc) and an X at the position of Sgr A*. Each highlighted spectrum (bolded color) is shown next to its morphological counterpart. The total spectrum in the respective energy band is also plotted in dark gray. We omit the noise components for brevity. Note that we have exposure corrected these images; we took the output pGMCA

components and divided them by exposure maps binned to match the input pGMCA data cube at the corresponding energies. We briefly note features of the images and spectra below, then compare them to multiwavelength images to interpret their physical significance in the following section.

5−8 keV components: Application of pGMCA to the 5−8 keV band cleanly isolates the 6.7 keV Fe-Kα line emission (Iron Component 1), confirming its primary origin in Sgr A East rather than astrophysical processes associated with Sgr A*. The center and extent of this feature is coincident with the higher energy emission seen in the 5−8 keV energy hue map (Figure 4.4) and the 5−8 keV diffuse emission (Figure 4.2). The next component (Iron Component 2) exhibits negligible emission in the SNR core, and the Fe-Kα line profile displays a slight energy offset (∼30 eV), indicative of a lower-ionization plasma. The shape of the plasma surrounding Sgr A* retrieved by pGMCA is morphologically very similar to the 1−2.6 keV plasma surrounding Sgr A* seen in Figure 4.2.

2−5 keV components: (1) Component 1 shows emission co-spatial with the NE plume and Western protrusion seen in the hue maps (Figure 4.3). Stronger emission appears to be from the plasma environment of Sgr A*. (2) Component 2 is the brightest component and displays a prominent sulfur line. Its morphology is anti-correlated with that of the supernova remnant and appears co-spatial with the molecular filament. This component also has emission co-spatial with the NSC, but it is much less extended than in Component 1, and seems to be contained within the CND. Both Components 1 and 2 display vertical structures extending perpendicular to the Galactic plane, previously interpreted as potential signatures of past ejections fromSgr A* (Maeda et al., 2002). (3) Component 3 exhibits a bright core located near the center of the radio shell, suggesting an association with the supernova remnant. Its spectrum closely resembles that of Component 4 but is distinguished by the presence of a calcium emission line (4) Component 4 appears more compact than Component 3, but is similarly co-spatial with both SNR core and NSC. Comparing to Component 3, its spectral features are weaker.

We fit the spectrum of each pGMCA component to measure the line centroids and full widths at half maximum (FWHM), allowing us to compare the components and draw conclusions about the physical processes at play. We calculated the line centroids by fitting Voigt profiles to the continuum-subtracted spectra produced by pGMCA, using tools from `specutils` and `astropy.modeling`. The fits were optimized with the Levenberg–Marquardt algorithm with a least-squares minimization. Reported uncertainties correspond to 3σ errors, derived from the diagonal elements of the covariance matrix returned by each fit.

Table 4.2 gives the line centroids, corresponding FWHMs, and elemental transitions that could plausibly give rise to these lines. We note that fitting Component 4's spectrum was

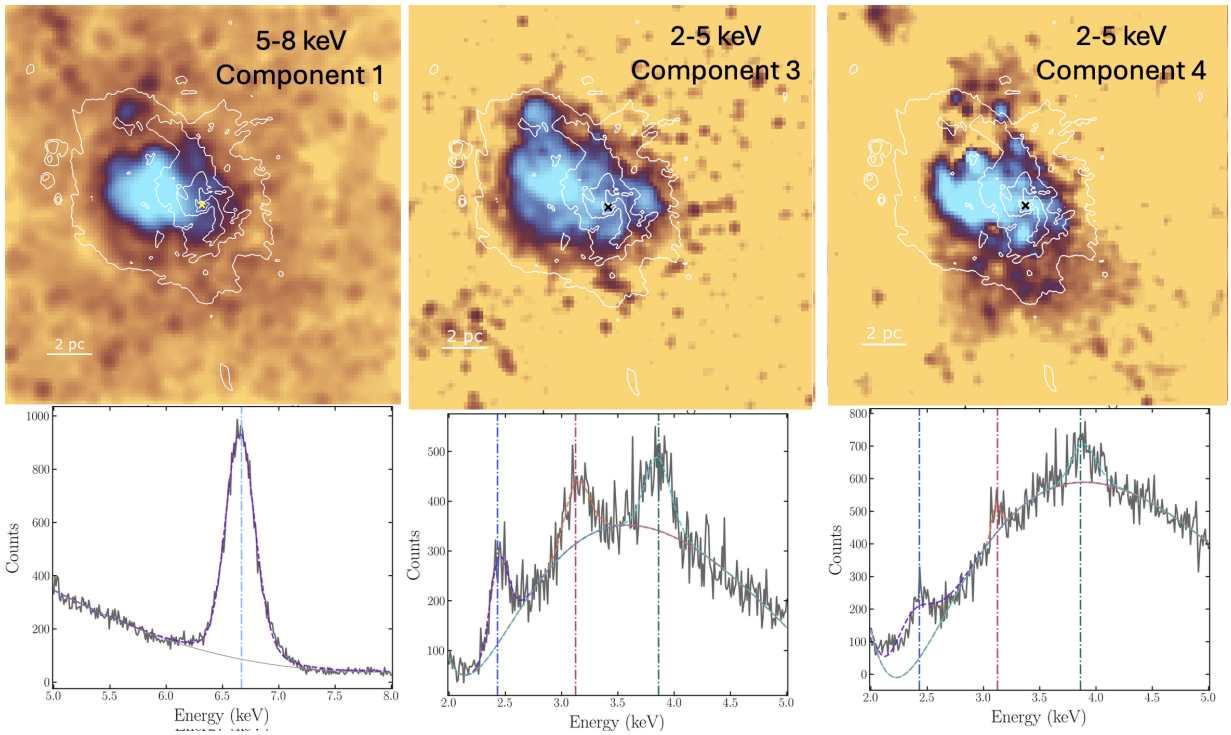


Figure 4.6: GMCA outputs we believe capture emission from the supernova remnant. Each image has the radio shell (Zhao et al., 2016) overlaid in white, an X at the location of Sgr A*, and a scale bar showing the extent of 2 parsecs in the bottom left. Below each image, we plot the associated spectrum. The panel on the left is from the 5−8 keV component, while the other two are emission components from the 2−5 keV data. The line centroids and widths can be found in Table 4.2.

particularly challenging; the algorithm had difficulty identifying peaks due to the lower strength of the 3.1 and 3.9 keV features. By eye, the 2.430 S XV forbidden line fits the peak very well. However, the derived line centroids and widths for this component should be interpreted with caution.

4.6 Interpretation

The final stage of our analysis involves physically characterizing the pGMCA-derived components by combining insights from our energy hue maps and multiwavelength images to derive their physical interpretations. In this section, we compare observed correlations and interpret the structure of the X-ray plasma in the central parsecs of our Galaxy.

Energy Band	pGMCA Component	Line FWHM (keV)	Line Centroid (keV)	Possible Ions
2–5 keV	1	0.196	2.460 ± 0.008	S XV[a]
2–5 keV	1	0.234	3.115 ± 0.014	Ar XVII[b] or S XVI[c]
2–5 keV	1	0.084	3.920 ± 0.032	Ca XIX[d]
2–5 keV	2	0.219	2.495 ± 0.007	S XV[a] or Si XIV[e]
2–5 keV	2	0.253	3.114 ± 0.009	Ar XVII[b] or S XVI[c]
2–5 keV	2	0.209	3.891 ± 0.014	Ca XIX[d]
2–5 keV	3	0.044	2.438 ± 0.016	S XV[a]
2–5 keV	3	0.064	3.126 ± 0.033	Ar XVII[b] or S XVI[c]
2–5 keV	3	0.077	3.860 ± 0.036	Ca XIX[d]
2–5 keV	4	0.194	2.369 ± 0.032*	Si XIV[e], Si XIII[f], or S XV[a]
2–5 keV	4	0.037	3.148 ± 0.030	Ar XVII[b] or S XVI[c]
2–5 keV	4	0.051	3.905 ± 0.043	Ca XIX[d]
5–8 keV	1	0.186	6.630 ± 0.028	Fe XXV[g] or Fe XXIV[h]
5–8 keV	2	0.460	6.663 ± 0.004	Fe XXV[g] or Fe XXIV[h]
a: S XV (He-like): R: 2.461 keV; I: 2.447, 2.449 keV; F: 2.430 keV; kT_p = 1.289 keV				
b: Ar XVII (He-like): R: 3.140 keV; I: 3.124 keV; F: 3.104 keV; kT_p = 1.821 keV				
c: S XVI (H-like): R: 3.107, 3.106 keV; kT_p = 2.293 keV				
d: Ca XIX (He-like): R: 3.902 keV; F: 3.861 keV; kT_p = 2.573 keV				
e: Si XIV (H-like): R: 2.377, 2.376 keV; kT_p = 1.447 keV				
f: Si XIII (He-like): R: 2.374, 2.346 keV; kT_p = 0.967 keV				
g: Fe XXV (He-like): R: 6.700 keV; I: 6.682, 6.668 keV; F: 6.637 keV; kT_p = 5.759 keV				
h: Fe XXIV (Li-like): R: 6.682 keV; kT_p = 3.849 keV				

Table 4.2: Line features identified in the 2–5 keV band across pGMCA components. Candidate lines are matched by centroid energy and temperature peak to known transitions. Errors on the values are 3σ uncertainties. Below, we list the possible ions corresponding to the spectral features in the pGMCA outputs, with the recombination (R), intercombination (I), and forbidden (F) line centroids, along with peak plasma temperatures associated with the resonance lines.

4.6.1 The Sgr A East SNR

As seen in the previous section, applying pGMCA to the stacked and point source removed *Chandra* dataset has pulled out several components that appear centered in the middle of the 5.5 GHz radio shell (Zhao et al., 2016). Figure 4.6 shows the components from Figure 4.5 that we attribute to the supernova remnant, overlaid with the 5.5 GHz continuum VLA contours in white (Zhao et al., 2016). The images have the same colorbar and limits.

Examining the pGMCA spectra and morphologies of three key components in Figure 4.6 reveals their distinct physical origins. The 5−8 keV component forms a compact, uniformly bright core reminiscent of the isothermal centres seen in mixed-morphology supernova remnants. Its spectrum is dominated by a strong Fe Kα line at 6.663 ± 0.004 keV with a full width at half maximum of 0.46 keV, indicating a highly turbulent, iron-rich plasma localized in the remnant's core. By contrast, the 2−5 keV component 3 extends farther to the north and west and exhibits a broader, less concentrated core whose peak is offset from the iron centre. Its spectrum shows comparably strong sulfur, argon and calcium lines, consistent with a multi-temperature plasma composed of supernova ejecta, and the spatial offset suggests element-dependent mixing within the remnant. The 2−5 keV component 4 isolates the lower-energy continuum underlying the iron emission. The corresponding spectrum exhibits weak spectral features compared to the other pGMCA outputs.

To see how this compares to the X-ray emission overall, in Figure 4.7, we plot the pGMCA contours from the left and middle panels in Figure 4.6 in white and yellow, respectively. The line-dominated 2−5 keV component is co-spatial with the NE plume and Western protrusion described earlier (Section 4.4.2), implying the supernova remnant has extended up and to the East. The Fe Kα line emission is more concentrated, and looks centered on the high value median energy pixels in the previously denoted Iron core.

To contextualize the interaction between Sgr A East and its surrounding environment, we compare our results to multiwavelength datasets capturing emission between 10 K and 50 K. Adjacent to Sgr A East lies a molecular filament, historically divided into distinct components: the 50 km s^{-1} cloud to the east and the 20 km s^{-1} cloud to the south. However, this structure forms a continuous filament connected by magnetic field lines (see panel A in Figure 4.1) and exhibits a smooth velocity gradient, decreasing from 50 km s^{-1} in the southwest to 20 km s^{-1} in the south (Coil & Ho, 2000). This filament is traced by SCUBA 450 μm emission (Figure 4.1, panel A), which reveals cold dust at temperatures of 10–20 K (Pierce-Price et al., 2000), while HI-Gal derived dust maps (PPMAPs; Figure 4.1, panels B-D) resolve distinct dust structures at intervals between 10 and 50 K (Marsh et al., 2017). Surveys of OH 1720 MHz and Class I methanol (44 GHz) masers detect numerous masers along the filament. Those in the 20 km s^{-1} cloud are associated with ongoing star formation,

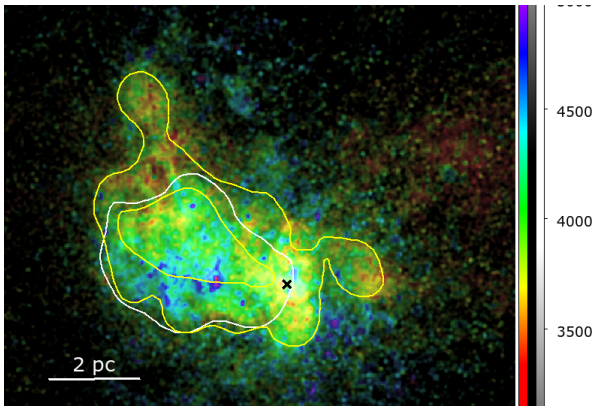


Figure 4.7: Median energy map of 2−8 keV photons (identical to Figure 4.3). The brightness and saturation in each pixel correspond to the X-ray intensity, while the color corresponds to the median energy (colorbar in units of eV). Overlaid in white and yellow are the left and middle panels, respectively, from Figure 4.6. The 2−5 keV ejecta component is co-sptial with the two X-ray bright and red features seen in Figure 4.3. The Iron line component appears to be ceneterd on high median energy pixels, the iron core denoted in Figure 4.3.

while masers near 0 and 50 km s^{-1} likely trace shocks or cloud-cloud collisions (Yusef-Zadeh et al., 1999a; Pihlström & Sjouwerman, 2006).

A schematic from Murchikova et al. 2019 (top panel, Figure 4.8) illustrates the filament's kinematic structure, with Galactic rotation markers overlaid. The Galactic plane is denoted in yellow, where "×" symbols represent material moving away from the observer and "o" symbols material approaching. This configuration indicates that the 50 km s^{-1} component of the molecular filament (in Figure 4.1, not pictured in the schematic) should be redshifted along the line of sight due to Galactic rotation.

In Figure 4.8, we compare pGMCA 2−5 keV Component 3 (right) to N_{H_2} column density maps corresponding to dust with $T_{dust} \sim 25.7$ K (left). The colorbars have been chosen to highlight contrast. Note that gaps in the column density do *not* imply a lack of dust, in fact, the material surrounding Sgr A* contains dust closer to 30-40 K (see Figure 4.1, panel D). We also overplot 44 GHz Class I Methanol masers (McEwen et al., 2016); the legend explaining the color scheme is to the left of the image. On the pGMCA image, we have overlaid contours corresponding to the N_{H_2}, and highlighted with pink arrows areas of interest. Both arrows are pointing to areas where it is clear that the X-ray emission is being compressed against material, preventing it spreading further. The dust in this molecular material is at 25.7 K, warmer than the dust associated with the 20 km s^{-1} material to the South (see Figure 4.1). Along with previous maser observations (see, e.g. McEwen et al., 2016) which cluster along the X-ray ridge, indicating regions of enhanced density and shock excitation, this implies the remnant's expansion has heated the 50 km s^{-1} cloud and compressed dust.

The bottom pink arrow marks the sharp interface between the pGMCA component and the 25.7 K dust, delineating the reflected-shock front. At this boundary, ejecta heated by the reflected shock has been compressed and thermalized, creating the nearly isothermal core. Masers at both 0 $\mathrm{km\,s^{-1}}$ and 50 $\mathrm{km\,s^{-1}}$ cluster along this edge, confirming that the reflected shock propagates simultaneously toward and away from us along our line of sight.

In Figure 4.7, we show the energy hue map on the left and SCUBA 450 μm continuum map on the right. The cyan contours trace the dense molecular gas. In the left panel, the color delineates the median energy of the pixel. Overlaying the SCUBA contours reveals that red, X-ray bright regions align precisely with cavities devoid of cold (10-20K) and dense molecular gas. The spatial correlation between cold dust and hard X-ray regions also implies that greener areas in the hue map trace molecular material lying in front of the remnant. This foreground gas absorbs soft X-rays, thereby raising the median photon energy.

4.6.2 Plasma associated with the NSC and/or Warm Dust

We identify two components that are spatially coincident with warm dust and hot gas features (Figure 4.1; panels F and G). Figure 4.10 show images and spectra of pGMCA 2−5 keV Component 1 and 5−8 keV Component 2, with HST NICMOS Pa-α 1.875 μm (hot gas) and SOFIA Forcast 37.1 μm (warm dust; $\mathrm{T}_{dust} \sim 100K$) contours overlaid in white and pink, respectively. The arrows indicate locations where the contours of the corresponding color align with the pGMCA-extracted component, highlighting spatial coincidence. In the left panel, the X-ray emission is co-spatial with the warm dust in the NE plume and the hot gas protruding to the East and West of Sgr A*. The 5−8 keV component is co-spatial with the warm dust in the NE plume and hot gas in the Western direction, but not the extension to the East.

Looking at the spectra, the 2−5 keV component has three features at 2.46 ± 0.008 keV (S XV), 3.115 ± 0.014 keV (could be Ar XVII at 3.124 or 3.104 keV, or S XVI at 3.106 or 3.107 keV), and 3.920 ± 0.032 keV (Ca XIX). The FWHMs for the first two lines are $\sim$ 0.2 keV, while the Calcium FWHM is closer to 0.01 keV. The 3.115 keV line centroid is in between the two strongest possible lines, the Ar XVII 5-1 transition at 3.124 keV and the Ar SVII 2-1 transition at 3.104 keV, both peaking in plasmas at $kT_e \sim 1.7$ keV. It could also be lines associated with S XVI closer to 3.107 keV, which would correspond to $kT_e \sim 2.3$ keV. As the S XV feature is strongest, corresponding to temperatures between $kT_e = 1.22 - 1.29$ keV, the plasma is likely closer to the lower range $\sim 1.2 - 1.3$ keV. Meanwhile, the 5−8 keV component has a broad Iron line centered at 6.63 ± 0.03 keV and a FWHM of 0.186 keV. The Iron line here is weaker and slightly redshifted (by $\sim$ 30 keV) compared to the Iron core

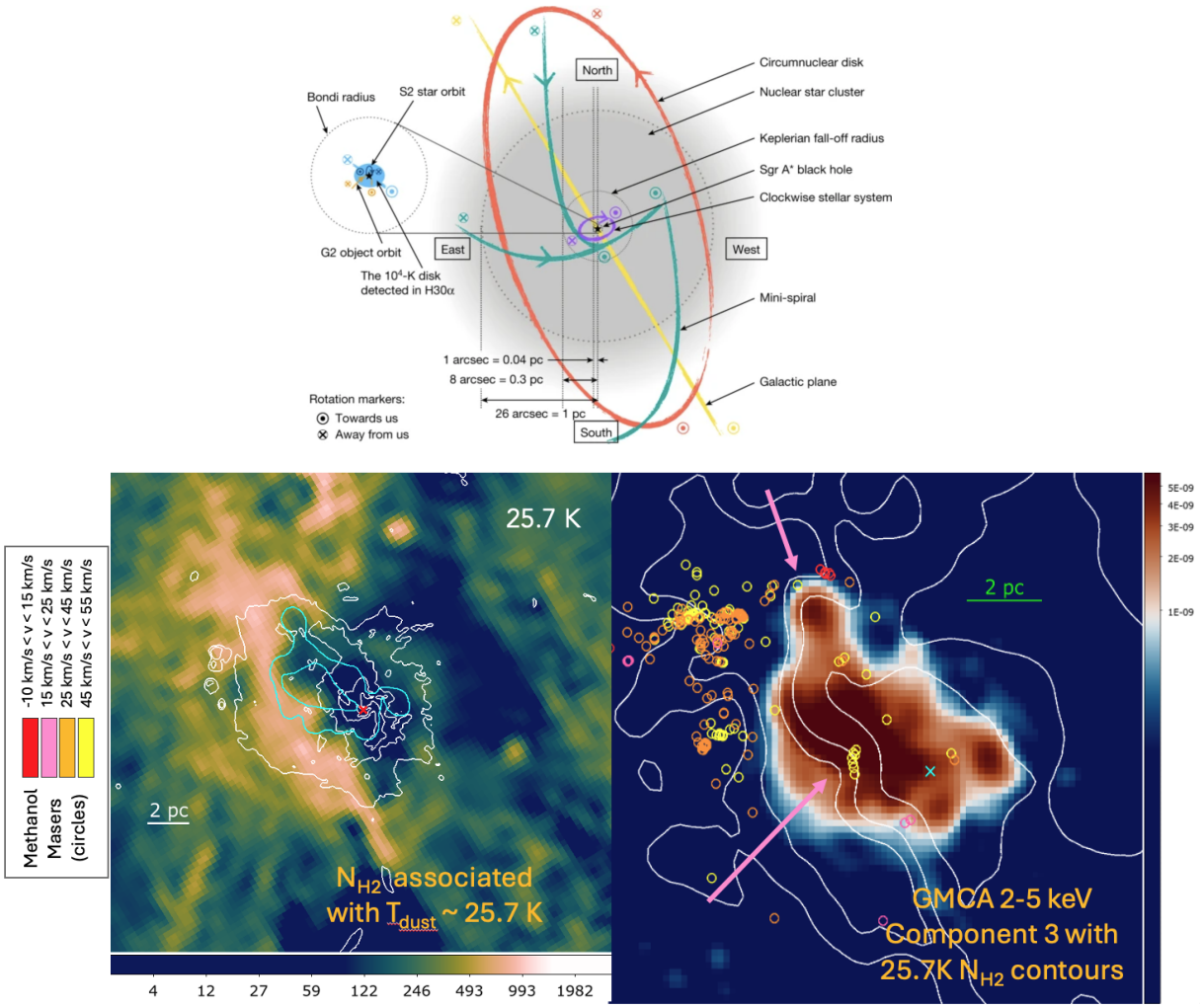


Figure 4.8: TOP: Schematic from Murchikova et al. 2019 showing the extents of various structures within and associated with the CND. The schematic has rotation markers, showing that the molecular filament is expected to be redshifted along the line of sight due to Galactic rotation. BOTTOM LEFT: N_{H_2} column densities of gas associated with dust at 25.7 K (derived from HI-Gal plane survey dust maps Marsh et al., 2017), with VLA 5.5 GHz contours and 2−5 pGMCA Component 3 contours in white and cyan, respectively. RIGHT: pGMCA 2−5 keV component 3, from Figure 4.6, with 44 GHz methanol masers (McEwen et al., 2016) plotted (maser legend is to the left) and contours from the 25.7 K emission. The pink arrows in the bottom right image highlight regions where it appears the X-ray plasma is pushing up against material associated with 25.7 K dust.

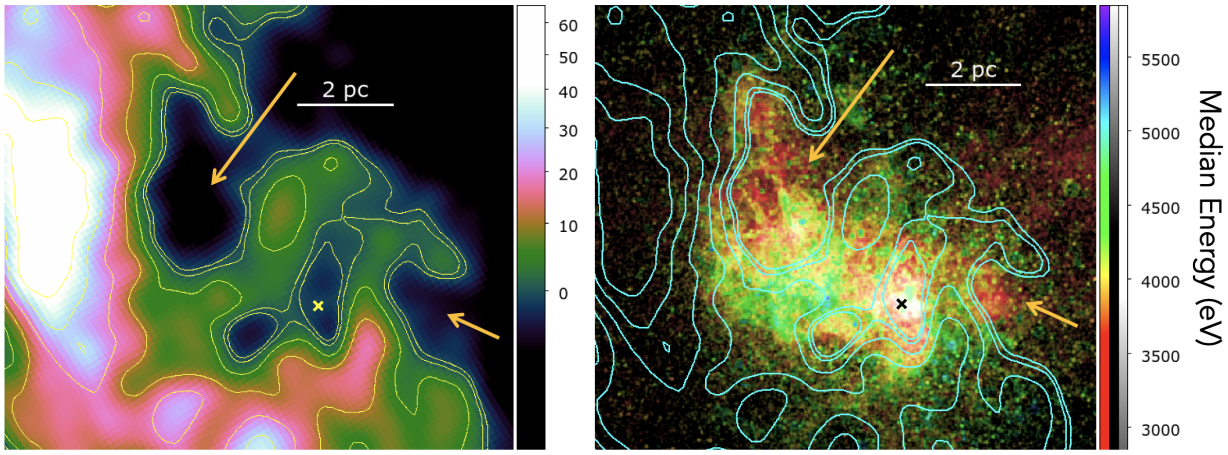


Figure 4.9: LEFT: SCUBA 450 μm emission (colormap) with overlaid contours. RIGHT: 2–8 keV energy hue map, with the same contours from the left panel shown in cyan. Arrows mark gaps in the molecular material, and the red regions in the energy map correspond precisely to these holes. This alignment indicates that the SNR lies behind the molecular gas where the median pixel energy is higher, since the softer X-ray emission has been absorbed by the foreground material.

(5−8 keV Component 1), indicating lower abundance or temperature.

The warm dust emission observed by SOFIA Forcast, specifically the region highlighted with a green arrow in Figure 4.10, was analyzed in previous work by Lau et al. 2015. In that work, the authors found that this region of dust emission exhibited an average temperature of 100 K, significantly higher than the 75 K expected for typical 0.1 μm ISM grains heated by the NSC, implying a population of smaller grains (0.01 μm). They postulated that the dust was located *within* Sgr A East due to a spatial distribution anti-correlated with hard X-ray (2-8 keV) emission, suggesting a cooler, denser ejecta region. The absence of cold dust and ionized gas emission further excluded a scenario in which the dust was in a foreground cloud. SED modeling incorporating SOFIA and Spitzer data required a mix of very small grains (VSGs, $\sim$0.001 μm) and larger grains (LGs, $\sim$0.04 μm), with a VSG-to-LG mass ratio (15–90%) exceeding typical ISM values (13%). Compositional constraints ruled out PAHs, favoring amorphous carbon, and derived a dust mass of about 0.02 $M_\odot$.

The 2−5 keV component in particular (Figure 4.10; left) aligns precisely with the ionized gas protruding from Sgr A*/NSC, identifying these blobs as hot pockets of plasma. This ionized material likely originates in the NSC, but it is unclear why it is extending perpendicular to the Galactic plane, instead of following the plume in the Northwest.

As mentioned, both of these pGMCA components are co-spatial with the dust component characterized by Lau et al. 2015 (green arrow in Figure 4.10). However, no corresponding X-

ray emission is detected from the H II regions to the East of the remnant, or the northwestern protrusion visible in the dust contours and the radio contours (e.g. Figure 4.1). This difference strongly suggests two distinct heating mechanisms: the dust that overlaps X-ray emission has been shock-heated by the supernova blast wave, whereas the dust embedded in H II and in the NW protruding structure is warmed predominantly by stellar UV photons. Additionally, the NE plume and Western protrusion (labeled in Figure 4.3) were both seen in pGMCA Component 3 (Figure 4.6; middle), which we attribute to ejecta/swept up material from the remnant. Together with the fact that these H II regions lie outside the current reflected-shock radius (Section 4.6.1), our findings bolster Lau et al.'s conclusion that this dust resides inside the remnant shell and has survived the passage of the reflected shock.

4.6.3 Diffuse GC Plasma

In Figure 4.11, we show the image and spectrum of 2−5 keV Component 2. This spectral component is the most prominent among all pGMCA outputs, with the highest number of counts. Table 2 shows the measured spectral features with tentative identifications. The lines show consistent broadening of $\Delta E = 0.2$–0.25 keV, the widest among the components, indicating a turbulent, diffuse, and optically thin plasma.

Morphologically, this component is largely absent in the region coincident with the remnant, but it appears muted in areas associated with the 20 $\mathrm{km\,s^{-1}}$ molecular cloud, and it is brightest toward the 50 $\mathrm{km\,s^{-1}}$ component, NE plume, material *within* the CND, the Western protrusion, and the emissions perpendicular to the Galactic plane linked to past outflows (Maeda et al., 2002). Please see Figure 4.3 for our nomenclature. Its morphology shows minimal correlation with any of the dust emission maps used in this work, which span dust temperatures from 10 to 1000 K, but does have heightened emission in certain molecular gas cavities, supporting the interpretation that the emission arises from a diffuse, optically thin plasma. The spatial distribution implies a line-of-sight geometry where a larger portion of the plasma lies between the observer and the 50 $\mathrm{km\,s^{-1}}$ material, while the 20 $\mathrm{km\,s^{-1}}$ material is positioned closer to us, farther "in front" of the plasma. This configuration is consistent with findings from previous studies (see, e.g. Coil & Ho, 2000). The elevated emission observed in the NE plume, Western protrusion, and outflows perpendicular to the Galactic plane likely arises due to molecular cavities in these regions, allowing us to see the near and far sides of the plasma. Meanwhile, the plasma within the CND is likely bright due to the large amounts of optically thin and turbulent plasma generated by the colliding stellar winds.

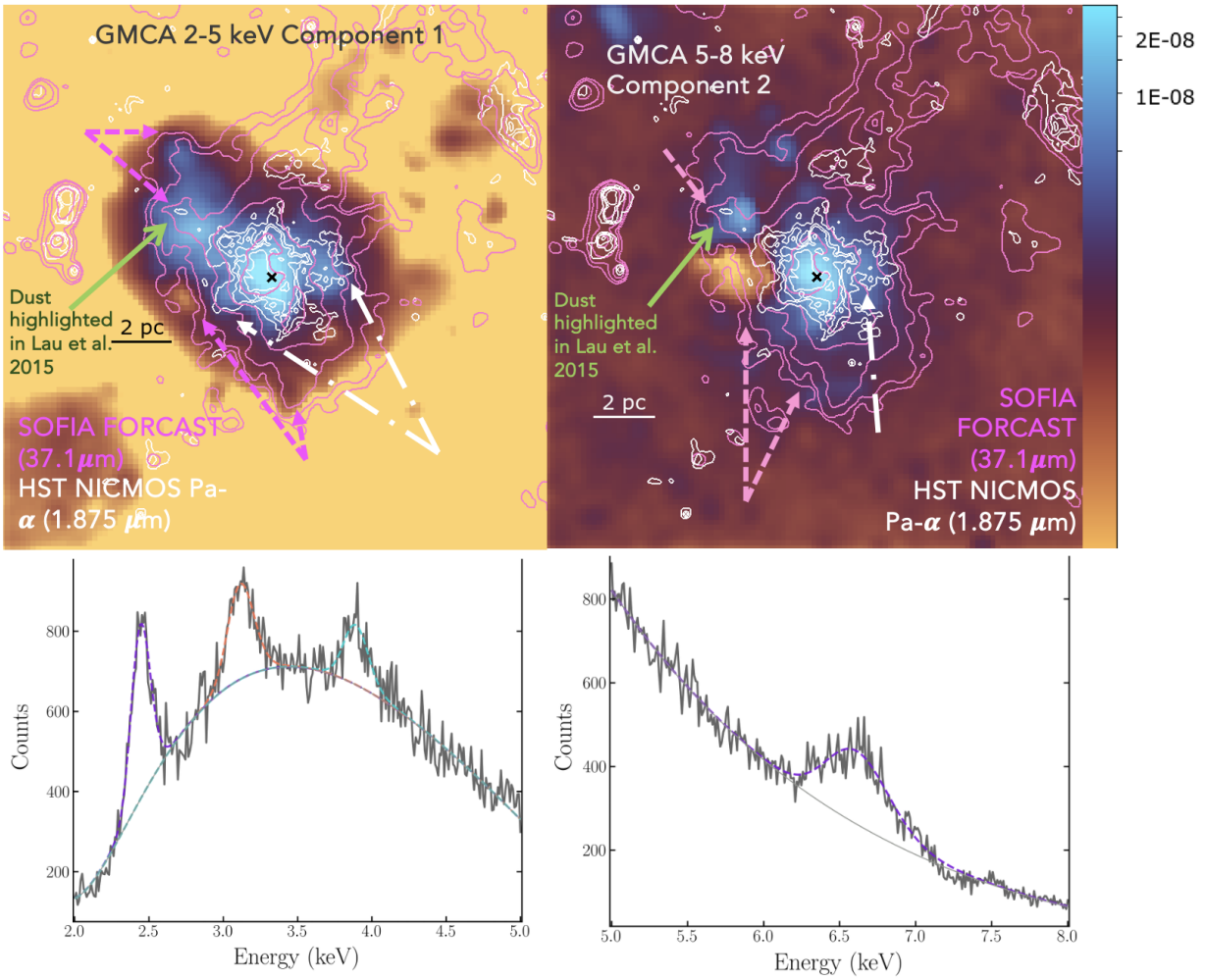


Figure 4.10: GMCA outputs that appear co-spatial with warm and hot gas emission. Each image has cnotours from 37.1μm $\sim$ SOFIA FORCAST dust emission ($T_{dust} \sim 100K$) and 1.875 μm Pa-α HST NICMOS $\sim$ ($T_{gas} \sim 100K$) emission in pink and white, respectively. They also have an X at the location of Sgr A* and a scale bar showing the extent of 2 parsecs in the bottom left. The panel on the left is emission between 2$-$5 keV while the panel on the right is emission between 5$-$8 keV. The pink and white arrows denote regions where the contours align particularly well with the pGMCA extracted component. The corresponding spectra are plotted below each image, with continuum and line fits that were used in the calculation of line centroids listed in Table 4.2. The component on the left traces hot plasma pockets that coincide with both the NSC and dust within the Sgr A East shell (Lau et al., 2015). This implies that the dust (denoted by the right arrow) has endured the passage of the reflected shock and has been shock heated.

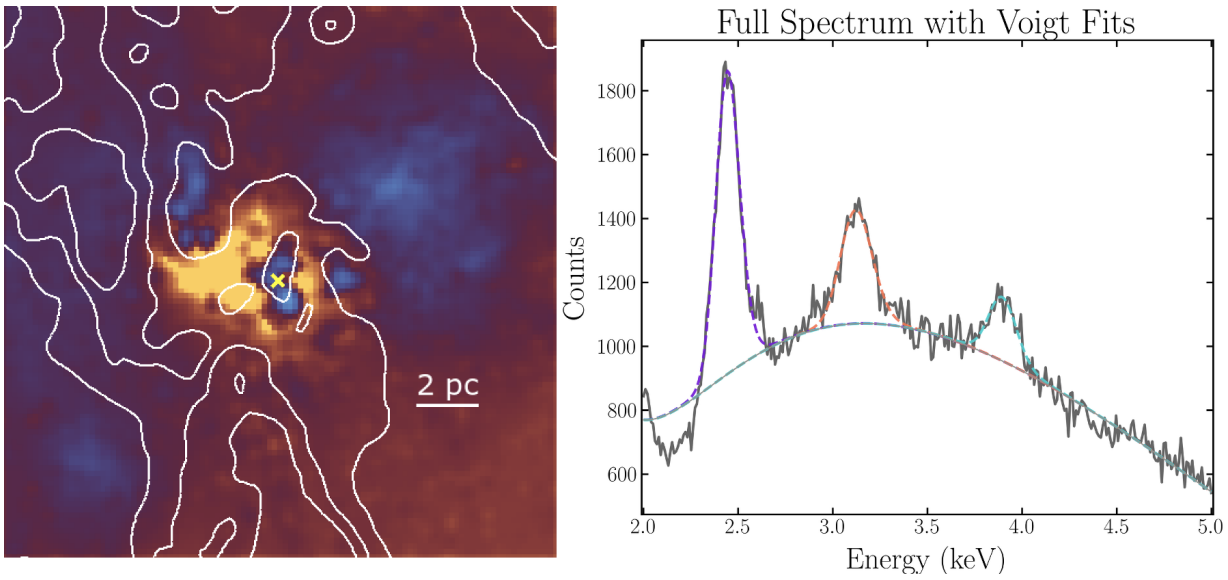


Figure 4.11: GMCA 2−5 keV Component 2. On the left, the image is overlaid with contours from the SCUBA 450 μm continuum (Pierce-Price et al., 2000). The colorbar is consistent with the other pGMCA outputs, an "X" marks the location of Sgr A*, and a 2 pc scale bar is shown on the bottom right. On the right, the spectrum is dominated by a strong feature at 2.4 keV. This component displays the broadest lines of all pGMCA outputs, indicative of a diffuse and turbulent plasma.

4.7 Summary

In this work, we have presented the first application of pGMCA on *Chandra* observations of the central ∼30 parsecs. We showed that pGMCA isolates physically meaningful components from the data. These features were hinted at through narrow band imaging in previous studies (see, e.g. Maeda et al., 2002; Wang, 2022), but have now been revealed spatially and spectrally isolated from other plasma components. We also demonstrate the power of combining pGMCA with multiwavelength observations to better understand complex, interacting environments.

Our analysis began by creating diffuse emission maps and median energy maps to identify key features in the X-ray data. These provide a basis for interpreting our subsequent application of pGMCA. We then applied pGMCA to 1.3 Ms of stacked and point source removed ACIS-I observations, and compared our results to complementary multiwavelength datasets to establish robust physical interpretations. Below, we list our main results.

The pGMCA algorithm was particularly effective in separating line emission from the supernova remnant (Figure 4.6, left panel), whose center is clearly offset from broader Iron emission in the 5−8 keV band (Figure 4.10), which is co-spatial with the NSC and CND.

In the 2−5 keV band, pGMCA separated two extended components that are both centered

on the middle of the radio shell (middle and right panel of Figure 4.6), suggesting they are associated with the supernova remnant. 2−5 keV Component 3 has strong lines from S XV, Ar SVII, and Ca XIX, suggestive of a multitemperature plasma, and suggesting that this component is ejecta and swept up material. Comparing these results to median pixel energy maps, we see that the Iron core is co-spatial with regions of high median pixel energy, while the S/Ar/Ca component extends further, encompassing areas with redder X-ray emission.

GMCA 2−5 keV Component 3 is clearly interacting with the molecular filament. Regions of low median photon energy lie where dense molecular gas is absent, indicating that these sightlines suffer minimal soft-photon absorption. Meanwhile, the central regions of the remnant appear to be harder due to molecular material in the foreground that has not been vaporized. Comparing to 25.7 K dust maps, we saw a clear interface between the pGMCA component and the dust, the reflected-shock front, inside which compressed ejecta have thermalized. Moreover, maser emission at both 0 $\mathrm{km\,s^{-1}}$ and 50 $\mathrm{km\,s^{-1}}$ along the reflected-shock boundary confirms that the shock is expanding outward from within the molecular cloud in both directions along our line of sight.

Previous SOFIA/FORCAST observations of the warm dust highlighted by Lau et al. (2015) revealed a compact region within Sgr A East at an average temperature of 100 K, indicating the population is likely made up mostly of very small grains (~ 0.01 μm). The co-location of our pGMCA Components with the Lau et al. dust feature, along with lack of X-ray emission from HII regions, confirms that the warm dust was heated by a different mechanism, like shock heated, and has endured the reflected shock and remains embedded within the supernova remnant.

GMCA 2–5 keV Component 2 appears to be associated with diffuse plasma. It is anti-correlated with the supernova remnant but shows spatial overlap with several notable structures, including the NE plume, material within the CND, the Western protrusion, soft X-ray features previously linked to past outflows from Sgr A* (Maeda et al., 2002), and the 50 $\mathrm{km\,s^{-1}}$ component of the molecular filament (see Figure 4.3 for labelling). Its apparent absence in regions associated with the 20 $\mathrm{km\,s^{-1}}$ cloud likely results from line-of-sight absorption, implying that the 20 $\mathrm{km\,s^{-1}}$ material lies between us and the majority of the plasma. The plasma within the CND is likely bright due to the presence of abundant optically thin, turbulent plasma generated by the stellar winds. In contrast, the enhanced emission seen in the NE plume, Western protrusion, and ejections perpendicular to the Galactic plane likely arises from molecular cavities in those regions, allowing us to see the near and far side of the plasma.

Overall, this study provides a much clearer separation of the X-ray components in the central arcminutes than preivously achieved. It validates the long-standing picture of Sgr

A East as a MMSNR evolving in a dense environment, now with detailed maps of the iron core and S/Ar/Ca plasma. The remnant has strongly influenced the Galactic Center; it has expanded into, compressed, and shock-heated the 50 km s^{-1} molecular material immediately adjacent to the 20 km s^{-1} cloud believed to feed the CND. Additionally, we demonstrate that the supernova explosion has likely carved out cavities in the surrounding molecular gas, reshaping the three-dimensional structure of the region. In addition to the SNR-specific features, we separate out the diffuse, turbulent GC plasma component that pervades most of the field of view, showing that this ambient plasma and the SNR ejecta are spatially and spectrally distinct. Finally, by tracing the dust emission, we support findings from Lau et al. (2015), who find that the dust has survived the shock passage and implies that older SNRs can retain dust grains long into their evolution. demonstrating that dust survives passage through the reflected shock and indicating that mature SNRs can preserve dust grains over extended timescales.

The remnant's proximity to Sgr A* suggests a mutual influence, in which Sgr A East has both impacted and been shaped by the evolution and behavior of the SMBH. The SNR's spectrum indicates temperatures of $kT \sim 2 - 5\,\mathrm{keV}$ out to $\sim 2\,\mathrm{pc}$ (Baganoff et al., 2003). Such a pervasive hot medium implies inefficient radiative cooling: for plasma at $n_e \sim 1\,\mathrm{cm}^{-3}$ and $kT \sim 3\,\mathrm{keV}$, the cooling time is $t_{\mathrm{cool}} \sim (3/2)\,kT/(n_e\Lambda) \approx 10^{7-8}\,\mathrm{yr}$ (Draine, 2011), orders of magnitude longer than the SNR's estimated age of $\sim 10^4\,\mathrm{yr}$. Therefore, the presence of the supernova remnant maintains high thermal energy in the surrounding gas, preventing it from efficiently cooling and collapsing onto Sgr A*. This sustained shock heating likely reduces the rate at which ambient gas accretes onto the black hole. At the same time, feedback from the SNR may influence star formation by maintaining high thermal pressure and turbulence. In particular, the spatial correlation between our pGMCA 2–5 keV Component 3 and the 25.7 K dust filament shows that the shock has compressed the gas to higher densities, potentially triggering star formation in nearby clouds while preventing fragmentation within the shell itself (Lau et al., 2015). Shock–excited OH masers and surviving warm dust further attest to the remnant's ongoing interaction with dense gas (Yusef-Zadeh et al., 1997). These findings portray Sgr A East as a significant agent of energy injection in the Galactic Center that, over its $\sim 10^4\,\mathrm{yr}$ lifetime, has kept the circumnuclear environment of Sgr A* hot and dynamically turbulent.

CHAPTER 5

Conclusions

In this dissertation, we set out to learn more about the high energy plasma environment of Sgr A*, specifically:

a) How does Sgr A*'s environment affect its behaviour? We utilized *Chandra* high-resolution spectroscopy to model the accretion flow, shaped by the surrounding NSC plasma, on arcsecond scales.

b) How does Sgr A* influence its surroundings? We isolated Sgr A East from the line-of-sight overlapping accretion flow, using data-driven techniques to show how this SNR and the plasma environment of Sgr A* are interacting on arcminute scales.

As we summarize below, by combining *Chandra*'s sensitivity with data-driven techniques, we have improved our understanding of both the Sgr A* accretion flow and the nature of SNR Sgr A East. We developed a physically motivated model tailored to *Chandra*'s gratings and showed it matched analytical predictions for inefficient accretion flows. Next, we tested state-of-the-art hydrodynamic simulations of the colliding stellar winds in the central parsec for a range of plasma configurations, including models incorporating the hypothesized cool accretion disc. By directly comparing these simulated spectra to our *Chandra* observations, we demonstrate that, within the limitations imposed by the current data, the X-ray predictions from simulated stellar winds are consistent with those for inefficient accretion flows. Finally, we used signal separation of X-ray data in combination with multiwavelength datasets to illuminate the location of the reverse shock front in Sgr A East and how it may have vaporized parts of its natal molecular cloud, in addition to confirming the presence of shock-heated dust. Together, these findings underscore the notion that multi-scale feedback from colliding winds to supernova shocks fundamentally shapes the density, temperature, and kinematics of the gas around Sgr A*, thereby influencing its accretion mode.

5.1 Examining the X-ray Spectrum of Sgr A* with a RIAF Model

The Milky Way's SMBH Sgr A* accretes at an exceptionally low rate despite its location within a dense and dynamic environment shaped by stellar winds from neighboring massive stars. This underluminous state renders Sgr A* a particularly valuable case study for exploring radiatively inefficient accretion processes. Leveraging the high spatial resolution of Chandra, which allows us to separate Sgr A* from nearby X-ray sources, we modeled the HETG-S high-resolution gratings spectrum of the quiescent accretion flow.

In Chapter 2, we employed a physically motivated Radiatively Inefficient Accretion Flow (RIAF) model, explicitly accounting for the geometry of the *Chandra* gratings and the distribution of emitting plasma along the line of sight. Our RIAF model took into account the extraction size of the gratings pipeline and contaminating non-dispersed photons that may have been captured by the gratings extraction. Our best-fit model yielded density and temperature power-law indices of $s = 0.74$ $(-0.22, +0.66)$ and $q = 0.22$ $(-0.22, +1.35)$, respectively, in broad agreement with previous multiwavelength analyses. These values suggest a quasi-equilibrium between inflow and outflow components. Notably, our spectral fits also favored sub-solar iron abundances, which may reflect iron depletion onto dust grains.

Our study focused on the information-rich Fe XXV emission features. Future studies could include extracting the spectrum from different annuli, allowing the RIAF s parameter, which controls the slope of the density profile, to change with radius. Comparing these results to trends in the multiwavelength SED (Yuan & Narayan, 2014; Ma et al., 2019) could reveal whether the observed increase in outflow fraction with radius still holds. Another possible avenue of investigation could be to test whether similar results hold using the Medium Energy Grating (MEG), which covers the 0.4-5 keV range, in contrast to the High Energy Grating (HEG) used in our work, which spans 0.8-10 keV[1]. One could also model both the MEG and HEG spectra together, in addition to the non-gratings ACIS-S CCD spectrum, tying together the density and temperature profiles in order to model the accretion flow structure over the entire *Chandra* band.

[1]https://cxc.harvard.edu/proposer/POG/html/chap8.html

5.2 Examining the X-ray Spectrum of Sgr A* with SPH Simulations

In Chapter 3, we expanded upon our HETG-S analysis by comparing our RIAF results with updated SPH simulations of colliding stellar winds from massive stars within the central parsec. We ran these simulations for >3000 years and found that the SPH results can produce a transient, cold ($\sim 10^4$ K) disk, such as the one reported in H30α observations (Murchikova et al., 2019), when evolved over long timescales. This outcome is consistent with previous stellar wind simulations that use AMR (Calderón et al., 2020), showing that the formation of the disk is invariant to numerical method used. While the synthetic spectra generated from disc and no-disc scenarios were not distinguishable with *Chandra*, we found that the SPH simulations successfully reproduced key features of the X-ray gratings spectrum, indicating that both the RIAF and stellar wind scenarios are capable of accounting for the current data within the constraints of *Chandra*'s sensitivity.

However, the SPH model (using Fe abundances of 0.6–1 $Z_\odot$, depending on WR subtype) predicts a hotter X-ray plasma than the RIAF model (best-fit Fe: 0.3 $Z_\odot$). We note that temperature and Fe abundance are degenerate when fitting only the Fe Kα complex. Resolving spectral differences near the Fe XXVI line at 6.97 keV to distinguish between the RIAF and stellar-wind plasma models will require a substantial leap in instrumental capability beyond *Chandra*, which has little effective area at this energy. While XRISM's *Resolve* (Tashiro et al., 2025) instrument offers excellent spectral resolution (5 eV), its limited spatial resolution (30″) means that it is unable to isolate the Sgr A* accretion flow from surrounding sources. Future observatories such as NewAthena, equipped with a microcalorimeter providing 2.5 eV resolution and an angular resolution of 9″[2], *may* disentangle these overlapping components, however, contamination will remain a challenge. Differentiating between models has implications for understanding the impact of Sgr A*'s feedback and outflows in the current quiescent accretion state.

Heightened spatial/spectral sensitivity provided by future microcalorimeters would also help resolve the kinematics and composition of the stellar winds originating in the nuclear star cluster. These winds reach velocities of several thousand km/s (Genzel et al., 2010) and are thought to be dominated by contributions from Wolf-Rayet stars. With improved energy resolution and higher spectral throughput, upcoming missions like NewAthena will be able to resolve plasma components with bulk velocities down to a few hundred km/s, enabling direct comparison with hydrodynamic simulations of stellar wind collisions. Breaking the degeneracies between velocity broadening, temperature, and abundance in these winds will help

[2] https://www.esa.int/Science_Exploration/Space_Science/NewAthena_factsheet

constrain the elemental composition of the hot plasma and, by extension, the abundances of the Wolf-Rayet stars themselves, which remain poorly known (Anastasopoulou, 2025). Together, these capabilities promise to open a new window into both the nature of quiescent accretion and the complex interplay between massive stars and our central supermassive black hole.

5.3 Examining the Emissions of Sgr A East using GMCA

The inner Galactic environment is further shaped by energetic feedback from massive stellar evolution, particularly core-collapse supernovae, which redistribute metals, heat dust and gas, and restructure the local interstellar medium (Gall et al., 2011). In Chapter 4, we examined Sgr A East, a mixed-morphology supernova remnant (MMSNR) situated only a few parsecs from and overlapping in our line of sight with Sgr A*. Its location within the high-pressure, high-density nuclear environment offers a rare opportunity to investigate supernova feedback and stellar evolution in extreme conditions.

Drawing upon 1.3 Ms of deep *Chandra* ACIS-I observations, we applied signal separation technique GMCA. This methodology enabled the separation of overlapping spatial and spectral emission features, revealing a complex, multiphase structure within the remnant. We identified morphological correlations between the X-ray plasma and dust structures observed in the infrared. The central regions of the SNR exhibit a pronounced concentration of iron-rich ejecta. Encircling this core is a more extended component enriched in intermediate-mass elements, e.g. sulfur, argon, calcium; this configuration is a signature of known MMSNRs. Comparing the morphology of the intermediate-mass elements to maps of dust at 25.7 K, we identify the location of the reverse shock. Additionally, the intermediate-mass-rich ejecta spatially coincide with warm ($\sim$100K) dust, suggesting that the SNR has shock-heated the dust to high temperatures. The warm dust component appears to have survived shock passage and remains embedded within the central ejecta, suggesting that this dust has survived the passage of the reverse shock (as suggested in Lau et al., 2015).

We also uncovered a few regions of X-ray emission coincident with gaps in molecular material (and warm dust), suggesting that the remnant could have vaporized molecular gas in the area. This molecular gas is likely associated with the 20–50km/s cloud complex and appears to be funneling material from the Central Molecular Zone toward the vicinity of Sgr A* (Molinari et al., 2011). By disrupting and heating this inflowing molecular reservoir, Sgr A East likely perturbs and heats the cold gas supply to Sgr A*. Additionally, our

component analysis revealed a sulfur-rich plasma with broadened spectral features anti-correlated with the SNR but distributed across the field of view, indicative of turbulent, hot ambient medium.

Future missions such as AXIS, offering arcsecond-scale imaging over 0.3−10 keV and a flat PSF[3], will aid in resolving finder substructures within the SNR, possibly identifying molecular clumps through X-ray absorption. Increased sensitivity offers the potential to disentangle velocity shifts in the plasma, as demonstrated in SNR Cas A (Picquenot et al., 2019), further constraining the dynamics of the plasma. When complemented by high-resolution X-ray spectroscopy, these observations will advance our understanding of the mechanisms governing dust destruction, chemical enrichment, and energy deposition in the center of our Galaxy.

5.4 Future Directions: From the Central Parsecs to Galactic Scales

The recent discovery of the eROSITA bubbles (∼ kpc scale; Predehl et al., 2020) and the Galactic chimneys (∼100s of pc scale; Ponti et al., 2019) has renewed interest in the structure, origin, and energetics of large-scale outflows from the GC. Whether these features are predominantly the result of past episodes of enhanced accretion onto Sgr A* or are instead driven by concentrated nuclear star formation remains an open question. Resolving this ambiguity requires precise constraints on the thermal, chemical, and morphological properties of the X-ray-emitting plasma associated with these outflows.

As a future postdoc at McGill, I plan to extend the GMCA-based signal separation pipeline to archival *Chandra* *XMM-Newton*, and *eROSITA* datasets covering the chimneys and bubble interiors. Spatially resolved spectroscopy of the decomposed components will enable measurement of temperature, ionization state, and elemental abundances, thereby constraining the outflow's history and energy injection mechanisms. I will also investigate whether the large-scale plasma retains signatures of stellar wind origin or whether it bears the imprint of AGN-like outbursts. For example, stellar-wind driven plasmas should be relatively cooler and smoothly varying compared to AGN outbursts, which should produce sharp boundaries (Predehl et al., 2020). Differences in emission mechanism will also constrain the competing scenarios, as AGN activity would produce an under-ionized plasma compared to a supernova-heated gas (Fujita et al., 2022).

Ultimately, the objective of this future work is to construct a physically coherent, multi-

[3]https://axis.umd.edu/

scale framework for gas inflow, black hole accretion, and feedback-driven outflows within the Milky Way. Our GC remains the only environment in which these processes can be observed with parsec-scale resolution. As such, it offers an unparalleled laboratory for studying the coupling between black hole activity, stellar evolution, and galactic-scale structure formation. The methodologies and results developed in this dissertation provide a foundation to further our knowledge by constructing a multiwavelength picture of how Sgr A* has molded both its immediate surroundings and the broader evolution of our Galaxy. By defining robust observational "fingerprints" of stellar versus AGN-driven feedback, we can then extend these diagnostics to more distant systems where spatial resolution is coarser, such as the starburst-driven superwind in M82 or the bipolar outflows of Seyfert galaxies.

APPENDIX A

Stacking the Chandra ACIS-I Observations

We began by retrieving all available *Chandra* ACIS-I observations of the Galactic Center with exposure times exceeding 10 ks (listed in Table 4.1) from the *Chandra* Data Archive, as exposures often did not have enough counts to be used by `celldetect` to align observations. Standard data processing was performed using the CIAO `chandra_repro` tool. To filter out background flares, we applied the `deflare` script, selecting time bins based on visual inspection of light curves. We restricted the light curve energy range to 2 keV, below the threshold where Galactic absorption ($N_H \sim 10^{23} cm^{-2}$) renders the source flux negligible, identifying only particle-induced flares, not X-ray flares from Sgr A*. Since our analysis focuses on arcminute-scale diffuse structure, the presence of flares from Sgr A*, which manifest on arcsecond scales, does not significantly affect our results. We prioritized retaining as much of the large-scale signal as possible.

Astrometric alignment was performed using the CIAO tools `celldetect` and `wcs_match`, aligning all observations to the tangent point of OBSID 3392. We followed the standard aspect re-projection procedure to align event files. We then created exposure-corrected images across multiple energy bands (1–2.6 keV, 2.6–5 keV, 4.5–6 keV, 5–8 keV, and 2–8 keV) using `flux_obs` and `merge_obs`, with each exposure map weighted by effective exposure time.

For preliminary alignment and pGMCA input cube creation, we used source lists from `celldetect`, which is faster than `wavdetect` and adequate for bright source identification in this context. We experimented with several detection parameters and ultimately adopted `fixedcell=6` and `thresh=6`, using a fixed cell size to avoid introducing bias from missing exposure maps. The resulting source list was manually refined: spurious detections were removed, overlapping detections interpreted as filamentary structures were merged into single extended ellipses, and circular regions were narrowed where appropriate. The final set of removed point sources is shown in Figure A.1, overlaid on the merged 1.3 merged data cube.

To isolate diffuse X-ray structures, we identified point sources using the CIAO tool `wavdetect`, which correlates the image with a Mexican Hat wavelet function at multiple

spatial scales. We adopted wavelet scales of 4, 8, and 16 pixels to ensure sensitivity to both compact and moderately extended sources. The significance threshold was set to produce approximately one spurious detection per CCD. At each scale, `wavdetect` performs an iterative cleansing procedure, masking out significant features to estimate the local background before detecting statistically significant peaks. We specified `ellsigma=2` to enlarge the resulting elliptical source regions, enabling conservative masking of source flux.

Following source detection, we manually reviewed and edited the `wavdetect` output. Several sources—particularly in regions of bright diffuse emission—appeared to be compact knots within extended structures rather than discrete point sources. These were removed from the region list to avoid over-subtraction. We verified that no obvious residual point sources were present in the resulting diffuse emission maps.

At this stage, we chose not to exclude the filamentary structures previously identified as nonthermal filaments (NTFs; Yusef-Zadeh & Mehringer, 1995). Before publication, we will assess whether removing them changes our results or uncovers new science. Finally, we note that while identifying and excluding point sources is important for accurate imaging of diffuse structures, our primary results, particularly those based on pGMCA decomposition, are not highly sensitive to the exact extent of source removal. pGMCA is robust against residual point sources, and our conclusions remain consistent across different masking strategies.

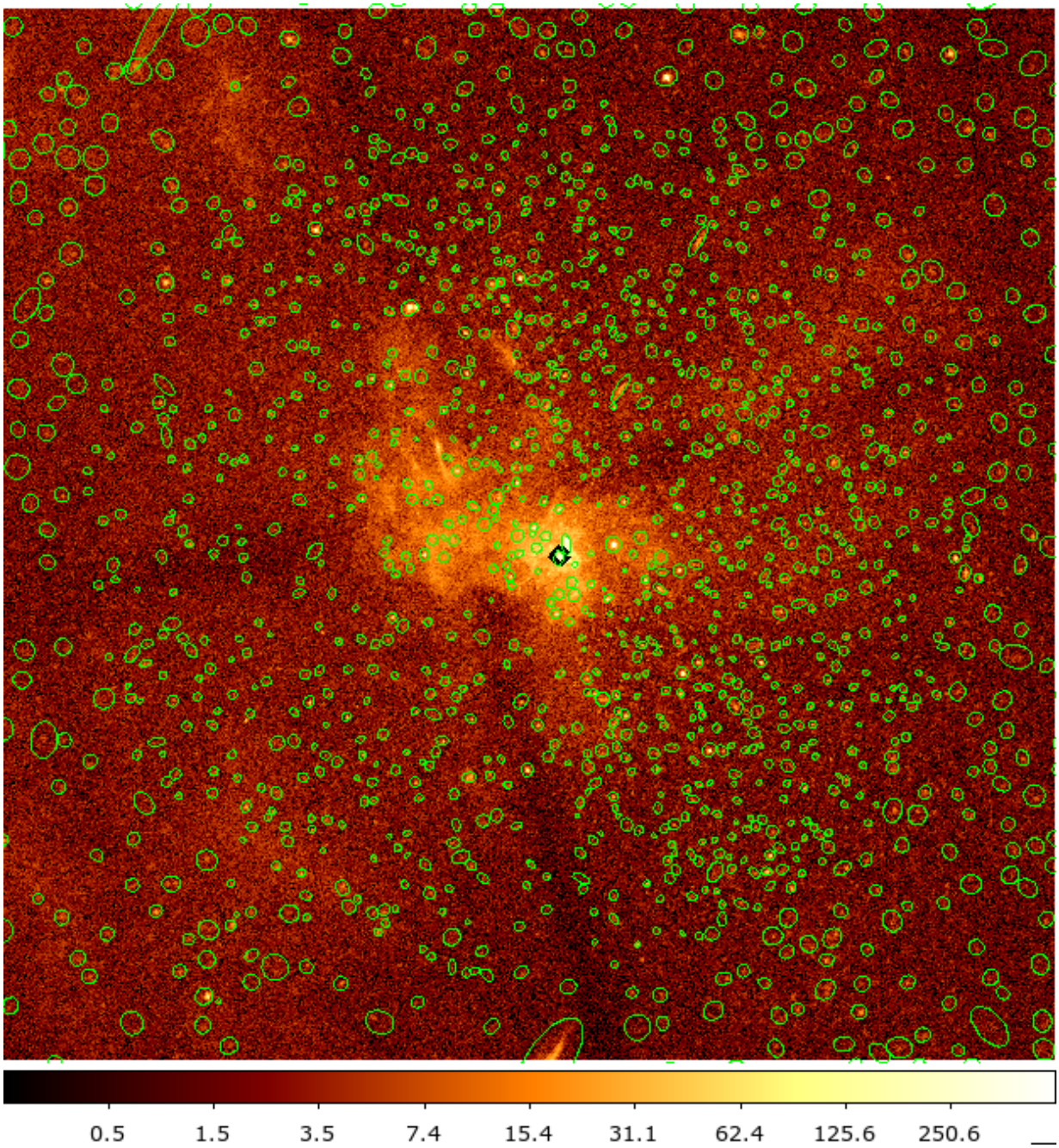


Figure A.1: Merged *Chandra* event image created using `reproject_obs`, with point sources identified by `wavdetect` shown as green ellipses. These regions were manually refined to exclude diffuse structures misidentified as compact sources. The black diamond near the center marks the location of the supermassive black hole, Sgr A*. The image is centered on Sgr A* and spans 8.4' x 8.4'.

BIBLIOGRAPHY

Anastasopoulou, K. 2025, in American Astronomical Society Meeting Abstracts, Vol. 245, American Astronomical Society Meeting Abstracts, 462.01

Anders, E., & Grevesse, N. 1989, GeoCoA, 53, 197, doi: 10.1016/0016-7037(89)90286-X

Arnaud, K. A. 1996, in Astronomical Society of the Pacific Conference Series, Vol. 101, Astronomical Data Analysis Software and Systems V, ed. G. H. Jacoby & J. Barnes, 17

Asplund, M., Grevesse, N., Sauval, A. J., & Scott, P. 2009, ARA&A, 47, 481, doi: 10.1146/annurev.astro.46.060407.145222

Baganoff, F. K., Maeda, Y., Morris, M., et al. 2003, ApJ, 591, 891, doi: 10.1086/375145

Begelman, M. C. 2012, MNRAS, 420, 2912, doi: 10.1111/j.1365-2966.2011.20071.x

Bender, R., Kormendy, J., Bower, G., et al. 2005, ApJ, 631, 280, doi: 10.1086/432434

Blandford, R. D., & Begelman, M. C. 1999, MNRAS, 303, L1, doi: 10.1046/j.1365-8711.1999.02358.x

—. 2004, MNRAS, 349, 68, doi: 10.1111/j.1365-2966.2004.07425.x

Bobin, J., Hamzaoui, I. E., Picquenot, A., & Acero, F. 2020, IEEE Transactions on Image Processing, 29, 9429

Bobin, J., Rapin, J., Larue, A., & Starck, J.-L. 2015, IEEE Transactions on Signal Processing, 63, 1199, doi: 10.1109/TSP.2015.2391071

Bobin, J., Starck, J.-L., Fadili, J., & Moudden, Y. 2007, IEEE Transactions on Image Processing, 16, 2662, doi: 10.1109/TIP.2007.906256

Bobin, J., Sureau, F., & Starck, J.-L. 2016, A&A, 591, A50, doi: 10.1051/0004-6361/201527822

Bondi, H. 1952, MNRAS, 112, 195, doi: 10.1093/mnras/112.2.195

Cai, X., McEwen, J. D., & Pereyra, M. 2021, arXiv e-prints, arXiv:2106.03646, doi: 10.48550/arXiv.2106.03646

Calderón, D., Cuadra, J., Russell, C. M. P., et al. 2025, A&A, 693, A180, doi: 10.1051/0004-6361/202452800

Calderón, D., Cuadra, J., Schartmann, M., Burkert, A., & Russell, C. M. P. 2020, ApJL, 888, L2, doi: 10.3847/2041-8213/ab5e81

Camilloni, F., Becker, W., & Sasaki, M. 2024, A&A, 681, A122, doi: 10.1051/0004-6361/202347970

Canizares, C. R., Davis, J. E., Dewey, D., et al. 2005, PASP, 117, 1144, doi: 10.1086/432898

Chatterjee, K., Markoff, S., Neilsen, J., et al. 2021, MNRAS, 507, 5281, doi: 10.1093/mnras/stab2466

Chatzopoulos, S., Fritz, T. K., Gerhard, O., et al. 2015, MNRAS, 447, 948, doi: 10.1093/mnras/stu2452

Chiotellis, A., Zapartas, E., & Meyer, D. M. A. 2024, MNRAS, 531, 5109, doi: 10.1093/mnras/stae947

Ciurlo, A., Morris, M. R., Campbell, R. D., et al. 2021, ApJ, 910, 143, doi: 10.3847/1538-4357/abe71a

Coil, A. L., & Ho, P. T. P. 2000, ApJ, 533, 245, doi: 10.1086/308650

Corrales, L., Baganoff, F. K., Wang, Q. D., et al. 2020, ApJ, 891, 71, doi: 10.3847/1538-4357/ab74df

Corrales, L. R., García, J., Wilms, J., & Baganoff, F. 2016, MNRAS, 458, 1345, doi: 10.1093/mnras/stw376

Cuadra, J., Armitage, P. J., & Alexander, R. D. 2008, MNRAS, 388, L64, doi: 10.1111/j.1745-3933.2008.00500.x

Cuadra, J., Nayakshin, S., Springel, V., & Di Matteo, T. 2005, MNRAS, 360, L55, doi: 10.1111/j.1745-3933.2005.00045.x

Cuadra, J., Nayakshin, S., & Wang, Q. D. 2015, MNRAS, 450, 277, doi: 10.1093/mnras/stv584

Dexter, J., Tchekhovskoy, A., Jiménez-Rosales, A., et al. 2020, MNRAS, 497, 4999, doi: 10.1093/mnras/staa2288

Do, T., Kerzendorf, W., Konopacky, Q., et al. 2018, ApJL, 855, L5, doi: 10.3847/2041-8213/aaaec3

Do, T., Martinez, G. D., Yelda, S., et al. 2013, ApJL, 779, L6, doi: 10.1088/2041-8205/779/1/L6

Draine, B. T. 2011, Physics of the Interstellar and Intergalactic Medium

Eadie, G. M., Speagle, J. S., Cisewski-Kehe, J., et al. 2023, arXiv e-prints, arXiv:2302.04703, doi: 10.48550/arXiv.2302.04703

Ehlerová, S., Palouš, J., Morris, M. R., et al. 2022, A&A, 668, A124, doi: 10.1051/0004-6361/202244682

Ekers, R. D., Goss, W. M., Schwarz, U. J., Downes, D., & Rogstad, D. H. 1975, A&A, 43, 159

Event Horizon Telescope Collaboration, Akiyama, K., Alberdi, A., et al. 2022a, ApJL, 930, L12, doi: 10.3847/2041-8213/ac6674

—. 2022b, ApJL, 930, L12, doi: 10.3847/2041-8213/ac6674

—. 2024, ApJL, 964, L26, doi: 10.3847/2041-8213/ad2df1

Fabian, A. C. 2012, ARA&A, 50, 455, doi: 10.1146/annurev-astro-081811-125521

Feroz, F. 2013, in 2013 IEEE 13th International Conference on Data Mining Workshops, 8–15, doi: 10.1109/ICDMW.2013.21

Feroz, F., Hobson, M. P., & Bridges, M. 2009, MNRAS, 398, 1601, doi: 10.1111/j.1365-2966.2009.14548.x

Foreman-Mackey, D., Hogg, D. W., Lang, D., & Goodman, J. 2013, PASP, 125, 306, doi: 10.1086/670067

Fritz, T. K., Gillessen, S., Dodds-Eden, K., et al. 2011, ApJ, 737, 73, doi: 10.1088/0004-637X/737/2/73

Fujita, Y., Kawakatu, N., & Nagai, H. 2022, ApJ, 924, 24, doi: 10.3847/1538-4357/ac31a6

Gall, C., Hjorth, J., & Andersen, A. C. 2011, A&A Rv, 19, 43, doi: 10.1007/s00159-011-0043-7

Genzel, R., Eisenhauer, F., & Gillessen, S. 2010, Reviews of Modern Physics, 82, 3121, doi: 10.1103/RevModPhys.82.3121

Genzel, R., & Stutzki, J. 1989, ARA&A, 27, 41, doi: 10.1146/annurev.aa.27.090189.000353

Ghez, A. M., Klein, B. L., Morris, M., & Becklin, E. E. 1998, ApJ, 509, 678, doi: 10.1086/306528

Gillessen, S., Genzel, R., Fritz, T. K., et al. 2012, Nature, 481, 51, doi: 10.1038/nature10652

Gillessen, S., Plewa, P. M., Eisenhauer, F., et al. 2017, ApJ, 837, 30, doi: 10.3847/1538-4357/aa5c41

Gillessen, S., Plewa, P. M., Widmann, F., et al. 2019, ApJ, 871, 126, doi: 10.3847/1538-4357/aaf4f8

GRAVITY Collaboration, Abuter, R., Amorim, A., et al. 2019, A&A, 625, L10, doi: 10.1051/0004-6361/201935656

Grevesse, N., & Anders, E. 1989, in American Institute of Physics Conference Series, Vol. 183, Cosmic Abundances of Matter, ed. C. J. Waddington, 1–8, doi: 10.1063/1.38013

Haggard, D., Nynka, M., Mon, B., et al. 2019, ApJ, 886, 96, doi: 10.3847/1538-4357/ab4a7f

Handley, W. J., Hobson, M. P., & Lasenby, A. N. 2015, MNRAS, 453, 4384, doi: 10.1093/mnras/stv1911

Ho, L. C. 2008, ARA&A, 46, 475, doi: 10.1146/annurev.astro.45.051806.110546

Hsieh, P.-Y., Koch, P. M., Kim, W.-T., et al. 2019, ApJL, 885, L20, doi: 10.3847/2041-8213/ab4e1e

Jeffreys, H. 1998, Theory of Probability (Oxford University Press), doi: 10.1093/oso/9780198503682.001.0001

Jia, S., Xu, N., Lu, J. R., et al. 2023, ApJ, 949, 18, doi: 10.3847/1538-4357/acb939

Kawasaki, M., Ozaki, M., Nagase, F., Inoue, H., & Petre, R. 2005, ApJ, 631, 935, doi: 10.1086/432591

Kormendy, J., & Ho, L. C. 2013, ARA&A, 51, 511, doi: 10.1146/annurev-astro-082708-101811

Lau, R. M., Herter, T. L., Morris, M. R., Li, Z., & Adams, J. D. 2015, VizieR Online Data Catalog (other), 0210, J/other/Sci/348

Lazendic, J. S., & Slane, P. O. 2006, ApJ, 647, 350, doi: 10.1086/505380

Lee, M. D., & Wagenmakers, E.-J. 2013, Bayesian cognitive modeling: A practical course., Bayesian cognitive modeling: A practical course. (New York, NY, US: Cambridge University Press), doi: 10.1017/CBO9781139087759

Leutenegger, M. A., Cohen, D. H., Zsargó, J., et al. 2010, ApJ, 719, 1767, doi: 10.1088/0004-637X/719/2/1767

Lu, J. R., Do, T., Ghez, A. M., et al. 2013, ApJ, 764, 155, doi: 10.1088/0004-637X/764/2/155

Lützgendorf, N., Helm, E. v. d., Pelupessy, F. I., & Portegies Zwart, S. 2016, MNRAS, 456, 3645, doi: 10.1093/mnras/stv2918

Ma, R.-Y., Roberts, S. R., Li, Y.-P., & Wang, Q. D. 2019, MNRAS, 483, 5614, doi: 10.1093/mnras/sty3039

Maeda, Y., Baganoff, F. K., Feigelson, E. D., et al. 2002, ApJ, 570, 671, doi: 10.1086/339773

Marin, F., Churazov, E., Khabibullin, I., et al. 2023, Nature, 619, 41, doi: 10.1038/s41586-023-06064-x

Marrone, D. P., Moran, J. M., Zhao, J.-H., & Rao, R. 2007, ApJL, 654, L57, doi: 10.1086/510850

Marsh, K. A., Whitworth, A. P., Lomax, O., et al. 2017, MNRAS, 471, 2730, doi: 10.1093/mnras/stx1723

Martins, F., Genzel, R., Hillier, D. J., et al. 2007, A&A, 468, 233, doi: 10.1051/0004-6361:20066688

McConnell, N. J., & Ma, C.-P. 2013, ApJ, 764, 184, doi: 10.1088/0004-637X/764/2/184

McEwen, B. C., Sjouwerman, L. O., & Pihlström, Y. M. 2016, ApJ, 832, 129, doi: 10.3847/0004-637X/832/2/129

McEwen, J. D., Wallis, C. G. R., Price, M. A., & Spurio Mancini, A. 2021, arXiv e-prints, arXiv:2111.12720, doi: 10.48550/arXiv.2111.12720

Melia, F. 1992, ApJL, 387, L25, doi: 10.1086/186297

Molinari, S., Bally, J., Noriega-Crespo, A., et al. 2011, ApJL, 735, L33, doi: 10.1088/2041-8205/735/2/L33

Morris, M., & Serabyn, E. 1996, ARA&A, 34, 645, doi: 10.1146/annurev.astro.34.1.645

Muno, M. P., Baganoff, F. K., Bautz, M. W., et al. 2003, ApJ, 589, 225, doi: 10.1086/374639

Murchikova, E. M., Phinney, E. S., Pancoast, A., & Blandford, R. D. 2019, Nature, 570, 83, doi: 10.1038/s41586-019-1242-z

Narayan, R., & McClintock, J. E. 2008, NewAR, 51, 733, doi: 10.1016/j.newar.2008.03.002

Narayan, R., Sadowski, A., Penna, R. F., & Kulkarni, A. K. 2012, MNRAS, 426, 3241, doi: 10.1111/j.1365-2966.2012.22002.x

Narayan, R., & Yi, I. 1994, ApJL, 428, L13, doi: 10.1086/187381

Neilsen, J., Nowak, M. A., Gammie, C., et al. 2013, ApJ, 774, 42, doi: 10.1088/0004-637X/774/1/42

Nogueras-Lara, F., Schödel, R., Gallego-Calvente, A. T., et al. 2020, Nature Astronomy, 4, 377, doi: 10.1038/s41550-019-0967-9

Nowak, M. A., Neilsen, J., Markoff, S. B., et al. 2012, ApJ, 759, 95, doi: 10.1088/0004-637X/759/2/95

Nynka, M., Hailey, C. J., Mori, K., et al. 2013, ApJL, 778, L31, doi: 10.1088/2041-8205/778/2/L31

Olivares, V., Picquenot, A., Su, Y., et al. 2025, Nature Astronomy, doi: 10.1038/s41550-024-02473-8

Ono, A., Uchiyama, H., Yamauchi, S., et al. 2019, PASJ, 71, 52, doi: 10.1093/pasj/psz025

Pang, B. 2011, PhD thesis, University of Toronto, Canada

Park, S., Muno, M. P., Baganoff, F. K., et al. 2004, ApJ, 603, 548, doi: 10.1086/381542

Paumard, T., Genzel, R., Martins, F., et al. 2006, ApJ, 643, 1011, doi: 10.1086/503273

Peißker, F., Zajaček, M., Thomkins, L., et al. 2023, ApJ, 956, 70, doi: 10.3847/1538-4357/acf6b5

Picquenot, A., Acero, F., Bobin, J., et al. 2019, A&A, 627, A139, doi: 10.1051/0004-6361/201834933

Picquenot, A., Acero, F., Holland-Ashford, T., Lopez, L. A., & Bobin, J. 2021, A&A, 646, A82, doi: 10.1051/0004-6361/202039170

Pierce-Price, D., Richer, J. S., Greaves, J. S., et al. 2000, ApJL, 545, L121, doi: 10.1086/317884

Pihlström, Y. M., & Sjouwerman, L. O. 2006, in Journal of Physics Conference Series, Vol. 54, Journal of Physics Conference Series, ed. R. Schödel, G. C. Bower, M. P. Muno, S. Nayakshin, & T. Ott (IOP), 77–80, doi: 10.1088/1742-6596/54/1/014

Ponti, G., Terrier, R., Goldwurm, A., Belanger, G., & Trap, G. 2010, ApJ, 714, 732, doi: 10.1088/0004-637X/714/1/732

Ponti, G., Jin, C., De Marco, B., et al. 2016, MNRAS, 461, 2688, doi: 10.1093/mnras/stw1382

Ponti, G., Hofmann, F., Churazov, E., et al. 2019, Nature, 567, 347, doi: 10.1038/s41586-019-1009-6

Predehl, P., & Schmitt, J. H. M. M. 1995, A&A, 293, 889

Predehl, P., Sunyaev, R. A., Becker, W., et al. 2020, Nature, 588, 227, doi: 10.1038/s41586-020-2979-0

Price, D. J. 2007, PASA, 24, 159, doi: 10.1071/AS07022

Quataert, E. 2002, ApJ, 575, 855, doi: 10.1086/341425

—. 2004, ApJ, 613, 322, doi: 10.1086/422973

Ressler, S. M., Quataert, E., & Stone, J. M. 2018, MNRAS, 478, 3544, doi: 10.1093/mnras/sty1146

—. 2020a, MNRAS, 492, 3272, doi: 10.1093/mnras/stz3605

Ressler, S. M., White, C. J., & Quataert, E. 2023, MNRAS, 521, 4277, doi: 10.1093/mnras/stad837

Ressler, S. M., White, C. J., Quataert, E., & Stone, J. M. 2020b, ApJL, 896, L6, doi: 10.3847/2041-8213/ab9532

Rimoldi, A., Rossi, E. M., Piran, T., & Portegies Zwart, S. 2015, MNRAS, 447, 3096, doi: 10.1093/mnras/stu2630

Roberts, S. R., Jiang, Y.-F., Wang, Q. D., & Ostriker, J. P. 2017, MNRAS, 466, 1477, doi: 10.1093/mnras/stw2995

Rockefeller, G., Fryer, C. L., Baganoff, F. K., & Melia, F. 2005, ApJL, 635, L141, doi: 10.1086/499360

Russell, C. M. P., Wang, Q. D., & Cuadra, J. 2017, MNRAS, 464, 4958, doi: 10.1093/mnras/stw2584

Sakano, M., Warwick, R. S., Decourchelle, A., & Predehl, P. 2004, MNRAS, 350, 129, doi: 10.1111/j.1365-2966.2004.07571.x

Sánchez Díaz, G., Richer, M., Martínez González, M., et al. 2024, -. https://atomdb.qcdevs.org/

Sander, A. A. C., Hamann, W. R., Todt, H., et al. 2019, A&A, 621, A92, doi: 10.1051/0004-6361/201833712

Schödel, R., Morris, M. R., Muzic, K., et al. 2011, A&A, 532, A83, doi: 10.1051/0004-6361/201116994

Shakura, N. I., & Sunyaev, R. A. 1973, A&A, 24, 337

Sjouwerman, L. O., & Pihlström, Y. M. 2008, ApJ, 681, 1287, doi: 10.1086/588753

Smith, R. K., Brickhouse, N. S., Liedahl, D. A., & Raymond, J. C. 2001, ApJL, 556, L91, doi: 10.1086/322992

Solanki, S., Ressler, S. M., Murchikova, L., Stone, J. M., & Morris, M. R. 2023, ApJ, 953, 22, doi: 10.3847/1538-4357/acdb6f

Springel, V. 2005, MNRAS, 364, 1105, doi: 10.1111/j.1365-2966.2005.09655.x

Starck, J.-L., Fadili, J., & Murtagh, F. 2007, IEEE Transactions on Image Processing, 16, 297, doi: 10.1109/TIP.2006.887733

Tashiro, M., Kelley, R., Watanabe, S., et al. 2025, PASJ, doi: 10.1093/pasj/psaf023

Tsuboi, M., Kitamura, Y., Tsutsumi, T., et al. 2019, PASJ, 71, 105, doi: 10.1093/pasj/psz089

Tsuboi, M., Kitamura, Y., Uehara, K., et al. 2017, ApJ, 842, 94, doi: 10.3847/1538-4357/aa74e3

Tsuboi, M., Tadaki, K.-i., Miyazaki, A., & Handa, T. 2011, PASJ, 63, 763, doi: 10.1093/pasj/63.4.763

Verner, D. A., & Yakovlev, D. G. 1995, A&AS, 109, 125

Vink, J. 2012, A&A Rv, 20, 49, doi: 10.1007/s00159-011-0049-1

Vogelsberger, M., Genel, S., Springel, V., et al. 2014, Nature, 509, 177, doi: 10.1038/nature13316

von Fellenberg, S. D., Gillessen, S., Graciá-Carpio, J., et al. 2018, ApJ, 862, 129, doi: 10.3847/1538-4357/aacd4b

Wang, Q. D. 2022, Universe, 8, 515, doi: 10.3390/universe8100515

Wang, Q. D., Li, J., Russell, C. M. P., & Cuadra, J. 2020, MNRAS, 492, 2481, doi: 10.1093/mnras/stz3624

Wang, Q. D., Dong, H., Cotera, A., et al. 2010, MNRAS, 402, 895, doi: 10.1111/j.1365-2966.2009.15973.x

Wang, Q. D., Nowak, M. A., Markoff, S. B., et al. 2013, Science, 341, 981, doi: 10.1126/science.1240755

Weinberger, R., Springel, V., Pakmor, R., et al. 2018, MNRAS, 479, 4056, doi: 10.1093/mnras/sty1733

White, R. L., & Long, K. S. 1991a, ApJ, 373, 543, doi: 10.1086/170073

—. 1991b, ApJ, 373, 543, doi: 10.1086/170073

Wilms, J., Allen, A., & McCray, R. 2000, ApJ, 542, 914, doi: 10.1086/317016

XRISM Collaboration. 2024, arXiv e-prints, arXiv:2412.00676, doi: 10.48550/arXiv.2412.00676

Xu, Y.-D., Narayan, R., Quataert, E., Yuan, F., & Baganoff, F. K. 2006, ApJ, 640, 319, doi: 10.1086/499932

Yalinewich, A., Piran, T., & Sari, R. 2017, ApJ, 838, 12, doi: 10.3847/1538-4357/aa5d0f

Yelda, S., Ghez, A. M., Lu, J. R., et al. 2014, ApJ, 783, 131, doi: 10.1088/0004-637X/783/2/131

Yuan, F., Gan, Z., Narayan, R., et al. 2015, ApJ, 804, 101, doi: 10.1088/0004-637X/804/2/101

Yuan, F., & Narayan, R. 2014, ARA&A, 52, 529, doi: 10.1146/annurev-astro-082812-141003

Yuan, F., Quataert, E., & Narayan, R. 2003, ApJ, 598, 301, doi: 10.1086/378716

Yuan, F., Yoon, D., Li, Y.-P., et al. 2018, ApJ, 857, 121, doi: 10.3847/1538-4357/aab8f8

Yusef-Zadeh, F. 1986, PhD thesis, Columbia University, New York

Yusef-Zadeh, F., Lacy, J. H., Wardle, M., et al. 2010, ApJ, 725, 1429, doi: 10.1088/0004-637X/725/2/1429

Yusef-Zadeh, F., & Mehringer, D. M. 1995, ApJL, 452, L37, doi: 10.1086/309698

Yusef-Zadeh, F., & Morris, M. 1987, ApJ, 320, 545, doi: 10.1086/165572

Yusef-Zadeh, F., Roberts, D. A., Goss, W. M., Frail, D. A., & Green, A. J. 1996, ApJL, 466, L25, doi: 10.1086/310165

—. 1999a, ApJ, 512, 230, doi: 10.1086/306769

—. 1999b, ApJ, 512, 230, doi: 10.1086/306769

Yusef-Zadeh, F., Roberts, D. A., & Wardle, M. 1997, ApJL, 490, L83, doi: 10.1086/310997

Yusef-Zadeh, F., Royster, M., Wardle, M., et al. 2020, MNRAS, 499, 3909, doi: 10.1093/mnras/staa2399

Yusef-Zadeh, F., Stolovy, S. R., Burton, M., Wardle, M., & Ashley, M. C. B. 2001, ApJ, 560, 749, doi: 10.1086/322496

Zhao, J.-H., Morris, M. R., & Goss, W. M. 2013, ApJ, 777, 146, doi: 10.1088/0004-637X/777/2/146

—. 2016, ApJ, 817, 171, doi: 10.3847/0004-637X/817/2/171

Zhou, P., Leung, S.-C., Li, Z., et al. 2021, ApJ, 908, 31, doi: 10.3847/1538-4357/abbd45